

LIGHT TWO-WHEELED ELECTRIC VEHICLE ENERGY BALANCE INVESTIGATION USING CHASSIS DYNAMOMETER

Szymon RACEWICZ,^{*} Paweł KAZIMIERCZUK^{**}

^{*}Faculty of Technical Sciences, Department of Mechatronics and Technical-Computer Sciences Education, University of Warmia and Mazury in Olsztyn, 2 Michała Oczapowskiego St., 10-719 Olsztyn, Poland

^{**}Maintenance Department, Michelin Polska S.A., 9 Władysława Leonharda St., 10-454 Olsztyn, Poland

szymon.racewicz@uwm.edu.pl, pawel.kazimierczuk@michelin.com

received 30 April 2020, revised 15 January 2021, accepted 19 January 2021

Abstract: The article presents the methodology for light two-wheeled electric vehicle energy balance investigation using MAHA LPS 3000 chassis dynamometer. For this purpose, the laboratory tests, as well as the road tests, have been performed on the self-constructed light two-wheeled electric vehicle equipped with the 3 kW BLDC motor and the 100.8 V battery pack. The road test data have been used to set up the dynamometer parameters in order to simulate the real road drive taking into account, among others, the rolling resistances and the air drag coefficient. The overall energy consumption for the laboratory tests and the road conditions' tests have been then compared for different vehicle speeds. In addition, based on the power and the torque characteristics measured on the MAHA chassis dynamometer, the efficiency of the vehicle electric drive system and the efficiency of the battery charging process have been calculated.

Keywords: Electric vehicle, energy balance, chassis dynamometer, drive system efficiency

1. INTRODUCTION

Since the last few decades, electric vehicles have gained in popularity. This is because of the recent technological improvements in the areas of electric motors, power electronics, and energy storages, which makes them more accessible and affordable (Ho et al., 2014; Lin et al., 2015; Lim et al., 2016; Sarlioglu et al., 2017; Li et al., 2018). Other reasons are the obvious environmental advantages and the much lower cost of transportation in comparison to the vehicles with internal combustion engines or even hybrids (Bertoluzzo and Buja, 2011; Saponara et al., 2020). Although this cost is relatively low, it is still closely related to the overall efficiency of the electric vehicle drive system and so it can be further reduced. This is an issue raised in many researches, for example, Kumar et al. (2017), Kumar and Sivakumar (2017), Laitinen et al. (2017), Dobrucky et al. (2019) and Zaghari et al. (2020). In order to better investigate and implement new technical solutions, one has to provide repetitive traction conditions during certain tests. Chassis dynamometers help to study motor parameters as well as the fuel or energy consumption in laboratory conditions (Chen Mingjie et al., 2010). Nevertheless, most chassis dynamometers, for example, the MAHA LPS 3000, are originally dedicated to power characteristics investigation of cars and motorcycles. Their predefined parameter sets mainly apply to vehicles with internal combustion engines. The MAHA dynamometer can simulate the real road conditions using the eddy current breaks. Moreover, it can also measure the characteristics of four-wheel-drive vehicles. It is then interesting to use such a dynamometer for light two-wheeled electric vehicle testing in order to investigate its mechanical and electrical parameters.

2. LIGHT TWO-WHEELED ELECTRIC VEHICLE CONSTRUCTION

The studied vehicle has been designed and built from scratch using brushless DC motor of 3 kW of nominal continuous output mechanical power and the battery pack built of 360 lithium-ion power cells of 2600 mAh each. According to the Polish law formulated in the Act on Road Traffic of June 20, 1997, with the changes made on April 1, 2011, it cannot be called electric bicycle, neither electric moped among others due to the over normed output power (UPRD (1997), 1997). Indeed, the vehicle weighs 78 kg and can reach the speed of up to about 100 km/h. The maximum output power measured on the chassis dynamometer has been equal to 4.7 kW (6.4 BHP) with 184.1 Nm of torque for 440 rpm. The motor is placed in the rear wheel hub without any gearbox. The maximum voltage of the battery pack is 100.8 V with the 39 Ah of nominal capacity. More detailed information about the previous prototype of the vehicle can be found in Racewicz et al. (2018). Its final version is presented in Fig. 1.



Fig. 1. Light two-wheeled electric vehicle powered by 3 kW BLDC motor and classical bicycle pedals

3. DESCRIPTION OF TESTS

In order to find coherence between vehicle electric parameters recorded during real road drive and the simulated road drive on the MAHA LPS 3000 chassis dynamometer, several assumptions have to be met. These are the recommendations of the dynamometer manufacturer as well as the official procedures described in COMMISSION DELEGATED REGULATION (EU) No 134/2014 of 16 December 2013 supplementing Regulation (EU) No 168/2013 of the European Parliament and of the Council with regard to environmental and propulsion unit performance requirements and amending Annex V the (2013).

All the tests were carried out with a fully charged battery when the ambient temperature was about 24°C. The test road was sufficiently long and straight without any inclinations. Wind speed was close to zero. The measurements started at a speed of 10 km/h, which was then increased by 10 km/h until it reached the speed of 90 km/h. The speed was controlled using the vehicle speedometer. For each speed, the time, distance, motor voltage, motor current and power were registered and saved on the SD card by the on-board computer designed for this purpose. The measurements of electric parameters were recorded in 0.5 s intervals and were then averaged for calculations. The summarized road measurements results are presented in Tab. 1.

Tab. 1. Road tests results

Speed [km/h]	Time [s]	Distance [m]	Current [A]	Power [kW]
10.00	60.35	169.70	0.96	0.10
20.00	25.50	141.67	2.08	0.21
30.00	25.50	212.50	4.24	0.41
40.00	25.25	280.56	5.86	0.58
50.00	18.50	256.94	11.00	1.07
60.00	22.00	366.67	20.39	1.96
70.00	20.50	398.61	29.42	2.79
80.00	18.25	405.56	42.06	3.91
90.00	21.25	531.25	64.21	5.81

The same procedure was repeated on the chassis dynamometer for the laboratory tests. Drive profile representing the actual speed of the vehicle and its motor current is shown in Fig. 2 and the measurement values are collected in Tab. 2.

Tab. 2. Laboratory tests results

Speed [km/h]	Time [s]	Distance [m]	Current [A]	Power [kW]
10.00	24	67	3.29	0.33
20.00	13	69	7.07	0.71
30.00	16	126	10.22	1.02
40.00	13	140	14.46	1.43
50.00	19	264	18.57	1.83
60.00	17	275	24.58	2.39
70.00	16	300	26.90	2.55
80.00	19	417	32.31	3.10
90.00	14	346	43.29	4.12
100.00	14	385	47.06	4.40

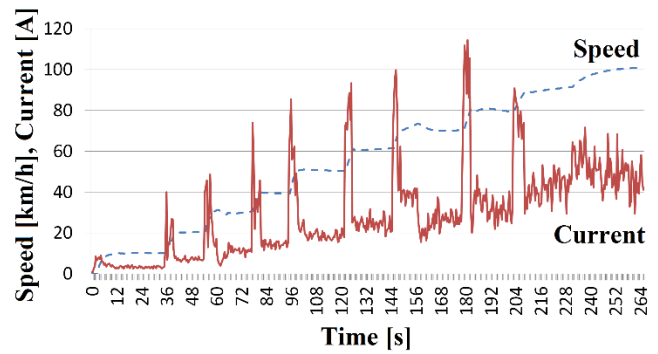


Fig. 2. Speed and motor current registered during chassis dynamometer test

In order to set up the MAHA chassis dynamometer parameters, the data collected during the road test, that is, speed, motor voltage and current were mapped for a laboratory test. The ambient temperature in the laboratory room was about 22°C. The MAHA LPS 3000 chassis dynamometer enables exact simulation of the predefined real road drive conditions. The load is applied by the eddy current brakes as a function of vehicle speed, which reflects different road drive conditions. This process is supervised by the microprocessor-controlled computing unit with graphic and digital display of the measured values.

For the test purpose, the MAHA chassis dynamometer parameters were set up assuming that the vehicle is moving linearly on the flat horizontal surface. The total driving force F on the rear wheel is determined by relation (1) and the power P on the wheel is described by equation (2):

$$F = F_r + F_w + F_g + F_b = m \cdot g \cdot f + 0,5 \rho \cdot C_D \cdot A_f \cdot v^2 + m \cdot g \cdot w + m \cdot a \tag{1}$$

$$P = F \cdot v \tag{2}$$

where v is the speed of the vehicle, a is the acceleration of the vehicle, $m = 123 \text{ kg}$ is the mass of the vehicle with driver, $g = 9.81 \text{ m/s}^2$ is the gravity acceleration, $f = 0.009$ is the rolling resistance coefficient, $\rho = 1.2 \text{ kg/m}^3$ is the air density, $C_D = 0.5$ is the air drag coefficient, $A_f = 0.62 \text{ m}^2$ is the frontal area taking into account the driver posture, w is the road inclination. The more detailed procedure of setting up the MAHA chassis dynamometer and determining all the needed components concerning driving forces and vehicle coefficients have been described in Kolator et al. (2018).

4. ENERGY CONSUMPTION ANALYSIS

Using data from the road tests (Tab. 1) as well as the laboratory tests (Tab. 2), the energy consumption E for each speed was evaluated and compared. For calculations of the energy consumption, formula (3) has been applied.

$$E = \frac{P \cdot t}{s} \cdot \frac{2500}{9} \tag{3}$$

where E is the consumed energy in [Wh/km], P is the motor power in [kW], t is the drive time in [s] and s is the distance travelled in [m].

Fig. 3 presents the comparison between energy consumption during road and laboratory tests for different speeds.

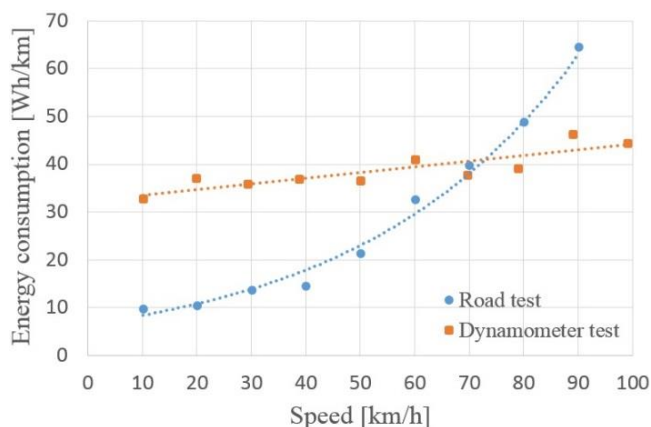


Fig. 3. Comparison of energy consumption during road and laboratory tests

The discrepancy of the energy consumption results for the road and laboratory tests especially for low speeds is due to the fact that the dynamometer rollers and eddy current brakes have an important inertia factor, which cannot be lowered. Moreover, the eddy current brakes are cooled by the fans placed on the same shaft as rollers, which introduces an additional load proportional to the roller speed. Analysing Fig. 3, one can observe that in the light two-wheeled vehicle case, the chassis dynamometer can be successfully used and controlled over the speed of about 70 km/h. Moreover, different natures of the characteristics, that is, quadratic for the road tests and linear for the laboratory tests are due to the lack of air resistance in laboratory conditions, which was simulated by the changing load of the chassis dynamometer rollers. Nevertheless, for such small values of the vehicle parameters introduced to the chassis dynamometer computer, it generated the rollers' load close to zero, so just the linear load coming from the rollers' fans was applied. This is the main limit of car chassis dynamometers, which has to be taken into account for such type of measurements.

Battery pack capacity has also an impact on the total energy consumption of the electric vehicle (Fei Feng et al., 2012; Park et al., 2019). A properly designed battery pack maximizes the use of energy resources in relation to the distance travelled. In order to properly design the battery pack, one has to take into consideration the following important aspects: maximum discharge current, single cell capacity, total battery weight and mass distribution over the battery volume. Available battery cells can be divided into two categories: low current cells with high capacity and high current cells with low capacity. For low power vehicles (up to 3 kW), the better solution is to use high capacity cells. The advantage of such a configuration is the lower weight of the battery pack and its higher energy storage capacity. This results in larger distances, which can be covered by a vehicle. The disadvantage of such a solution is faster cells' wear, which is about 3 years assuming daily use of a vehicle. The second group are the high current low capacity cells, which can deliver higher current translated into better driving dynamics but also higher operating temperature. This solution obliges to design larger and heavier battery packs in order to obtain a similar capacity as for the high capacity cells. The advantage of using a high discharge current cells is the longer battery life, which is about several years assuming the same conditions as mentioned above. The batteries used in the studied project are the high current low capacity Li-ion cells SONY US18650VTC5. The total weight of the battery pack is about 18 kg.

During the laboratory tests on the chassis dynamometer, the weight of the vehicle is not taken into account as the vehicle is tested in a stable position. The MAHA chassis dynamometer is able to simulate an inertial force for the vehicles whose mass exceeds 200 kg. However, the usefulness of such an approach has been proved for the lithium-ion electric vehicle battery parameter estimation in Kim et al. (2016). In the next section, an approach for the overall efficiency of the electric drive system has been proposed. In contrast to the energy consumption analysis, it gives the unequivocal results, which are independent of the assumed road conditions.

5. EFFICIENCY OF THE ELECTRIC DRIVE SYSTEM

In order to evaluate the efficiency of the vehicle electric drive system, the power and torque characteristics' test was carried out using the MAHA chassis dynamometer. Discrete measurement option was used. The measurement started at a speed of 20 km/h, which was then increased by 10 km/h until it reached a speed of 80 km/h. The results from the MAHA computer system are presented in Fig. 4.

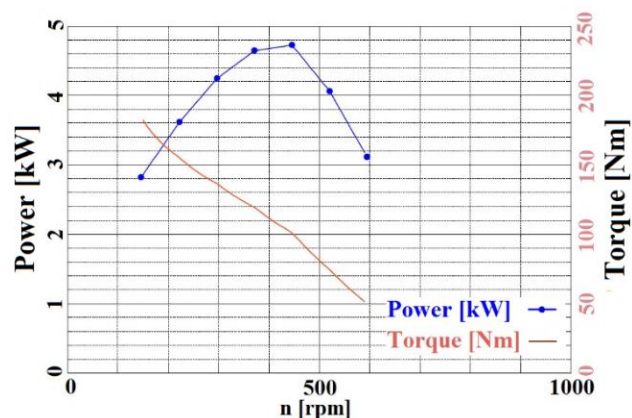


Fig. 4. Power and torque characteristics of the light two-wheeled electric vehicle

During the test, the voltage of the battery pack as well as the total current consumed by the vehicle were measured and stored in the on-board data acquisition system based on Arduino Mega 2560 Pro platform. In the studied case, the use of such simple DAQ system gives reliable measurement results (Barański et al., 2019). In addition to the voltage and current measurements, the system also displayed the actual calculated power consumed by the vehicle, the actual speed, percentage of the battery charge as well as the temperatures of the BLDC motor, motor controller and the battery pack, which is extremely important for the battery pack operation and its life cycle (Chu et al., 2011). The on-board computer consumes about 200 W of power, which is not a relevant value in comparison to the BLDC motor power and so it was neglected in the further considerations. The averaged measured values of the voltage and current for the maximum mechanical power were equal to respectively 97.2 V and 111.28 A.

The maximum mechanical power obtained during the test was equal to 4.7 kW (6.4 BHP) for 440 rpm and the maximum torque was equal to 184.1 Nm. For total drive system efficiency calculations, formula (4) has been used.

$$\mu = \frac{P_{\text{mechanical}}}{P_{\text{electrical}}} \cdot 100\% \quad (4)$$

where $P_{\text{mechanical}}$ is the mechanical power measured using the chassis dynamometer and $P_{\text{electrical}}$ is the electrical power calculated as a product of consumed voltage and current measured on the battery pack output, that is, 10.82 kW. The final efficiency value of the studied electric vehicle drive system was estimated as 43.44%. This is a typical value for such constructions based on the powerful BLDC motors and the high voltage battery packs.

Fig. 5 shows the heat losses in the BLDC motor during intensive vehicle exploitation which have an important impact on the total electric drive system efficiency. Moreover, similar losses are present in the motor controller which is placed on the top side of the battery compartment near the vehicle saddle (Fig. 6). It should be noted that the original motor has undergone some technical modifications to increase its operating temperature range. These are, firstly, replacement of 4 mm² power cables to 8 mm², which resulted in heat losses reduction, and hence, increased power transmitted to the motor. Secondly, replacement of the original motor windings to the ones with a thicker insulation, that is, two layers of polyurethane varnish and an external coating of polyamide varnish. Thirdly, the two small fans were installed inside the motor to create air circulation. Fourth, the aluminium heat sink was mounted on the motor housing for better heat dissipation. The actual temperature inside the motor is provided by the PT100 sensor, which transmits this information to the controller.

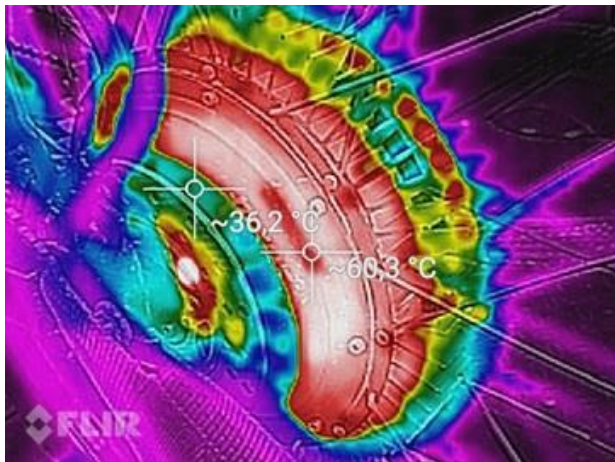


Fig. 5. Temperature of the BLDC motor during chassis dynamometer tests

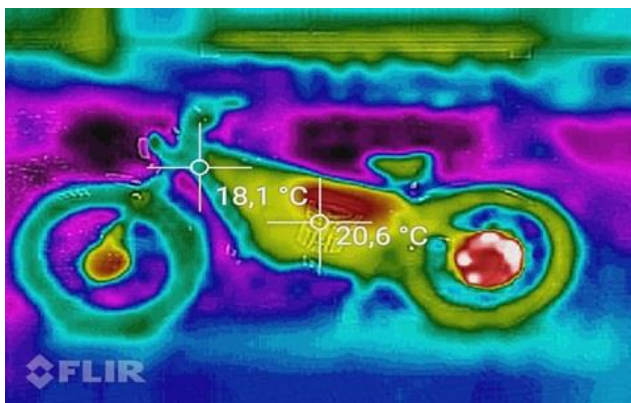


Fig. 6. Distribution of heat losses in the light two-wheeled electric vehicle

Thanks to these modification, the motor operating temperature range increased from 150°C to about 200°C and the operating voltage increased to about 240 V. Nevertheless, due to security reasons, the motor controller was programmed to maintain the motor temperature below 120°C. Exceeding this temperature results in a noticeable power reduction, which has to be controlled during the tests.

Apart from the heat losses present in the vehicle drive system, one has to take into account the losses associated with the power transmission between the vehicle and the chassis dynamometer. In order to avoid a drive wheel slipping on the rollers, the vehicle must be tightly pressed against the rollers, which introduces additional tire deflection losses.

6. ELECTRIC VEHICLE CHARGING BALANCE

Charging of the electric vehicle batteries is also a process that consumes some additional amount of energy (Khan and Choi, 2018; Ahn and Lee, 2019). In order to measure an efficiency of charging process, the battery pack was discharged to 84.85 V, which is the 84.18% of its maximum voltage. The nominal capacity of the SONY VTC5 cell is 2600 mAh, but in reality, this value oscillates around 2560 mAh when the cell is new. The cut-off voltage of this cell is 2 V, which is interpreted as 0% of charge. Nevertheless, frequent discharging to such a voltage leads to an irreversible damage of the cell. In practice, the cell loses its operating properties at about 2.5 V and a significant loss of its capacity is already observed at a voltage of about 3.3 V (Test of Sony US18650VTC5 2600mAh (Green)). Therefore, devices such as BMS (Battery Management System) and on-board computer system were programmed to control the voltage to a minimum limit of 3.5 V to maintain the maximum battery life.

Tab. 3. Charging test results

Parameter	Device 1	Device 2
Voltage before charging	84.85 V	
Voltage after charging	100.8 V	
Charging energy/ battery capacity	2.64 kWh / 28.9 Ah	2.92 kWh / 29.2 Ah

For the charging test, two devices were used. The first (Device 1) was plugged in between the battery charging socket and the vehicle charger output while the second (Device 2) was plugged in directly to the power socket and the vehicle charger input. The battery charging time was 8 hours and 38 minutes and cost about €0.41. Tab. 3 summarizes values measured during the test. One has to notice that the real capacity of the battery pack decreased significantly from nominal 39 Ah to about 29 Ah, which is a result of natural cells ageing used intensively for more than 2 years. Considering the data from the Tab. 3, the charging efficiency was estimated at 90%.

7. CONCLUSIONS

Responding to an increased interest in electric vehicles design and operation, the authors have proposed the procedures for light two-wheeled electric vehicle energy balance investigation using a

car chassis dynamometer. These are: the energy consumption analysis, the overall efficiency test of the electric drive system and the electric vehicle charging balance studies. Regarding the first of above mentioned procedures one can conclude that the use of the car chassis dynamometer allows to investigate the energy consumption only for some range of speeds. This issue is closely related to the studied vehicle performances, that is, the more powerful the vehicle is, the better coherence of the analysis can be obtained. On the other hand, during efficiency test of light vehicle electric drive system, the excessive power can cause the wheel to slide on the dynamometer rollers, which distorts the results. The vehicle should be firmly attached to the test stand and the additional tire deflection losses should be taken into consideration.

Being conscious about the inconveniences and limits of the car chassis dynamometer (i.e., important rollers inertia factor) for light electric vehicles testing as well as about the advantages of such approach, one can prepare valuable testing procedures.

REFERENCES

1. **Ahn J.-H., Lee B.K.** (2019) High-Efficiency Adaptive-Current Charging Strategy for Electric Vehicles Considering Variation of Internal Resistance of Lithium-Ion Battery, *IEEE Transactions on Power Electronics*, 34(4), 3041–3052.
2. **Barański R., Galewski M., Nitkiewicz S.** (2019) The study of Arduino Uno feasibility for DAQ purposes, *Diagnostyka*, 20(2), 33–48.
3. **Bertoluzzo M., Buja G.** (2011) Development of Electric Propulsion Systems for Light Electric Vehicles, *IEEE Transactions on Industrial Informatics*, 7(3), 428–435.
4. **Chen M., Jin Z.a, Lu Q., Ye X., Fang M., Qin K.** (2010) A chassis dynamometer laboratory for fuel cell hybrid vehicles and the hydrogen consumption measurement system, in *2010 IEEE Vehicle Power and Propulsion Conference*. IEEE, 1–5.
5. **Chu L., Zhou F., Guo J.** (2011) Investigation of cycle life of li-ion power battery pack based on LV-SVM, in *2011 International Conference on Mechatronic Science, Electric Engineering and Computer (MEC)*. IEEE, 1602–1605.
6. **Commission Delegated Regulation (EU) No 134/2014** of 16 December 2013 supplementing Regulation (EU) No 168/2013 of the European Parliament and of the Council with regard to environmental and propulsion unit performance requirements and amending Annex V the (2013).
7. **Dobrucky B., Kascak S., Prazenica M., Jarabicova M.** (2019) Improving Efficiency of Hybrid Electric Vehicle Using Matrix Converters, *Elektronika ir Elektrotechnika*, 25(4), 29–35.
8. **Fei F., Rengui L., Guoliang W., Chunbo Z.** (2012) A measuring method of available capacity of Li-Ion series battery pack, in *2012 IEEE Vehicle Power and Propulsion Conference*, IEEE, 389–394.
9. **Ho T.Y., Chen W. C., Chiang C. H., Hung W. C., Chen M. S.** (2014) The Design of Motor Drive with Speed Control for an Electric Bicycle, in *2014 International Symposium on Computer, Consumer and Control*. IEEE, 864–867.
10. **Khan A.B., Choi W.** (2018) Optimal Charge Pattern for the High-Performance Multistage Constant Current Charge Method for the Li-Ion Batteries, *IEEE Transactions on Energy Conversion*, 33(3), 1132–1140.
11. **Kim N., Rousseau A., Rask E.** (2016) Parameter Estimation for a Lithium-Ion Battery From Chassis Dynamometer Tests, *IEEE Transactions on Vehicular Technology*, 65(6), 4393–4400.
12. **Kolator B., Racewicz S., Olszewski A.** (2018) Bench tests results of the traction parameters of the light two-wheeled electric vehicle, *IOP Conference Series: Materials Science and Engineering*, 421(2), 022015.
13. **Kumar B.V.R., Sivakumar K.** (2017) Design of a new switched-stator BLDC drive to improve the energy efficiency of an electric vehicle, in *2017 IEEE International Conference on Industrial Technology (ICIT)*. IEEE, 532–537.
14. **Kumar B. V. R., Sivakumar K., Karunanidhi S.** (2017) A novel configuration of regenerative braking system to improve the energy efficiency of an electric vehicle with Dual-Stator Dual-Rotor BLDC motor, in *2017 IEEE Transportation Electrification Conference (ITEC-India)*, IEEE, 1–4.
15. **Laitinen H., Lajunen A., Tammi K.** (2017) Improving Electric Vehicle Energy Efficiency with Two-Speed Gearbox, in *2017 IEEE Vehicle Power and Propulsion Conference (VPPC)*, IEEE, 1–5.
16. **Li Y., Hu J., Chen F., Liu S., Yan Z., He Z.** (2018) A New-Variable-Coil-Structure-Based IPT System With Load-Independent Constant Output Current or Voltage for Charging Electric Bicycles, *IEEE Transactions on Power Electronics*, 33(10), 8226–8230.
17. **Lim D.-K., Cho Y.-S., Ro J.-S., Jung S.-Y., Jung H.-K.** (2016) Optimal Design of an Axial Flux Permanent Magnet Synchronous Motor for the Electric Bicycle, *IEEE Transactions on Magnetics*, 52(3), 1–4.
18. **Lin J., Schofield N., Emadi A.** (2015) External-Rotor 6–10 Switched Reluctance Motor for an Electric Bicycle, *IEEE Transactions on Transportation Electrification*, 1(4), 348–356.
19. **Park M., Seo M., Song Y., Kim S.** (2019) Capacity Estimation of Li-ion battery using Constant Current Charging Voltage, in *2019 IEEE Asia Pacific Conference on Circuits and Systems (APCCAS)*. IEEE, 202–204.
20. **Racewicz S., Kazimierczuk P., Kolator B., Olszewski A.** (2018) Use of 3 kW BLDC motor for light two-wheeled electric vehicle construction, *IOP Conference Series: Materials Science and Engineering*, 421(4), 042067.
21. **Saponara S., Lee C. H. T., Wang N. X., Kirtley J. L.** (2020) Electric Drives and Power Chargers: Recent Solutions to Improve Performance and Energy Efficiency for Hybrid and Fully Electric Vehicles, *IEEE Vehicular Technology Magazine*, 15(1), 73–83.
22. **Sarioglu B., Morris C. T., Han D., Li S.** (2017) Driving Toward Accessibility: A Review of Technological Improvements for Electric Machines, Power Electronics, and Batteries for Electric and Hybrid Vehicles, *IEEE Industry Applications Magazine*, 23(1), 14–25.
23. **Test of Sony US18650VTC5 2600mAh (Green)** (no date). Available at: https://lygte-info.dk/review/batteries2012/Sony_US18650VTC5_2600mAh_%28Green%29_UK.html (Accessed: 30 December 2019).
24. **UPRD** (1997) Act of June 20, 1997, Road Traffic Law, *Journal of Laws*, (in Polish), 3113. Available at: <http://prawo.sejm.gov.pl/isap.nsf/download.xsp/WDU19970980602/U/D19970602Lj.pdf> (Accessed: 25 April 2018).
25. **Zaghari B., Stuijks A., Weddell A. S., Beeby S.** (2020) Efficient Energy Conversion in Electrically Assisted Bicycles Using a Switched Reluctance Machine Under Torque Control, *IEEE Access*, 8, 202401–202411. d

We would like to thank Prof. Bronisław Kolator and Dr Jarosław Gonera from the Department of Construction, Operation of Vehicles and Machines of the University of Warmia and Mazury in Olsztyn for their assistance and help during chassis dynamometer tests.

EVALUATION OF THE INFLUENCE OF THE SUPPLY PRESSURE ON FUNCTIONAL PARAMETERS OF THE IMPULSE LOW-PRESSURE GAS-PHASE INJECTOR

Dariusz SZPICA*, **Andrzej BORAWSKI***, **Grzegorz MIECZKOWSKI***, **Michał KUSZNIER****,
Mohamed M. AWAD***, **Adel M. SADIK******, **Mohammed SALLAH*******

*Faculty of Mechanical Engineering, Białystok University of Technology, 45C Wiejska Str., 15-351 Białystok, Poland

**Doctoral School, Białystok University of Technology, 45A Wiejska Str., 15-351 Białystok, Poland

***Mechanical Power Engineering Department, Faculty of Engineering, Mansoura University, Mansoura 35516, Egypt

****Physics Department, Faculty of Science, Mansoura University, Mansoura 35516, Egypt

*****Physics Department, Faculty of Science, Mansoura University, Mansoura 35516, Egypt,
 Higher Institute for Engineering and Technology, New Damietta, Egypt

d.szpica@pb.edu.pl, a.borawski@pb.edu.pl, g.mieczkowski@pb.edu.pl, michal.kuszniér@gmail.com,
m_m_awad@mans.edu.eg, sadikama@mans.edu.eg, msallahd@mans.edu.eg

received 23 November 2020, revised 15 January 2021, accepted 19 January 2021

Abstract: The article presents research results referring to the influence of supply pressure on the functional parameters of the impulse low-pressure gas-phase injector. The study was done on the original stand for flow test of gas-phase injectors. In the indirect evaluation, with the initial parameters and the length of the forced impulse, the current line, acceleration and pressure sensor courses were used. Apart from the volumetric flow rate, the analysed parameters were the time periods of the injector opening and closing process. Those time segments were composed of response time and opening/closing time, the sum of which gives time of full opening. Functional relationships describing the volumetric flow rate, time of full opening and closing are presented, which are helpful not only in comparative tests of different injectors, but also in modelling the operation of gas injector or algorithms of gas supply control system. The reference to the volumetric flow rate allowed to indicate possible causes of variability of this parameter depending on the supply pressure.

Key words: Mechanical engineering, combustion engines, fuel supply, alternative fuel injector, research

1. INTRODUCTION

In recent years, we have seen legislative efforts to reduce exhaust emissions from engines used in transport (WLTP, 2019). This is generally known as greenhouse gases (GHGs) (Clairotte et al., 2020). Although some of the regulations are European, manufacturers around the world are adapting their engines to the requirements of the next Euro emission limits, considering distribution issues (Kim et al., 2020). In 2018, CO₂ emissions during a European car certification test could reach 120.5 g/km. Since 2020, this has been reduced to 95 g/km. In a longer-term perspective, further reductions by 15% in 2025 and 37.5% in 2030 are planned (García et al., 2020). Such actions will most probably exclude the possibility of using combustion engines as the only source of vehicle propulsion. However, they may still be used in hybrid systems with different connection configurations (Raslavičius et al., 2015, 2017). A separate issue proposed for inclusion in the future Euro VII standard is the unification of exhaust emissions for cars, vans, and trucks. There are still matters of emissions for machines and non-road vehicles (Waluś et al., 2018; Warguła et al., 2018).

In Europe, the most popular alternative fuel used in cars and vans is liquefied petroleum gas (LPG) (Raslavičius et al., 2014). Alternative fuels are listed in the European Union Directive (2014/94/EU) (Council of the European Union, 2014). Interest in using LPG/CNG in forklift and working machinery engines is also observed (Warguła et al., 2020, 2020a).

Taking into consideration the emission regulations, more precise algorithms are required to monitor the performance of the internal combustion engine, and in particular towards the gas fuel supply (Dziewiatkowski et al., 2020). More precise executive modules are also required (Szpica, 2016). Additionally, it is necessary to know the working characteristics of the components in relation to variable input parameters.

The impulse low-pressure gas-phase injectors, which are installed in alternative combustion engine supply systems, are characterized by their diverse design. Out of many parameters, which can describe the operation of the gas injector, the volumetric flow rate (Czarnigowski, 2012) and the time periods associated with the movement of the actuator (Duk and Czarnigowski, 2012; Szpica, 2018) are considered as basic.

For the functional evaluation of the gas injectors, computational methods used for modelling the operation of engines and their components may be used:

- 0-D modelling (Baldi et al., 2015; Feng et al., 2019; Ngayihi Abbe et al., 2015; Polášek et al., 2002);
- 1-D modelling (Cerri et al., 2006; Da Silva Trindade and Dos Santos, 2016; Sawant and Bari, 2017; Pauras Sawant et al., 2018);
- 3-D modelling (Broatch et al., 2019; Buhl et al., 2017; Kosmadakis et al., 2012; Mohammadi et al., 2012).

Calculation methods are becoming essential when prototyping new construction solutions. Analytical models are used here (Brumercik et al., 2020; Szpica and Kuszniér, 2020). For strength

and thermal evaluation, the finite element method (FEM) is widely used (Bensetti et al., 2006; Borawski et al., 2020, 2021), while in the flow part, computational fluid dynamics (CFD) (Czarnigowski et al., 2007, 2009; Marčić et al., 2015; Szpica, 2015). A very difficult computational problem is the phenomenon of circuit magnetism with an injector drive coil (Passarini and Nakajima, 2003; Passarini and Pinotti, 2003; Taghizadeh et al., 2009). In gas injectors, as in other fuel injectors, there are high hopes for piezo-electric propulsion (Mieczkowski, 2019; Mieczkowski et al., 2020; Pogulyaev et al., 2015; Satkoski et al., 2009).

Mathematical modelling allows for the approximation of real processes, but in effect, experimental verification is required. For testing gas injectors, experimental methods used for functional analysis of injectors for different fuels can be applied:

- high speed cameras (Aleiferis et al., 2010; Jang et al., 2000; Panão and Moreira, 2005);
- optical laser (Kakuhou et al., 1999; Leach et al., 2007; Robart et al., 2001);
- light fluorescence absorption (Aleiferis and Van Romunde, 2013; Leach et al., 2007);
- current in the power line (Duk and Czarnigowski, 2012; Szpica, 2018);
- heat flow sensors (Serras-Pereira et al., 2013);
- acceleration sensors (Czarnigowski, 2012; Szpica, 2018);
- pressure sensors (Duk and Czarnigowski, 2012; Szpica, 2018);
- lift sensors (Ambrozik and Kurczyński, 2008; Szpica, 2018);
- optical sensors (Walaszuk and Busz, 2013);
- gravimetric method (Szpica and Czaban, 2014);
- ‘fuel tank refill’ method (Szpica and Czaban, 2014).

The methods presented above differ in the level of complexity, the required equipment, as well as the way they interfere with the executive parts. The use of direct methods gives the most precise picture of the processes, but this often involves interfering with the working system, which must be repaired at a later stage. As shown in (Szpica, 2018) indirect methods, which exclude interference with the working elements of the gas injector, also allow for a correct assessment of functional parameters.

On the one hand, the emission regulations and, on the other hand, the expansion of the control algorithms within the engine require knowledge not only of the static characteristics, but also of their changes when adjusting the input parameters. The main feature of the injector, which is the volumetric flow rate, has been improved by time intervals for opening and closing the injector, filling the research gap in this area. The aim of the study was to develop functional dependencies describing the variability of the analysed parameters that may be helpful in the analysis of engine transitions as well as in creating mathematical models.

2. THE RESEARCH OBJECT

The object of the research was STAG AC W02 – four-section injection rail LPG/CNG (Fig. 1a). W02 is the impulse low-pressure gas-phase injector. In the lack of power supply, plunger 1 (Fig. 1b) is pressed against the socket by spring 3 and gas flow is not possible. When an electrical impulse arises in circuit 2, the electromagnetic force raises plunger 1 and the gas flow is realized according to the red arrows (Fig. 1). When the electric impulse disappears, spring 3 moves plunger 1 downwards, making the flow impossible.



Fig. 1. STAG AC W02 – four-section injection rail LPG/CNG: a – picture; b – scheme: 1 – plunger, 2 – electromagnetic circuit, 3 – spring, red arrows point at the flow direction

Basic technical data of the STAG AC W02 – four-section injection rail LPG/CNG have been presented in Tab. 1.

Tab. 1. Basic technical data of the Valtek Rail Type 30 gas injector
Data taken from (AC, 2020)

Parameter	Value
max flow rate at 1.2 bar	120 NL/min
coil resistance	1.9 Ω
nozzle size	(min 1.5/max 2.8) mm
opening time/closing time	(2 / 1) ms
operating temperature	(-20 ÷ 120)°C
max working pressure	400 kPa

3. THE RESEARCH METHODOLOGY

The tests were carried out on the original gas injector flow test stand. For safety reasons, the tests were conducted using air instead of LPG/CNG (Fig. 2). In the evaluation of functional parameters, indirect methods were used without interfering with the injector's working system.

Compressed air from air supply 1 flows through the air preparation 2 system to the buffer tank 3. The buffer tank is designed to accumulate sufficient air to prevent temporary pressure drops. The air continues to flow through the tested injector 4. The impulse action of the injector is controlled by a pulse generator 5.

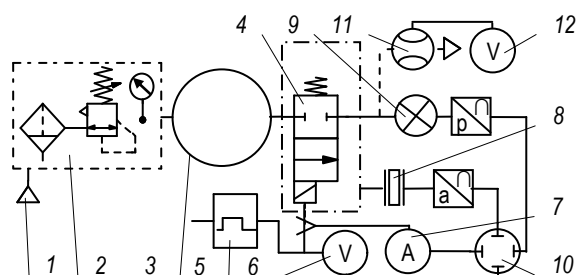


Fig. 2. The scheme of the measurement stand: 1 – air supply, 2 – air preparation system, 3 – buffer tank, 4 – tested injector, 5 – pulse generator (based STAG ECU), 6 – voltage connector; 7 – current lines, 8 – accelerometer, 9 – pressure gauge, 10 – oscilloscope, 11 – mass flow meter, 12 – multimeter

In the measurement section that assesses the power supply, there is a voltage connector 6 and current line 7. The return positions of the injector plunger are accompanied by vibrations, which are read out by the accelerometer 8. The air stream coming out of the injector under test goes to the pressure sensor 9, which estimates the operating cycle in terms of flow-through. The design and operation of pressure sensor 9 is described in Szpica (2018).

Signals are stored in oscilloscope 10. In addition, it is possible to measure the average injector output through the mass flow meter 11 and multimeter Brymen 907 12. Basic technical data of the measurement equipment have been presented in Tab. 2.

By using an oscilloscope, it was possible to register 4 different channels. Assuming that the voltage supply to the injector is forced, the corps acceleration, current line, and pressure are additionally recorded. The registered values were saved to *.csv file. The results were processed using software created in Guide

Matlab-Simulink. A Butteworth low pass filter (Yang et al., 2005) was used to filter the waveforms. As a result, it was possible to read the times describing the injector reaction when opening and closing (Fig. 3). Based on the 'breakthrough' of the current line, only the time to full opening (t_{fo}) could be read. The acceleration course and the pressure course made it possible to read both response of opening or closing time (t_{or} , t_{cr}) and opening time (t_o) or closing time (t_c). By adding up response time and opening/closing time as a result, we get time to full opening/closing.

Tab. 2. Parameters of the measuring equipment

Parameter	Measurement device	Response time	Range	Output signal	Accuracy
current	HAMEG HZ050	< 1 μ s	\pm 30 A	100 mV/A	1%
acceleration	KELAG KAS903-02A	< 1 ms	\pm 12 g	(0.5–4.5) V	0.005 g
pressure	MPXH6400A	< 1 ms	(20–400) kPa	(0–5) V	0.25%
mass flow	BRONKHORST F-113AC-M50-ABD-00-V	< 0.5 s	(0–300) Nl/min	(0–5) V	0.5%
voltage	RIGOL RP1500A	bandwidth ~ 150 MHz; damping factor – 10:1			
record	RIGOL MSO4014	bandwidth – 100 MHz; real-time sample rate – up to 4 GSa/s			

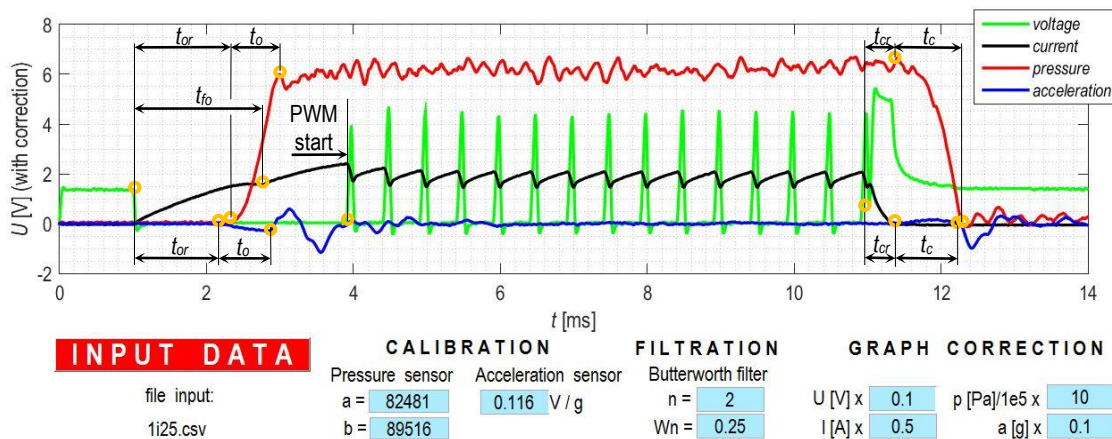


Fig. 3. Example courses recorded during the measurement (injection impulse 10 ms, PWM after 3 ms): t – time; index: or – of opening response, o – of opening, fo – of full opening, cr – of closing response, c – of closing

4. RESULTS OF THE MEASUREMENT

In the initial part of the study, the volumetric flow rate was determined using the flow meter. The supply pressure regulated in the scope (0.5–2.5) e5 Pa. The pulse generator has been set with constant parameters: frequency of impulses: 1000 min⁻¹; injection time: 10 ms; signal modulation 90% PWM at 3 ms; voltage: 14 V; outlet nozzle diameter: 3.2 mm.

The variability of volumetric flow rate relative to supply pressure was presented in the Fig. 4. The relation $Q = f(p)$ was approximated with the polynomial of 3rd degree:

$$Q = -1.1612p^2 + 13.9160p + 1.2933 \quad (R^2 = 99.9\%) \quad (1)$$

It was found that a 9-fold increase in supply pressure results in an approximate 6-fold increase in volumetric flow rate, the ratio is not proportional. In the study (Czarnigowski, 2012), the results of the volumetric flow rate tests of constructively similar injectors were presented. Despite the differences in values, the variability of the tested parameters correlates with the one presented in this study.

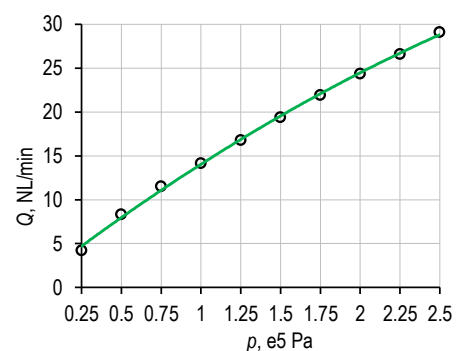


Fig. 4. The relation of the volumetric flow rate and the supply pressure for the tested injector

In order to maintain the necessary relationship towards comparison, the variability of time characterizing the injector operation was also approximated with the polynomial of 3rd degree. Functional dependencies have been determined for time to full opening and full closing. Full opening time based on the current course was described (Fig. 5a)

$$t_{fo} = -0.0358p^2 + 0.3066p + 1.4355 \quad (R^2 = 99.7\%) \quad (2)$$

and the acceleration sensor course

$$t_{fo} = -0.0485p^2 + 0.3263p + 1.5380 \quad (R^2 = 99.5\%) \quad (3)$$

also the pressure sensor course

$$t_{fo} = -0.0200p^2 + 0.2308p + 1.7478 \quad (R^2 = 99.1\%) \quad (4)$$

In case of evaluation of the injector closing process, it is im-

possible to evaluate it on the basis of the current line. Therefore, the ratios defining time to full closing are described based on the acceleration sensor course (Fig. 5d)

$$t_{fc} = 0.0109p^2 - 0.1102p + 2.3383 \quad (R^2 = 95.0\%) \quad (5)$$

and the pressure sensor course

$$t_{fc} = 0.0333p^2 - 0.0531p + 2.3498 \quad (R^2 = 82.9\%) \quad (6)$$

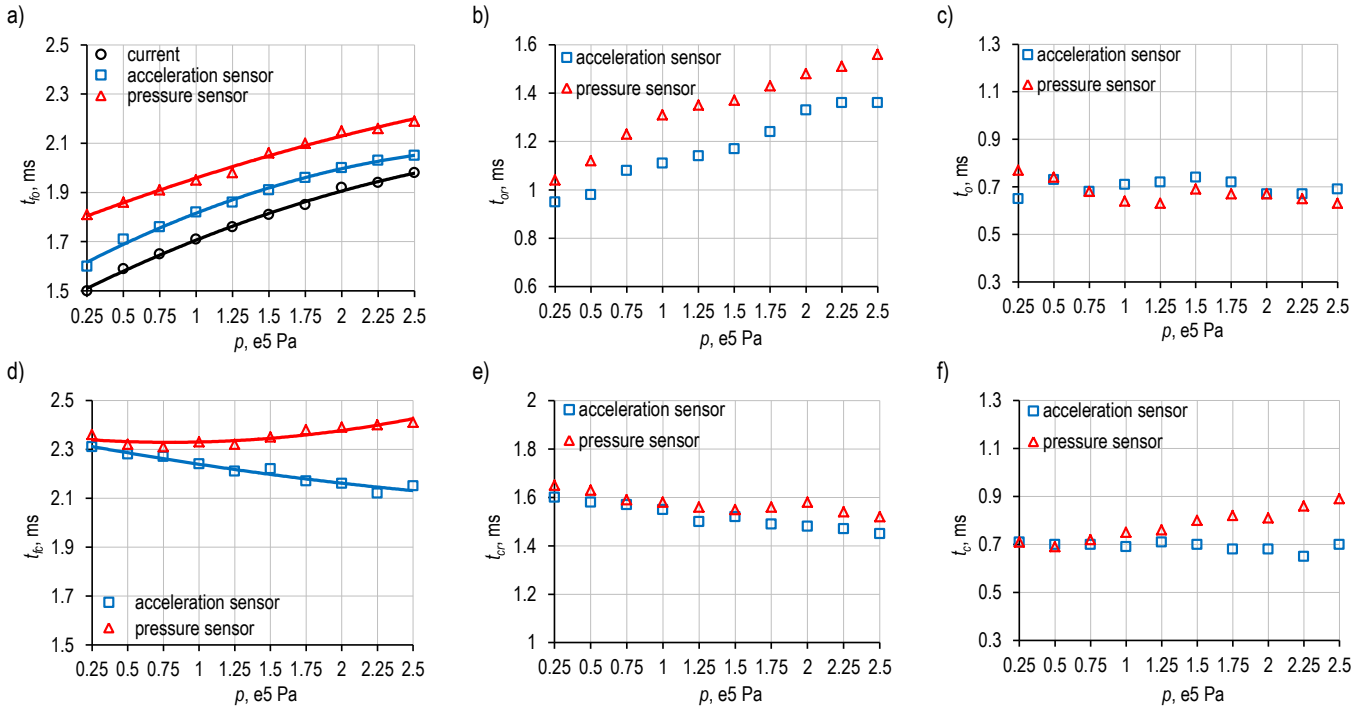


Fig. 5. The results of the research: a – time to full opening, b – opening response time, c – opening time, d – time to full closing, e – response closing time, f – closing time

In the case of time to full opening variability, it was found that a 9-fold increase in supply pressure gives time to full opening increments in the range 20–32%, current line – 32%, acceleration sensor – 28% and pressure sensor – 21% accordingly. Analysing Fig. 5b and c, the dominant influence of opening response time is observed. It results from the necessity to overcome the force from the differential pressure above and below the piston by the electromagnetic force of the drive. The opening process itself is characterized by similar time values, due to the disappearance of the pressure difference under and over the piston.

The closing process of the injector and the associated characteristic times are more difficult to estimate using indirect methods. While the acceleration sensor shows a 7.5% decrease in time to full closing, the pressure sensor shows a 2% increase. In this case, the accelerator sensor should be considered as representative, because in the pressure sensor and its course of pressure in the process of closing the injector, there is still a phase of air stream expansion between the injector and the sensor, as described in Szpica (2018). On the basis Fig. 5e and f for the acceleration sensor, it is possible to state the major influence of response time on time to full closing.

The presented results of research on the influence of supply pressure on functional parameters of the impulse low-pressure gas-phase injector correlate with the research and conclusions from the experimental studies presented in (Czarnigowski, 2010, 2014). It was found there that the supply pressure has an impact

on the opening response time because, as already mentioned, the electromagnetic force has to overcome the greater pressure difference under and over the piston. However, there was no confirmation with reference to the characteristic times of the opening and closing process. An analysis of opening and closing times of the injector can be helpful in developing an algorithm to control the operation of the supply system at variable gas pressure regarding the change in injection angle.

The results obtained in the course of the research are also the base for the verification of mathematical models describing the operation of the gas injector, for example Szpica and Kuszniar (2020).

5. CONCLUSIONS

The studies presented in the article and their analysis were intended to evaluate the influence of supply pressure on the functional parameters of the impulse low-pressure gas-phase injector. The parameters evaluated were volumetric flow rate and time intervals describing the process of opening and closing the injector. The conclusions are as follows,

- A 9-fold increase of supply pressure gives a 6-fold increase in the volumetric flow rate. The relation was approximated with the polynomial of 3rd degree;

- Changes in supply pressure in the scope covered by the research plan result in time to full opening increases of a range 20–32%.
- The opening response time has a more significant impact on the time to full opening than opening time.
- The acceleration sensor shows a 7.5% decrease in time to full closing, with a significantly higher impact on response time than closing time.
- The pressure sensor gives a 2% increase in time to full closing, but its course during closing process is not fully representative, which takes into account the expansion phase of the stream between injector and sensor.

The study results presented in the article fill the research gap regarding the evaluation of the influence of supply pressure on the examined time periods. They are also helpful in creating mathematical models describing the operation of the gas injector or planning algorithms for controlling the gas supply system. In the next stage, it is planned to verify the research presented in the study by the direct method using the displacement sensor.

REFERENCES

1. **AC** (2020), *STAG Autogas Section*. Retrieved May 10, 2020, from <https://www.ac.com.pl/en>.
2. **Aleiferis P. G., Serras-Pereira J., Augoye A., Davies T. J., Cracknell R. F., Richardson D.** (2010), Effect of fuel temperature on in-nozzle cavitation and spray formation of liquid hydrocarbons and alcohols from a real-size optical injector for direct-injection spark-ignition engines, *International Journal of Heat and Mass Transfer*, 53(21–22): 4588–4606.
3. **Aleiferis P. G., Van Romunde Z. R.** (2013), An analysis of spray development with iso-octane, n-pentane, gasoline, ethanol and n-butanol from a multi-hole injector under hot fuel conditions, *Fuel*, 105: 143–168.
4. **Ambrozik A., Kurczyński D.** (2008), Analysis of fast-changing quantities in the AD3.152 UR engine running of mineral fuel, plant fuel and their blends, *Motrol*, 10: 11–22.
5. **Baldi F., Theotokatos G., Andersson K.** (2015), Development of a combined mean value-zero dimensional model and application for a large marine four-stroke Diesel engine simulation, *Applied Energy* 154: 402–415.
6. **Bensetti M., Le Bihan Y., Marchand C.** (2006), Development of an hybrid 3D FEM for the modeling of micro-coil sensors and actuators, *Sensors and Actuators, A: Physical*, 129(1–2): 207–211.
7. **Borawski A., Szpica D., Mieczkowski G., Awad M. M., Shalby R. M., Sallah M.** (2021), Simulation study of the vehicle braking process with temperature dependent coefficient of friction between brake pad and disc, *Heat Transfer Research*, 52(2): 1–11.
8. **Borawski A., Szpica D., Mieczkowski G., Borawska E., Awad M. M., Shalby R. M., Sallah M.** (2020), Theoretical analysis of the motorcycle front brake heating process during high initial speed emergency braking, *Journal of Applied and Computational Mechanics*, 6(SI): 1431–1437.
9. **Broatch A., Olmeda P., Margot X., Escalona J.** (2019), New approach to study the heat transfer in internal combustion engines by 3D modelling, *International Journal of Thermal Sciences*, 138: 405–415.
10. **Brumercik F., Lukac M., Caban J., Krzysiak Z., Glowacz A.** (2020), Comparison of selected parameters of a planetary gearbox with involute and convex-concave teeth flank profiles, *Applied Sciences (Switzerland)*, 10(4): 1417.
11. **Buhl S., Gleiss F., Köhler M., Hartmann F., Messig D., Brücker C., Hasse C.** (2017), A combined numerical and experimental study of the 3D tumble structure and piston boundary layer development during the Intake stroke of a gasoline engine, *Flow, Turbulence and Combustion*, 98: 579–600.
12. **Cerri T., Onorati A., Mattarelli E.** (2006), 1D engine simulation of a small HSDI diesel engine applying a predictive combustion model, *Journal of Engineering for Gas Turbines*, 130(1): 012802.
13. **Claïrotte M., Suarez-Bertoa R., Zardini A. A., Giechaskiel B., Pavlovic J., Valverde V., Ciuffo B., Astorga C.** (2020), Exhaust emission factors of greenhouse gases (GHGs) from European road vehicles, *Environmental Sciences Europe*, 32(1): 125.
14. **Council of the European Union** (2014), Council Directive 2014/94/EU of 22 October 2014 on the deployment of alternative fuels infrastructure. In *Official Journal of the European Union*.
15. **Czarnigowski J.** (2010), The impact of supply pressure on gas injector expenditure characteristics, *Silniki Spalinowe*, 49(2): 18–26.
16. **Czarnigowski J.** (2012), *Theoretical and empirical study of modeling a pulse gas injector*. Wydawnictwo Politechniki Lubelskiej, Lublin.
17. **Czarnigowski J.** (2014), Experiments on the effect of pressure and voltage supply on pulse injector opening time, *SAE Technical Papers*, 2014-01-2560.
18. **Czarnigowski J., Jakliński P., Wendeker M., Pietrykowski K., Grabowski Ł.** (2009), The analyses of the phenomena inside a CNG flap-valve injector during gas flow, *Combustion Engines*, 136(1): 10–18.
19. **Czarnigowski J., Wendeker M., Jakliński P., Rola M., Grabowski Ł., Pietrykowski K.** (2007), CFD model of fuel rail for LPG systems, *SAE Technical Papers*, 2007-01-2053.
20. **Da Silva Trindade W. R., Dos Santos R. G.** (2016), Combustion modeling applied to engines using a 1D simulation code, *SAE Technical Papers*, 2016-36-0347.
21. **Duk M., Czarnigowski J.** (2012), The method for indirect identification gas injector opening delay time, *Przegląd Elektrotechniczny*, 88(10 B): 59–63.
22. **Dziwiątkowski M., Szpica D., Borawski A.** (2020), Evaluation of impact of combustion engine controller adaptation process on level of exhaust gas emissions in gasoline and compressed natural gas supply process, *Engineering for Rural Development*, 19: 541–548.
23. **Feng Y., Wang H., Gao R., Zhu Y.** (2019), A zero-dimensional mixing controlled combustion model for real time performance simulation of marine two-stroke diesel engines, *Energies*, 12(10): 2000.
24. **García A., Monsalve-Serrano J., Villalta D., Guzmán-Mendoza M.** (2020), Methanol and OME_x as fuel candidates to fulfill the potential EURO VII emissions regulation under dual-mode dual-fuel combustion, *Fuel*, 287: 119548.
25. **Jang C., Kim S., Choi S.** (2000), An experimental and analytical study of the spray characteristics of an intermittent air-assisted fuel injector, *Atomization and Sprays*, 10(2): 199–217.
26. **Kakuhou A., Urushihara T., Itoh T., Takagi Y.** (1999), Characteristics of mixture formation in a direct injection SI engine with optimized in-cylinder swirl air motion, *Journal of Engines*, 108: 550–558.
27. **Kim H. J., Lee S. H., Kwon S. I., Park S., Lee J., Keel J. H., Lee J. T., Park S.** (2020), Investigation of the emission characteristics of light-duty diesel vehicles in Korea based on EURO-VI standards according to type of after-treatment system, *Energies*, 13(18): 4936.
28. **Kosmadakis G. M., Rakopoulos C. D., Demuyneck J., De Paepel M., Verhelst S.** (2012), CFD modeling and experimental study of combustion and nitric oxide emissions in hydrogen-fueled spark-ignition engine operating in a very wide range of EGR rates, *International Journal of Hydrogen Energy*, 37(14): 10917–10934.
29. **Leach B., Zhao H., Li Y., Ma T.** (2007), Two-phase fuel distribution measurements in a gasoline direct injection engine with an air-assisted injector using advanced optical diagnostics, *Proceedings of the Institution of Mechanical Engineers, Part D: Journal of Automobile Engineering*, 221(6): 663–673.
30. **Marčić S., Marčić M., Praunseis Z.** (2015), Mathematical model for the injector of a common rail fuel-injection system, *Engineering*, 7: 307–321.
31. **Mieczkowski G.** (2019), Static electromechanical characteristics of piezoelectric converters with various thickness and length of piezoelectric layers, *Acta Mechanica et Automatica*, 13(1): 30–36.

32. **Mieczkowski G., Borawski A., Szpica D.** (2020), Static electromechanical characteristic of a three-layer circular piezoelectric transducer, *Sensors (Switzerland)*, 20(1), 222.
33. **Mohammadi A., Jazayeri A., Ziabasharhagh M.** (2012), Numerical simulation of direct injection engine with using porous medium, *Proceedings of the Spring Technical Conference of the ASME Internal Combustion Engine Division*, ICES2012-81150, pp. 785–795.
34. **Ngayih Abbe C. V., Nzengwa R., Danwe R., Ayissi Z. M., Obonou M.** (2015), A study on the 0D phenomenological model for diesel engine simulation: Application to combustion of Neem methyl ester biodiesel, *Energy Conversion and Management*, 89: 568–576.
35. **Panão M. R. O., Moreira A. L. N.** (2005), Flow characteristics of spray impingement in PFI injection systems, *Experiments in Fluids*, 39(2): 364–374.
36. **Passarini L. C., Nakajima P. R.** (2003), Development of a high-speed solenoid valve: an investigation of the importance of the armature mass on the dynamic response, *Journal of the Brazilian Society of Mechanical Sciences and Engineering*, 25(4): 329–335.
37. **Passarini L. C., Pinotti M.** (2003), A new model for fast-acting electromagnetic fuel injector analysis and design, *Journal of the Brazilian Society of Mechanical Sciences and Engineering*, 25(1): 95–106.
38. **Pogulyaev Y. D., Baitimerov R. M., Rozhdestvenskii Y. V.** (2015), Detailed dynamic modeling of common rail piezo injector, *Procedia Engineering*, 129: 93–98.
39. **Polášek M., Macek J., Takáts M., Vítek O.** (2002), Application of advanced simulation methods and their combination with experiments to modeling of hydrogen fueled engine emission potentials, *SAE Technical Papers*, 2002-01-0373.
40. **Raslavičius L., Azzopardi B., Keršys A., Starevičius M., Bazaras Ž., Makaras R.** (2015), Electric vehicles challenges and opportunities: Lithuanian review, *Renewable and Sustainable Energy Reviews*, 42: 786–800.
41. **Raslavičius L., Keršys A., Makaras R.** (2017), Management of hybrid powertrain dynamics and energy consumption for 2WD, 4WD, and HMMWV vehicles, *Renewable and Sustainable Energy Reviews*, 68: 380–396.
42. **Raslavičius L., Keršys A., Mockus S., Keršiene N., Starevičius M.** (2014), Liquefied petroleum gas (LPG) as a medium-term option in the transition to sustainable fuels and transport, *Renewable and Sustainable Energy Reviews*, 32: 513–525.
43. **Robart D., Breuer S., Reckers W., Kneer R.** (2001), Assessment of pulsed gasoline fuel sprays by means of qualitative and quantitative laser-based diagnostic methods, *Particle and Particle Systems Characterization*, 18(4): 179–189.
44. **Satkoski C. A., Shaver G. M., More R., Meckl P., Memering D.** (2009), Dynamic modeling of a piezoelectric actuated fuel injector, *IFAC Proceedings Volumes*, 42(26): 235–240.
45. **Sawant P., Bari S.** (2017), Combined effects of variable intake manifold length, variable valve timing and duration on the performance of an internal combustion engine, *ASME International Mechanical Engineering Congress and Exposition, Proceedings (IMECE)*, IMECE2017-70470, V006T08A052.
46. **Sawant Pauras, Warstler M., Bari S.** (2018), Exhaust tuning of an internal combustion engine by the combined effects of variable exhaust pipe diameter and an exhaust valve timing system, *Energies*, 11(6): 1545.
47. **Serras-Pereira J., Aleiferis P. G., Walmsley H. L., Davies T. J., Cracknell R. F.** (2013), Heat flux characteristics of spray wall impingement with ethanol, butanol, iso-octane, gasoline and E10 fuels, *International Journal of Heat and Fluid Flow*, 44: 662–683.
48. **Szpica D.** (2015), Simplified numerical simulation as the base for throttle flow characteristics designation, *Mechanika*, 21(2): 129–133.
49. **Szpica D.** (2016), The influence of selected adjustment parameters on the operation of LPG vapor phase pulse injectors, *Journal of Natural Gas Science and Engineering*, 34: 1127–1136.
50. **Szpica D.** (2018), Validation of indirect methods used in the operational assessment of LPG vapor phase pulse injectors, *Measurement: Journal of the International Measurement Confederation*, 118: 253–261.
51. **Szpica D., Czaban J.** (2014), Operational assessment of selected gasoline and LPG vapour injector dosage regularity, *Mechanika*, 20(5): 480–488.
52. **Szpica D., Kuszniar M.** (2020), Modelling of the low pressure gas injector operation, *Acta Mechanica et Automatica*, 14(1(51)): 29–35.
53. **Taghizadeh M., Ghaffari A., Najafi F.** (2009), Modeling and identification of a solenoid valve for PWM control applications, *Comptes Rendus – Mecanique*, 337(3): 131–140.
54. **Walaszyk A., Busz W.** (2013), Application of optical method for the analysis delay between control injector coil and beginning of the fuel injection, *Combustion Engines*, 154(3): 1038–1041.
55. **Waluś K. J., Warguła Ł., Krawiec P., Adamiec J. M.** (2018), Legal regulations of restrictions of air pollution made by non-road mobile machinery—the case study for Europe: a review, *Environmental Science and Pollution Research*, 25(4): 3243–3259.
56. **Warguła Ł., Kukla M., Lijewski P., Dobrzyński M., Markiewicz F.** (2020), Influence of the use of Liquefied Petroleum Gas (LPG) systems in woodchippers powered by small engines on exhaust emissions and operating costs, *Energies*, 13: 5773.
57. **Warguła Ł., Kukla M., Lijewski P., Dobrzyński M., Markiewicz F.** (2020a), Impact of Compressed Natural Gas (CNG) fuel systems in small engine wood chippers on exhaust emissions and fuel consumption, *Energies*, 13(24): 6709.
58. **Warguła Ł., Waluś K. J., Krawiec, P.** (2018), Small engines spark ignited (SI) for non-road mobile machinery- Review. *Transport Means - Proceedings of the International Conference, 2018-October*, 585–591.
59. **WLTP** (2019). *WLTP lab test*. Retrieved November 1, 2019, from <http://wltpfacts.eu/>.
60. **Yang W. Y., Cao W., Chung T.-S., Morris J.** (2005), Applied Numerical Methods Using MATLAB®. In *Applied Numerical Methods Using MATLAB®*.

This research was performed as a part of international cooperation under contract no. 147-UWBWM-2019 sign on 8th April 2019 between Bialystok University of Technology and Mansoura University, and it was financed through subsidy of the Ministry of Science and Higher Education of Poland for the discipline of mechanical engineering at the Faculty of Mechanical Engineering Bialystok University of Technology WZ/WM-IIM/4/2020.

ROBUST LFT-LPV H_∞ CONTROL OF AN UNDERACTUATED INVERTED PENDULUM ON A CART WITH OPTIMAL WEIGHTING FUNCTIONS SELECTION BY GA AND ES

Seif-EI-Islam HASSENI,* Latifa ABDOU**

*LMSE Laboratory, Electrical Engineering Department, University of Biskra, BP 145 RP, 07000, Biskra, Algeria

**LI3CUB Laboratory, Electrical Engineering Department, University of Biskra, BP 145 RP, 07000, Biskra, Algeria

seif.hasseni@univ-biskra.dz, l.abdou@univ-biskra.dz

received 23 March 2019, revised 18 January 2021, accepted 21 January 2021

Abstract: This article investigates the robust stabilization and control of the inverted pendulum on a cart against disturbances, measurement noises, and parametric uncertainties by the LFT-based LPV technique (Linear-Fractional-Transformation based Linear-Parameter-Varying). To make the applying of the LPV technique possible, the LPV representation of the inverted pendulum on a cart model is developed. Besides, the underactuated constraint of this vehicle is overcome by considering both degrees of freedom (the rotational one and the translational one) in the structure. Moreover, the selection of the weighting functions that represent the desired performance is solved by two approaches of evolutionary algorithms; Genetic Algorithms (GA) and Evolutionary Strategies (ES) to find the weighting functions' optimal parameters. To validate the proposed approach, simulations are performed and they show the effectiveness of the proposed approach to obtain robust controllers against external signals, as well as the parametric uncertainties.

Keywords: Inverted Pendulum on a cart, Robust Control, Underactuated Systems, Linear Parameter Varying Systems, H_∞

1. INTRODUCTION

1.1. Context and Motivations

The H_∞ control is one of the efficient control approaches on the robustness problem. Its objective is to minimize the gain between the external input signals and the so-called output signals (Zhou and Doyle, 1998). For the first time, it is developed for the Linear Time-Invariant systems (LTI). An extension of the H_∞ theory for the Linear Parameter Varying systems (LPV) has been developed. It has investigated the control synthesis and stability analysis of the LPV systems (Iwasaki and Shibata, 2001; Scherer, 2001; Wu, 2001). There are three kinds of LPV representations. First, the polytopic approach; the parameters are used at each vertex in the polytope. The main disadvantage of this approach is that exponential number of controllers are required, therefore, solving a large number of Linear Matrices Inequalities (LMI) and the computational effort is then expensive (Salhi et al., 2015; Liu, 2017). Second, gridding linearization; with this approach, there are simple controllers to implement, but, because the discretization on the parameters space is not well-defined (Wu et al., 1996), we may get infinity controllers. Third and last one; the LPV system with Linear Fractional Transformation (LFT) is common in separating the uncertainties from the nominal model in robust control. In this class, the same structure (LFT) is used with varying parameters. The main advantage of this approach is that minimal LMIs are solved to design a single controller. This controller has a self-scheduled structure around the parameters (Packard, 1994; Apkarian and Gahinet, 1995). The LPV theory shows efficiency in overcoming the complexity caused by the nonlinearity, especially the LFT representation, which we used in this paper. Moreover, researches were carried out about LPV systems in robust control because it's rigorous in robust stability. So, rather than divide the

nonlinear system in a set of LTI systems according to their operating points, the LPV system is developed by considering the nonlinearities as varying parameters, it is called here a quasi-LPV system (Shamma and Athans, 1991; Abbas et al., 2014).

On the other hand, the presented paper aims to investigate the design of a robust LPV controller for an inverted pendulum on a cart. The inverted pendulum is a classical benchmark, which can be considered as the simplest robotic system with one rigid body and one joint (Boubaker, 2013). The inverted pendulum could be considered as an ideal nonlinear system with a stable equilibrium point when the pendulum is in the pending position and an unstable equilibrium point when the pendulum is in the upright position. When the system is moved up from the pending position to the upright position, the model is strongly nonlinear with the pendulum angle. Besides, with two Degrees Of Freedom (DOF); and only the horizontal force, the inverted pendulum is the simplest Underactuated Mechanical System (UMS). Therefore, the inverted pendulum seems to be the platform for the implementation of different nonlinear and linear approaches; augmented PID controller (Siradjuddin et al., 2018), fuzzy logic control (El-Bardini and El-Nagar, 2014), sliding mode (Park and Chwa, 2009), predictive control (Ohhira and Shimada, 2017), and optimal control (Prasad et al., 2014).

1.2. Related Works

Many recent papers have interested the LPV techniques. For instance, in Tasoujian et al. (2020), the authors considered a parameter-varying model with delays to describe the dynamics of mean arterial blood pressure. Next, they designed a gain-scheduled output feedback LPV controller against disturbances and norm-bounded uncertainties to develop and regulate a real-time mean arterial blood pressure response of patients via time

delay LPV control technique. The LPV techniques are commonly used in sensible systems that need rigorous rejection of disturbances, uncertainties' effects, and faults like unmanned aerial vehicles (López-Estrada et al., 2016; Hasseni and Abdou, 2018). The authors of (Nguyen et al., 2020) constructed a conceptual model of narrow tilting vehicles in a polytopic LPV form, and they then proposed a static output feedback control method as the simplest structure to avoid the use of costly vehicle sensors. In (Xu et al., 2019), a novel robust fault detection approach is proposed. Besides, an unknown input observer is designed for LPV systems with both state and output scheduled by inexact scheduling variables. Here, the stability conditions for the proposed approaches are established via LMI. In Rotondo et al. (2018), a discrete-time LPV unknown input observer is proposed for the diagnosis of actuator faults and ice accretion in unmanned aerial vehicles. The effectiveness of the proposed approach is validated by simulations illustrating the diagnosis of actuator faults and icing in a small unmanned aerial vehicle. In Li et al. (2019), the authors designed a novel fault detection filter for a class of continuous-time LPV systems. This filter is transformed into an H_∞ filtering problem for the filtering error system with uncertain parameters. In Liu et al. (2019), an LPV model for the aero-engine dynamics is constructed. Next, a theoretical sufficiency criterion is provided to guarantee H_∞ performance based on LMI. The simulations showed the validity of the proposed strategy by reducing the computational cost and avoiding false switching due to disturbances. The authors of (Yang et al., 2020) constructed an LPV model of the proton-exchange-membrane-fuel-cell system to describe its behaviour and to reduce the computation cost. Besides, this LPV model is used to propose an augmented state observer for simultaneously estimating the states and component faults. The robustness is guaranteed against disturbances and measurement noises. In Alcalá et al. (2020), to develop a Model Predictive Controller that can be calculated online with reduced computational cost, the authors used the LPV theory to model and to control an autonomous vehicle. On the other hand, the problem of the best trajectory is solved by an optimal offline trajectory planner.

1.3. Challenges and Contributions

In previous work (Hasseni and Abdou, 2017), the translational DOF has been eliminated by taking a reduced model; the model was presented by two states $(\theta, \dot{\theta})$, the objective was to stabilize the pendulum in null angle with robustness against disturbances and uncertainties. In this work, the novelty is presented within these three points; include the friction effect and consider the velocity as a state (a), getting optimal weighting functions (b) and both of the two DOF $(\theta$ and $x)$ is stabilized and controlled simultaneously (c).

- a) Unlike Hasseni and Abdou (2017), in this work, we manipulate with considering the friction effect, so, the translational velocity has been included as a state. We note that we don't consider the translational position (x) as a state because it isn't necessary to measure or estimate the position of the pendulum's cart (i.e., Segway), where the objective is to stabilize it because the rider can move it by inclining himself.
- b) The technique of the controller design (LFT-based LPV H_∞) is applied here. One of the problems we face on the design is the weighting functions' selection, which depends on experimental skills. Many researchers have been interested in this

issue (Zhou and Doyle, 1998; Beaven et al., 1996; Hu et al., 2000), but there is no general methodology to select the weighting functions. This problem appears on complex systems when the performance specification is not (or is difficult to) defined. When we impose such optimal desired performance presented by the weighting functions, the H_∞ controller design process maybe failed to find a suitable controller for such performance, the solution is that we have to demean the performance specification. Nature-inspired stochastic optimization tools have been used in many works to get the weighting functions' optimal parameters with the existing H_∞ controller, for the LTI system (Alfaro-Cid et al., 2008), for a polytopic-LPV system (Do et al., 2011; Vu et al., 2017), and for an LFT-LPV system (Hasseni and Abdou, 2020). These tools are more required in the multi-objective problem, which is very common in the controller designing process. To get the weighting functions' optimal parameters, we use in this paper two evolutionary algorithms; first, the Genetic Algorithm (GA), which is based on Darwinian evolution, and is created by Holland (Holland, 1992). Second, the Evolutionary Strategies (ES), the first evolutionary algorithm created by Rechenberg (1973), which is based on biological evolution.

- c) With 2DOF $(x$ and $\theta)$ and just one input (Force), the inverted pendulum is considered as an Underactuated Mechanical System (UMS). Based on previous works (Hasseni and Abdou, 2017; Choukchou-Braham et al., 2014a), we conclude that the inverted pendulum is a kind of system that could not be transformed to chain structured and be controlled in cascade strategy. Therefore, in this paper, the global stabilization of the vehicle is investigated under this constraint. We design a controller that stabilizes the two DOF $(\theta$ and $x)$ simultaneously.

1.4. The Paper Outline

The outline of the paper is as follows: In Section 2, we introduce the proposed vehicle to control, the inverted pendulum on a cart. Besides, we present its model and develop its equivalent LFT-LPV representation. In Section 3, we will show the selected evolutionary algorithms, GA and ES, and the characteristics of such techniques we use. In Section 4, after getting the closed-loop system, including the disturbance, the measurement noise, and the weighting functions, we will apply the optimization process to get the weighting functions' optimal parameters considering the angle as the only output. The underactuated degree of freedom is taken into account in Section 5, we will show the ultimate simulation results of stabilizing the system. Finally, our conclusion is presented in Section 6.

2. THE INVERTED PENDULUM ON A CART

2.1. The mathematic model of the inverted pendulum on a cart

A dynamic model of any mechanical system can be derived from Lagrange-Euler formulation. We can describe the dynamic model of the mechanical system as follows:

$$M(q)\ddot{q} + C(q, \dot{q})\dot{q} + G(q) = u \quad (1)$$

where q is the degree of freedom coordinate. \dot{q} and \ddot{q} are its first and second derivatives. $M(q)$ is the symmetric definite positive inertia matrix. The term $C(q, \dot{q})$ is the centrifugal and Coriolis matrix. The term $G(q)$ is the gravitational torques vector, and u is the inputs.

The model of the inverted pendulum on a cart is a benchmark for many autonomous vehicles, that is, Segway (Younis and Abdelati, 2009), which is a vehicle having two degrees of freedom; one is relating on the angular coordinate (θ) and the other is relating on the translational coordinate (x), but the only applied input is the linear thrust force (F). The control objective is to stabilize the pendulum in the null angle whatever the initial angle (Fig. 1).

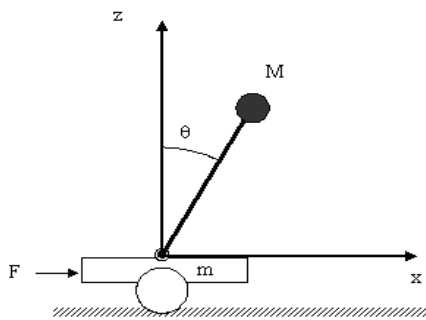


Fig. 1. Geometric scheme of an inverted pendulum on a cart

The dynamic model of the considered system, the inverted pendulum on a cart, is presented in the next expression (Fiacchini et al., 2006; Raffo et al., 2007):

$$\begin{bmatrix} M+m & Ml \cos(\theta) \\ Ml \cos(\theta) & Ml^2 \end{bmatrix} \begin{bmatrix} \ddot{x} \\ \ddot{\theta} \end{bmatrix} + \begin{bmatrix} b & -Ml \sin(\theta)\dot{\theta} \\ 0 & 0 \end{bmatrix} \begin{bmatrix} \dot{x} \\ \dot{\theta} \end{bmatrix} + \begin{bmatrix} 0 \\ -Mgl \sin \theta \end{bmatrix} = \begin{bmatrix} F \\ 0 \end{bmatrix} \quad (2)$$

Where m is the mass of the cart. M is the pendulum mass that presents here the mass of the rider who guides the vehicle, l is the pendulum length, g is the gravity constant, b is the linear friction force coefficient, and F is the linear force applied in the vehicle. The objective of this research is the robust control of this nonlinear system by using the LPV technique. We will create the nonlinear model of the inverted pendulum (2) as an LPV with LFT representation in the next subsection.

2.2. The LFT-LPV representation of the inverted pendulum on a cart

As we have mentioned, there are different presentations of an LPV system; polytopic, gridding, and LFT. We use the last one to present the inverted pendulum model because we are getting a single scheduled controller. We have to notice that the controller has the same representation of the system.

We extract the two equations from (2):

$$\begin{cases} (M+m)\ddot{x} + Ml \cos(\theta)\ddot{\theta} + b\dot{x} - Ml \sin(\theta)\dot{\theta}^2 = F \\ Ml \cos(\theta)\ddot{x} + Ml^2\ddot{\theta} - Mgl \sin(\theta) = 0 \end{cases} \quad (3)$$

We face the issue that the term $(Ml \sin(\theta)\dot{\theta}^2)$ makes the applying of the LFT-LPV technique difficult. To avoid this problem,

we change the generated signal by the controller. The new dynamic model is:

$$\begin{cases} (M+m)\ddot{x} + Ml \cos(\theta)\ddot{\theta} + b\dot{x} = u \\ Ml \cos(\theta)\ddot{x} + Ml^2\ddot{\theta} - Mgl \sin(\theta) = 0 \end{cases} \quad (4)$$

In which:

$$u = F + Ml \sin(\theta)\dot{\theta}^2 \quad (5)$$

By replacing one equation of (4) with the other, we take the nonlinearities as varying parameters. After some mathematical operations, we extract the LFT-LPV state space (6) and its structure (Fig. 2):

$$\begin{bmatrix} \dot{x} \\ z_\rho \\ y \end{bmatrix} = \begin{bmatrix} \mathcal{A} & \mathcal{B}_\rho & \mathcal{B}_1 \\ \mathcal{C}_\rho & \mathcal{D}_{\rho\rho} & \mathcal{D}_{\rho 1} \\ \mathcal{C}_1 & \mathcal{D}_{1\rho} & \mathcal{D}_{11} \end{bmatrix} \cdot \begin{bmatrix} x \\ w_\rho \\ u \end{bmatrix} \quad (6)$$

$$w_\rho = \theta z_\rho$$

where x is the states' vector, $x = [\theta \ \dot{\theta} \ \dot{x}]^T$. u is the input. z_ρ and w_ρ are the inputs and outputs of the parameters block Θ .

The matrices:

$$\mathcal{A} = \begin{bmatrix} 0 & 1 & 0 \\ \frac{g}{l} & 0 & \frac{b}{(M+m)l} \\ 0 & 0 & \frac{-b}{(M+m)} \end{bmatrix}, \mathcal{B}_\rho = \begin{bmatrix} 0 & 0 & 0 \\ \frac{g}{l} & 1 & 0 \\ 0 & 0 & \frac{Ml}{(M+m)} \end{bmatrix}, \mathcal{B}_1 = \begin{bmatrix} 0 \\ \frac{-1}{(M+m)} \\ 1 \\ \frac{1}{(M+m)} \end{bmatrix}, \mathcal{C}_\rho = \begin{bmatrix} 1 & 0 & 0 \\ 0 & 0 & b \\ \frac{g}{l} & 0 & \frac{b}{(M+m)l} \end{bmatrix}, \mathcal{C}_1 = [1 \ 0 \ 0],$$

$$\mathcal{D}_{\rho\rho} = \begin{bmatrix} 0 & 0 & 0 \\ 0 & 0 & 0 \\ \frac{g}{l} & 1 & 0 \\ 0 & 0 & 1 \end{bmatrix}, \mathcal{D}_{\rho 1} = \begin{bmatrix} 0 \\ -1 \\ -1 \\ \frac{1}{(M+m)} \end{bmatrix},$$

$$\mathcal{D}_{1\rho} = [0 \ 0 \ 0 \ 0], \mathcal{D}_{11} = 0, \theta = \begin{bmatrix} \rho_1 & 0 & 0 & 0 \\ 0 & \rho_2 & 0 & 0 \\ 0 & 0 & \rho_3 & 0 \\ 0 & 0 & 0 & \rho_4 \end{bmatrix}$$

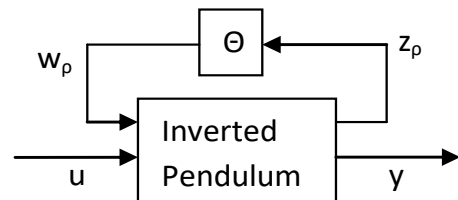


Fig. 2. LFT-LPV scheme of the inverted pendulum

Before designing a controller to stabilize such an LPV system, we need to provide the limit bound of each parameter. All the parameters; $\rho_1 \dots \rho_4$ are dependent on θ .

Theoretically, $-90^\circ \leq \theta \leq 90^\circ$ but to avoid the non-controllability, we have to reduce the bound to $-80^\circ \leq \theta \leq 80^\circ$. Table 1 presents the range of each parameter.

Tab. 1. The ranges of the varying parameters

Parameter	Description	Min. value	Max. value
ρ_1	$\left(\frac{\sin \theta}{\theta}\right) - 1$	-0.3	0
ρ_2	$\cos \theta - 1$	-0.83	0
ρ_3	$\cos \theta$	0.17	1
ρ_4	$\cos^2 \theta$	0.03	1

We notice that in (6)–(7), we didn't generate the closed-loop system yet, just convert the plant (4) to LFT-LPV representation. We need to interconnect the plant with the disturbances and the weighting functions. Our contribution is to select the weighting functions parameters by the nature-inspired algorithms (GA and ES). So, in the next section, we introduce the algorithms that we developed and their characteristics.

3. NATURE-INSPIRED ALGORITHMS

The nature-inspired optimization algorithms have common tasks on their procedures: selection randomly of initial solutions, evaluate the solutions depending on a fitness function, elimination of the worst solutions, and generation of new solutions. This last one is carried out by a set of operations (crossover, mutation, and selection). The significant difference between such algorithms is the generation of new solutions.

In the next subsections, we will show a description of the used algorithms (GA, ES), and their properties are explained by their pseudo-codes.

3.1. Genetic Algorithm

Genetic Algorithm (GA) is one of the oldest evolutionary algorithms. It is the most popular EAs in engineering applications. It was developed and created by Holland (1992). It is based on the Darwinian evolution of biological systems. Its operators are the biological operators: crossover, mutation, and selection, which are applied to each population. The population is divided on individuals, where the best individuals have a chance to survive and transfer their characteristics to the next generation. The individual is called chromosome, which presents a solution. In our work, we consider the individual as a real-coded solution (Wright, 1991) presented by a vector and the generation is the iteration to generate a new set of solutions. The procedure is as illustrated in

Algorithm 1:

Algorithm 1 : Genetic Algorithm

Initialize a solutions randomly;

While max_Generation not meet **do**

 Evaluate each solution;

 Rank the solutions;

 Recombine_BMW pairs of parents;

 Mutate the offspring by p_m ;

 Replace the worst parents by best offspring;

end while

The operation *Evaluate* is the evaluation according to its fitness function, where we need to rank the population according to its fitness to perform the Best-Mate-Worst crossover (Abdou and Soltani, 2005; Yeo and Lu, 1999). All the population's individuals are passing on the crossover operation (*Recombine_BMW*), which is presented by the following expression:

$$\begin{cases} x_i^{t+1} = \alpha \cdot x_i^t + (1 - \alpha) \cdot x_j^t \\ x_j^{t+1} = \alpha \cdot x_j^t + (1 - \alpha) \cdot x_i^t \end{cases} \quad (8)$$

The operation *Mutate* is a random mutation that is implemented on a few of the offspring (probability of p_m) after the crossover operation. The Gaussian mutation is used as:

$$x_i^{t+1} = x_i^{t+1} + N(0, \sigma) \quad (9)$$

Finally, the operator of the selection (*Replace*) permits to replace the worst individuals of the previous generation by the best individuals of the new generation to keep the size of the population and pass to the next generation. The parameters are shown in Table 2.

3.2. Evolutionary Strategies

Evolutionary Strategies (ES) is the oldest evolutionary algorithm. It is based on biological evolution. Like the GA, the ES operators are crossover (combination), mutation, and selection (Hansen et al., 2015). Its main advantage is the self-adaptive control of parameters, especially in the mutation task. ES contains many strategies; we use here the $(\mu+\lambda)$ strategy (Abdou and Soltani, 2008) with real-coding individuals. In the selection task, we took λ individuals from the offspring's population gathered with the best μ individuals from the parent's population, and we consider the result as a new generation. Unlike the GA, in the combination (crossover), we don't need to rank the population because the combination is randomly achieved between individuals (a fraction λ). The procedure is illustrated in Algorithm 2:

Algorithm 2 : Evolution Strategies

Initialize solutions randomly;

While max_Generation not meet **do**

 Generate new solutions;

 Recombine pairs of parents;

 Mutate the offspring;

 Rank the solutions;

 Replace new generation $(\mu+\lambda)$;

end while

The crossover task (*Recombine*) is implemented as in the case of the GA (8) by selecting λ parents randomly with a real-coding of the individuals (Wright, 1991). The main characteristic of ES is the self-adaptation mutation. So, we propose to use a *log-normal auto-adaptive* mutation in *Mutate* task as:

$$\sigma^{t+1} = \sigma^t \cdot e^{(\sqrt{n})^{-1} \cdot N(0,1)} \quad (10)$$

$$x_i^{t+1} = x_i^{t+1} + N(0, \sigma^{t+1}) \quad (11)$$

In the last operation (*Replace*), we take λ individuals of the offspring population and the best μ ones of parents' population to transfer them to the next generation. The common parameters are *max_Generation*, which is equal to 20 and *population size* is equal to 50. The other parameters are shown in Table 2.

Tab. 2. Parameters setting of different algorithms

GA		ES	
Par.	Val.	Par.	Val.
<i>cross.</i>	BMW	ρ_m	0.3
ρ_m	0.04	λ	36
α	1/3	μ	14
σ	0.04	σ^0	0.3

4. CONTROLLER DESIGN AND IMPLEMENTATION

In this section, the only output we consider is the angle (θ), where the objective is to make the pendulum's orientation null without considering the translational DOF.

4.1. The closed loop generation

Before passing to the controller's design phase, we are going to generate the closed-loop system (plant-controller) including the external signals and weighting functions. We notice that the controller has the same structure as the plant (Fig. 3).

The LFT-LPV state space of the augmented plant is as follows:

$$\begin{aligned}
 \dot{x} &= A x + B_\rho w_\rho + B_1 w + B_2 u \\
 z_\rho &= C_\rho x + D_{\rho\rho} w_\rho + D_{\rho 1} w + D_{\rho 2} u \\
 z &= C_1 x + D_{1\rho} w_\rho + D_{11} w + D_{12} u \\
 y &= C_2 x + D_{2\rho} w_\rho + D_{21} w + D_{22} u \\
 w_\rho &= \Theta z_\rho
 \end{aligned} \tag{12}$$

where $x \in \mathbb{R}^n$ is the state vector. $u \in \mathbb{R}^{n_u}$ is the control inputs vector. $y \in \mathbb{R}^{n_y}$ is the measurement outputs vector. $z \in \mathbb{R}^{n_z}$ is the controlled outputs. $w \in \mathbb{R}^{n_w}$ is the exogenous inputs (i.e., disturbances). z_p and $w_p \in \mathbb{R}^r$ are the inputs and outputs of parameter block Θ , with: $\Theta = \text{diag}(\rho_1 I_{r_1}, \rho_2 I_{r_2} \dots \rho_k I_{r_k})$.

The controller $K(\rho)$ is also an LPV system with LFT representation. We present its state space as follows:

$$\begin{aligned}
 \dot{x}_K &= A_K x_K + B_{K1} y + B_{K\rho} w_{K\rho} \\
 u &= C_{K1} x_K + D_{K11} y + D_{K1\rho} w_{K\rho} \\
 z_{K\rho} &= C_{K\rho} x_K + D_{K\rho 1} y + D_{K\rho\rho} w_{K\rho} \\
 w_{K\rho} &= \Theta z_{K\rho}
 \end{aligned} \tag{13}$$

where $x_K \in \mathbb{R}^n$ is the controller states vector. $y \in \mathbb{R}^{n_y}$ is the measurement outputs from the plant. $u \in \mathbb{R}^{n_u}$ is the controller outputs. $z_{K\rho}$ and $w_{K\rho} \in \mathbb{R}^r$ are the inputs and the outputs of the parameter block.

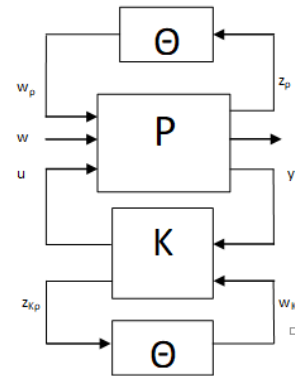


Fig. 3. LFT-LPV closed loop structure $F = u - Ml \sin(\theta)\dot{\theta}^2$

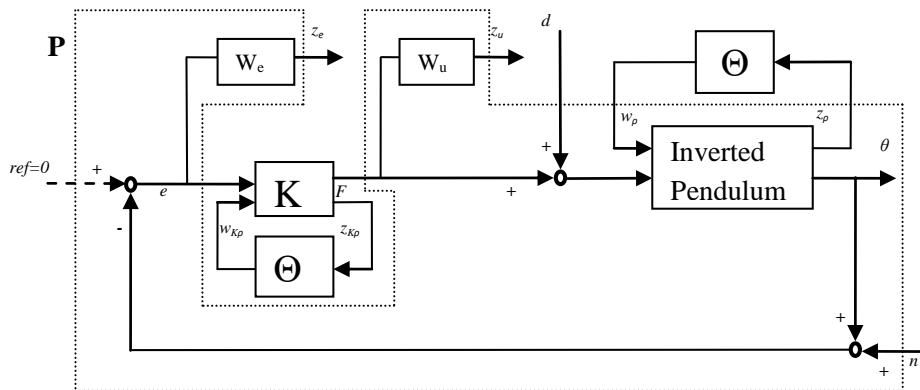


Fig. 4. Closed loop plant-controller interconnection

We interconnect the inverted pendulum system (6)–(7) with the exogenous inputs (disturbance on the input, and measurement noise on the output). We notice in (7) that the output matrix ($C_1 = [1 \ 0 \ 0]$) because we considered the angle θ as the only output.

As a last step of the designing the closed-loop scheme, we provide the applied force (F) from the generated input (u), from (5):

$$F = u - Ml \sin(\theta) \dot{\theta}^2 \tag{14}$$

The closed-loop scheme is presented in Fig. 4, in which there are two exogenous inputs (d: disturbance, n: noise), the measurement output is the error, and the only input is the force F. We have two controlled outputs (ze and zu), which present the performance. Because we have four varying parameters (Tab. 1) $z_p, w_p, z_{Kp},$ and $w_{Kp} \in R^4$.

As we noticed previously, to design the controller, we have to introduce the weighting functions' parameters. Our contribution is based on the choice of the weighting functions' parameters by two evolutionary algorithms (GA and ES) to get the optimal desired performance, and as a consequence, a robust scheduled controller that guarantees this performance. In the next subsection, we show the optimization procedure.

4.2. The optimization procedure

The optimization tools, GA and ES, need to specify some characteristics. The weighting functions formula has been taken as a first-order filter. The performance criterion is presented by W_e and W_u (Fig. 4).

$$W_e = k_e \frac{\tau_{e1}s+1}{\tau_{e2}s+1} \quad (15)$$

$$W_u = k_u \frac{\tau_{u1}s+1}{\tau_{u2}s+1} \quad (16)$$

Therefore, each solution contains six parameters:

$$sol. = [k_e \tau_{e1} \tau_{e2} k_u \tau_{u1} \tau_{u2}] \quad (17)$$

The main effect of the optimization by the evolutionary algorithms is the multi-objective. We have taken two dynamical indices; settling time $ST(\theta(t))$, and the overshoot $OV(\theta(t))$. By experience, the system (inverted pendulum on a cart) needs big force to stabilize in a short time, it could be faced with a big overshoot and oscillations (Fiacchini et al., 2006; Raffo et al., 2007; Hasseni and Abdou, 2017). So, it makes sense to give a small weight to the settling time and a big weight to the overshoot. We have chosen the fitness as follows:

$$Fitness = 0.3 ST(\theta(t)) + 0.7 OV(\theta(t)) \quad (18)$$

The controller synthesis algorithm is achieved by the small gain theorem via LMI conditions. This approach is developed in (Packard, 1994; Apkarian and Gahinet, 1995) and we have been helped by the toolbox *LPVTools* (Hjartarson et al., 2015).

As we noticed, the optimization problem has been achieved by two algorithms (GA and ES). *Algorithm 3* presents the optimization algorithm. We note *Algorithm_i* to mean *Algorithm 1* and *Algorithm 2* because we use both of them to solve the same problem. The details of their procedures and characteristics are mentioned in Section 3 and Table 2.

Algorithm 3 : Optimal weighting functions

Initialize a solutions (17) randomly;

While max_Generation not meet **do**

 Generate the closed loop (Fig. 4);

 Design the own controller;

 Evaluate the solutions based on fitness (18)

 Replace the solutions based on *Algorithm_i*;

end while

The optimal parameters that are obtained by GA and ES are presented in Table 3. Thanks to the optimization algorithms we

guarantee the low pass filter of the control on both algorithms because the H_∞ controller guarantees this condition $\left| \frac{K}{1+KP} \right| \leq \left| \frac{1}{W_u} \right|$ where K is the controller and P is the plant (Zhou and Doyle, 1998).

Tab. 3. Weighting functions parameters

Parameter	k_e	τ_{e1}	τ_{e2}	k_u	τ_{u1}	τ_{u2}
LPV-GA	3.286	0.4015	6.603	0.673	6.362	0.242
LPV-ES	6.165	7.493	2.772	1.091	5.968	0.645
(Hasseni and Abdou, 2017)	5	0.04	1	1	1	0.1

By taking the guidelines of Skogestad and Postlethwaite (2003) about the filters' shaping, we can find that the obtained controller with GA (LPV-GA) is suitable with these guidelines. The inverse of sensitivity function ($1/W_e$) is a high pass filter with a small gain in low frequencies and a big gain in high frequencies. The desired $\left| \frac{K}{1+KP} \right| = (1/W_u)$, should be a low-frequency function with the maximum gain in low frequencies, while the high-frequency gain is limited by the controller bandwidth. The equations (19)–(20) present the standard forms weights W_e and W_u of the LPV-GA controller, presented in Table 3.

$$W_e = \frac{1/M_s s + \omega_b}{s + \varepsilon \omega_b} = \frac{1/5.05 s + 0.4977}{s + (0.3042 * 0.4977)} \quad (19)$$

$$W_u = \frac{s + \omega_{bc}/M_u}{\varepsilon_u s + \omega_{bc}} = \frac{s + 0.233/1.485}{0.0565 s + 0.233} \quad (20)$$

Fig. 5 presents the bode magnitude of the inverse filters (19)–(20). The inverse of the sensitivity function ($1/W_e$) is a high pass filter, the steady-state error to step input ($\varepsilon = 0.304$), the overshoot magnitude (peak sensitivity, $M_s = 5.05$), and limit closed-loop bandwidth ($\omega_b = 0.4977$ rad/s). The maximum gain of ($1/W_u$) is fairly large ($M_u = 1.485$), it is limited by the controller bandwidth ($\omega_{bc} = 0.233$ rad/s). To make W_u proper, we introduce a faraway pole, as an obtained result, ε_1 is very small ($\varepsilon_1 = 0.0565$).

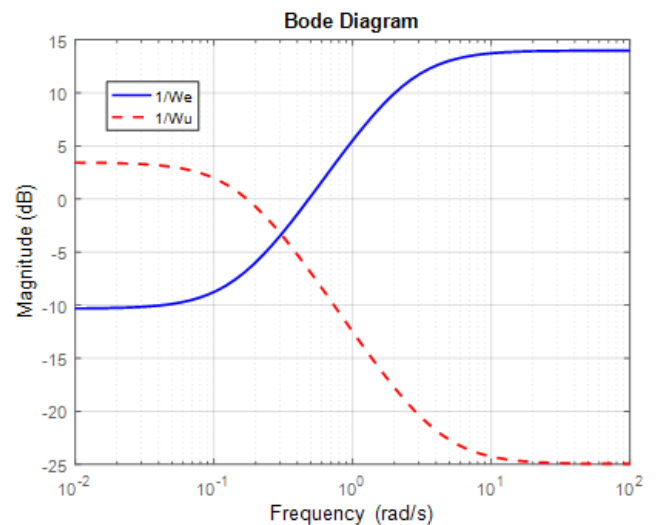


Fig. 5. Performance weight (solid) and control weight (dashed) of LPV-GA

4.3. Simulation results

This table presents the nominal values of the inverted pendulum on the cart used in this paper.

Tab. 4. Nominal parameters of the vehicle

Parameter	Description	Value	Unit
m	Cart's mass	35	Kg
M	Pendulum's mass	70	Kg
l	Pendulum's arm length	1	m
g	Gravity constant	9.8	$m.s^{-2}$
b	Friction coefficient	40	$N.s.m^{-1}$

We have gotten an LFT-LPV H_∞ controller with weighting functions' selection by GA optimization and another by ES. Fig. 6 presents a comparison of the dynamic response and the input between the three LFT-based LPV controllers; the obtained controller with GA (LPV-GA), the obtained one with ES (LPV-ES), and the existing one (Hasseni and Abdou, 2017) (LFT-LPV). Besides, we also show the gridding LPV technique and polytopic LPV technique (Briat, 2015). In this simulation, the performances of each method are presented in Fig. 6 and Table 5, where the initial angle is 60° . Among these controllers, the best performance is obtained by the LPV-GA algorithm.

Tab. 5. Performances comparison between different LPV techniques

Technique	Reference	Overshoot (%)	Settling time (s)
Polytopic-LPV	(Robert et al., 2010)	18	3
Gridding-LPV	(Hjartarson et al., 2015)	17	6.45
LFT-LPV	(Hasseni and Abdou, 2017)	7.2	1.47
LPV-ES	This work	10.7	0.6
LPV-GA	This work	7.6	0.53

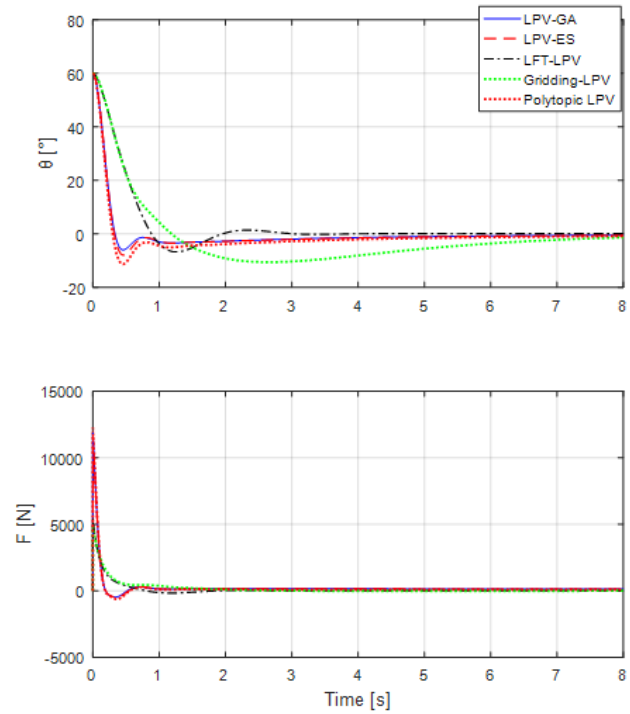


Fig. 6. Dynamic response comparison between different LPV techniques

To demonstrate that the proposed LPV method indeed increases the region of stability, Fig. 7 presents a test of different initial angles with two controllers; the existing controller called (LFT-LPV) and the optimal one gotten by GA called (LPV-GA). It must be shown that the existing controller (dashed line) could not exceed 75° as initial angle. With a bigger initial angle than 75° , the system is completely unstable. On the other hand, with the proposed method (solid line), the system is stable till 86° as an initial angle.

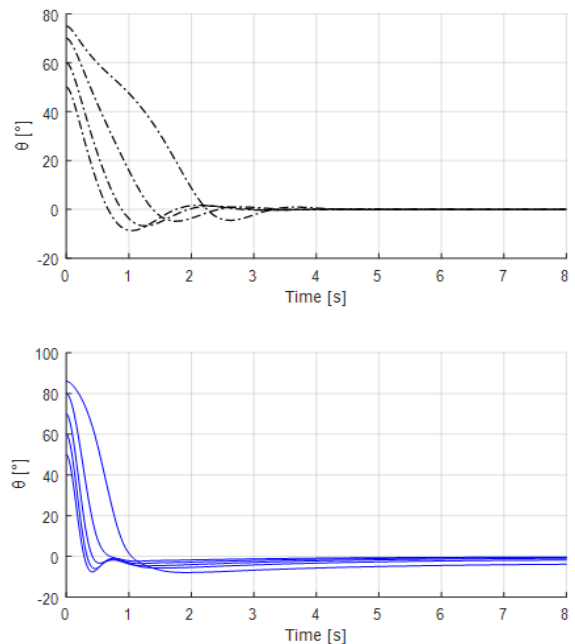


Fig. 7. The angle responses with different initial angles, LPV-GA (solid) and LFT-LPV (dashed)

Now we pass to another point, the robustness to the exogenous inputs. The external inputs we choose are the input disturbance and the noise. As shown in Fig. 8, we apply a permanent noise between $\pm 2^\circ$. Starting from 5 s, we apply a disturbance force of 200 N as shown in Fig. 8.

Remark 1: In the simulation, we don't apply the robust LPV controller on the approximated LPV model (6)–(7), but on the original nonlinear model itself (3).

Fig. 9 presents a comparison of the angle response (θ), the linear velocity (V), and the input (F) between LPV-GA and LPV-ES with the presence of disturbance and noises. In the curve of (θ), we notice that there is robustness to the noises. We notice also that there is a variation in 5 s due to the suddenly applied force, but the disturbance is ultimately rejected.

We conclude that the nature-inspired optimization tools, GA and ES, helped us to choose the suitable weighting functions parameters to get good performance. Also, the scheduled LFT-LPV controller guarantees the robustness against the external signals. But, the linear velocity (V) has not reached the null at the same time with the angle (the vehicle has not stopped) because we didn't care for the velocity in the controller design. The system is considered as a Single-Input Single-Output system (SISO). This is what we are discussing in the next section.

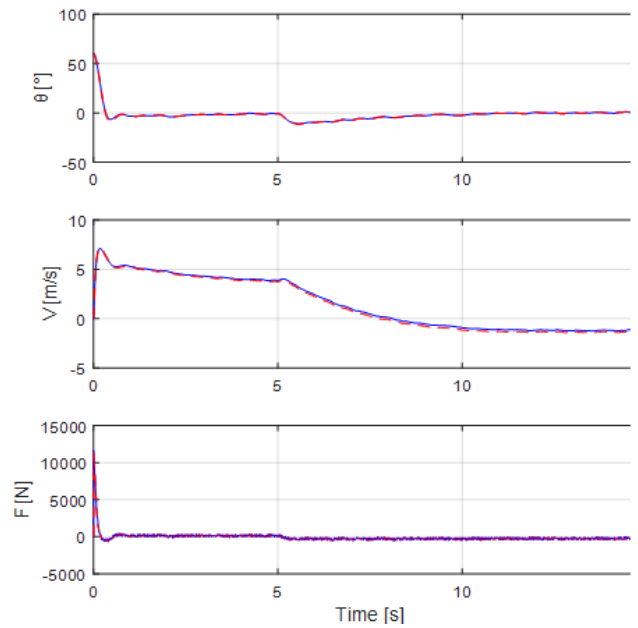


Fig. 9. The angle (θ), the velocity (V) and the force (F) responses with presence of disturbance and noise

5. EXTENDED LPV STABILIZATION TO THE 2DOF

An underactuated mechanical system (UMS) is a system that has fewer control inputs than the degrees of freedom, as well as the inverted pendulum. It has two degrees of freedom; one is relating to translational coordinate (x), and the other is relating to rotational coordinate (θ), but just one control input, the force (F). In Section 4, the inverted pendulum has been stabilized by a robust LPV H_∞ controller by considering it as a SISO system. In the previous simulation (Section 4), the velocity has reached the null very slowly (300 seconds).

We have to impose the constraint of the underactuated characteristic into account. One may say that alternatively to consider the angle (θ) as the only output, we consider two outputs: the angle (θ) and the linear velocity (\dot{x}) and generate its suitable LPV controller.

We have tried to control the inverted pendulum as a general Single-Input Multi-Outputs system (SIMO) by changing the output matrix of (6) by ($C_1 = \begin{bmatrix} 1 & 0 & 0 \\ 0 & 0 & 1 \end{bmatrix}$). The response, either the angle or the velocity is oscillation and never stabilize (Fig. 10). In this test, the weighting functions are obtained by GA.

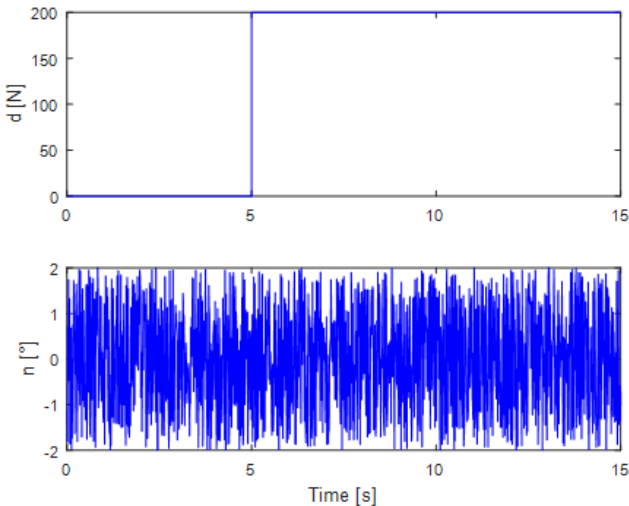


Fig. 8. The disturbance and the noise

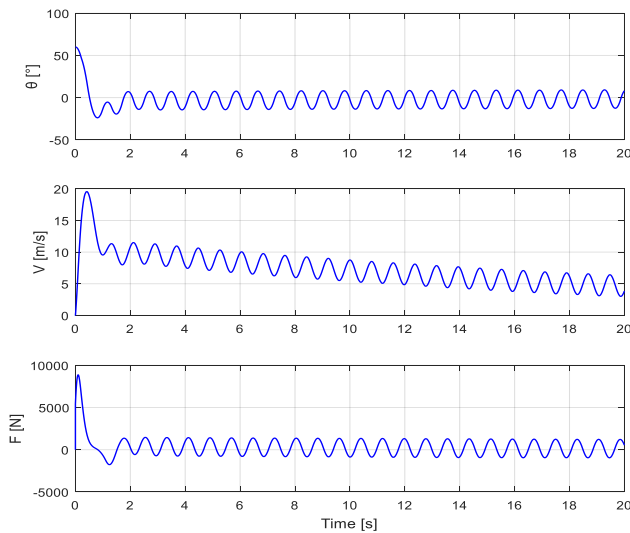


Fig. 10. The dynamic response of the inverted pendulum as a SIMO system

In literature, there is no unique methodology to control a UMS. There are different classifications. One of the most common classifications is *Seto and Baillieul's*. It depends on the so-called Control Flow Diagram (CFD). According to this classification, a UMS could have a chain structure, tree structure, or isolated-vertex structure (Seto and Baillieul, 1994; Choukchou-Braham et al., 2014a). The inverted pendulum is found under the tree class.

There are sub-classes into the tree structure (A1, A2) (Choukchou-Braham et al., 2014a). Since the first (A1) could be converted to a chain class by changing the states and controlled as a chain structure by Backstepping (Rudra et al., 2017). The other subclass (A2) could not. In (Choukchou-Braham et al., 2014b), the authors have proposed a method where the configuration variables (the degrees of freedom) of the system were controlled simultaneously and this is what we are going to develop. We have to include a term related to stabilize the angle (θ) and another term related to stabilize the linear velocity (\dot{x}) in the control law. We will denote to the state \dot{x} by v .

The only expression that has information about (θ) is the error (the measurement output of the LPV plant, Fig. 4). The closed-loop system has been changed by adding a proportional term related to (v), $k_v v$ (Fig. 11). The gain k_v presents the weight of the velocity, and we choose $k_v = 0.02$. The new output is ($\theta + 0.02 v$).

Remark 2: In this stage, we didn't design another controller, but we kept the controller we have designed in Section 4.

We pass now to the simulation phase. Fig. 12 presents the dynamic response of the angle (θ), the velocity (V), and the force (F) of both controllers (LPV-GA and LPV-ES) with the presence of disturbance and noise as well as presented in Fig. 8. In addition to the angle, the velocity is controlled and it has reached zero on both curves (LPV-GA and LPV-ES). The overshoot exceeds (-20°), and that is what the pendulum needs to balance itself. We note also that the system is robust against the permanent noise and the disturbance.

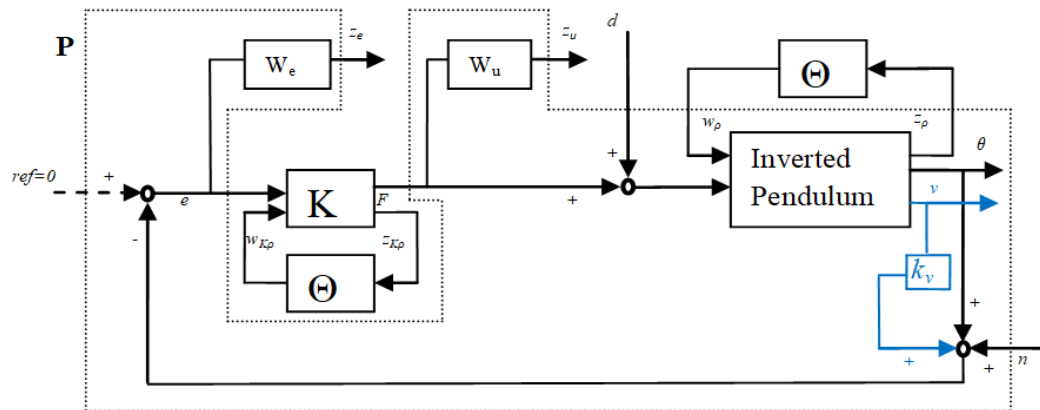


Fig. 11. Underactuated closed loop plant-controller

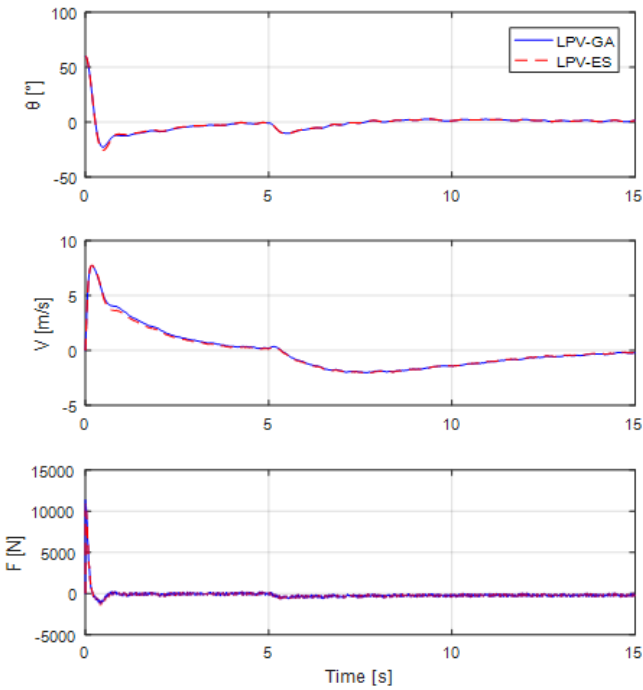


Fig. 12. The angle (θ), the velocity (V) and the force (F) responses with adding the velocity term

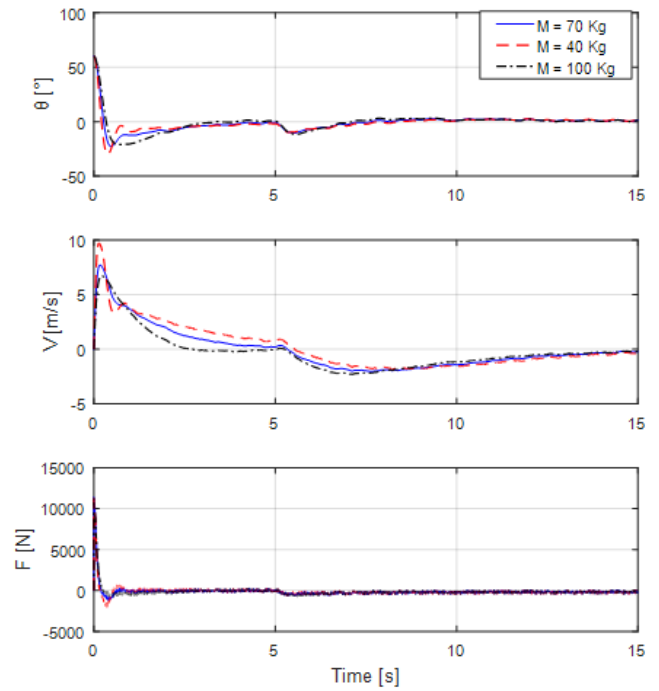


Fig. 13. The angle (θ), the velocity (V) and the force (F) responses with uncertainty on LPV-GA

We have to mention that when the H_∞ controller is achieved, it so guarantees the worst case of uncertainties. That means the closed-loop system is asymptotically stable for any $\|\Delta\|_\infty \leq 1$.

Remark 3: the stability of the augmented system is robust (plant-weighting functions), so, the performance of the system is robust because the performance is presented by the weighting functions.

In our system, the pendulum's mass presents the mass of the rider. We can apply the uncertainty according to the rider's mass by taking 70 Kg as a nominal mass (Tab. 4). In this simulation, we have taken $M = \text{nominal value} \pm 43\%$ (40 Kg, 70 Kg, and 100 Kg). Fig. 13 presents the response with the uncertainty of LPV-GA and Fig. 14 presents the response with the uncertainty of LPV-ES. We note that the controllers are robust to the uncertainty, the angular overshoot is between -20° and -30° , the peak velocity is 8 m/s when ($M = 100$), 9 m/s when ($M = 70$) and 10 m/s when ($M = 40$).

All the previous simulations (Fig. 13 and Fig. 14) are achieved with 60° as an initial angle. In Fig. 15 and Fig. 16, the simulation results of the dynamic responses are achieved with different initial angles (60° , 30° , -30° and -60°). Fig. 15 presents the dynamic responses of LPV-GA and Fig. 16 presents the dynamic responses of LPV-ES. On both controllers, the 2DOF are stabilized. The angle and velocity have reached the equilibrium point simultaneously. Besides, it is robust, whatever the initial angle.

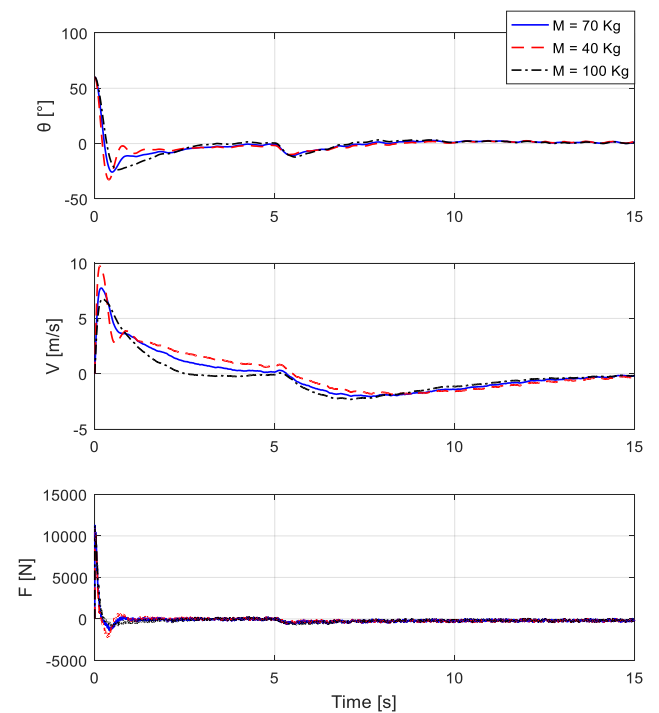


Fig. 14. The angle (θ), the velocity (V) and the force (F) responses with uncertainty on LPV-ES

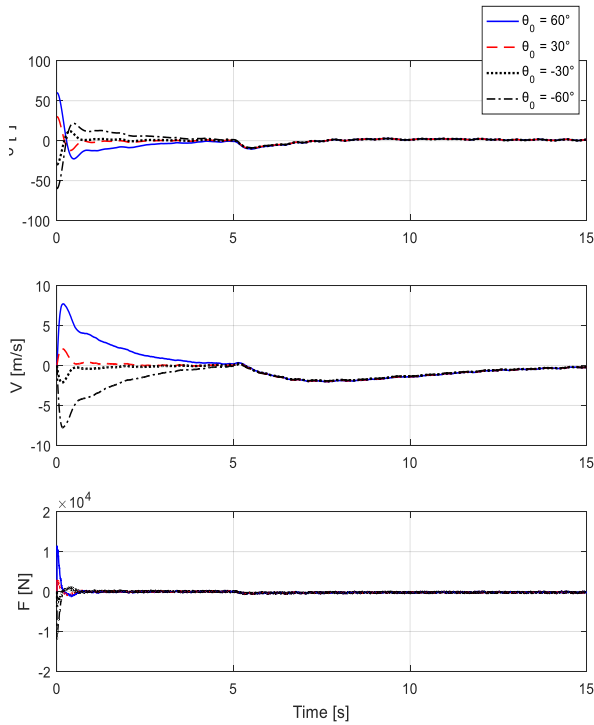


Fig. 15. The angle (θ), the velocity (V) and the force (F) responses with different initial angles on LPV-GA

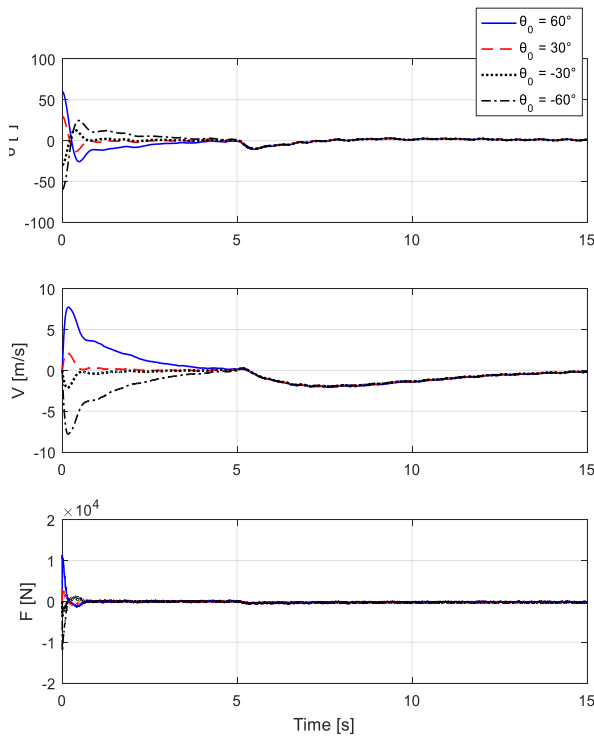


Fig. 16. The angle (θ), the velocity (V) and the force (F) responses with different initial angles on LPV-ES

6. CONCLUSION

In this paper, the robust stabilization problem of the inverted pendulum on a cart is considered. We have applied a scheduled robust controller with type LFT-LPV H_∞ . As a first step, we have

developed its LFT-LPV representation from the nonlinear model. Second, we have focused on the weighting functions' parameters selection. We have suggested solving it through two nature-inspired optimization algorithms (GA and ES). Thanks to those, besides to get optimal performance, the robustness is guaranteed against the disturbances and the uncertainties. The last and important point we have investigated is the problem of underactuation. The inverted pendulum imposes this constraint and our objective is to balance the inverted pendulum where its angle and velocity should be zero without adding another actuator. After we modify the closed-loop structure, the simulation results have shown an optimal performance, the objective is successfully achieved. It is robust against external signals and uncertainties.

REFERENCES

1. Abbas H.S., Tóth R., Petreczky M., Meskin N., and Mohammadpour J. (2014), Embedding of nonlinear systems in a Linear Parameter-Varying representation, In: *Proc. of IFAC World Congress*, Cape Town, South Africa, 6907–6913.
2. Abdou L., and Soltani F. (2005), OS-CFAR and CMLD threshold optimization with genetic algorithms, In: *Proc. of 3rd International Conference on Systems, Signals & Devices, Vol III Communication and Signal Processing*, Sousse, Tunisia.
3. Abdou L., and Soltani F. (2008), OS-CFAR and CMLD threshold optimization in distributed systems using evolutionary strategies, *Signal, Image and Video Processing*, Vol. 2, No. 2, 155–167.
4. Alcalá E., Puig V., Quevedo J., and Rosolia U. (2020), Autonomous racing using Linear Parameter Varying-Model Predictive Control (LPV-MPC), *Control Engineering Practice*, Vol. 95, 104270.
5. Alfaro-Cid E., McGookin E.W., and Murray-Smith D.J. (2008), Optimisation of the weighting function of an H_∞ controller using genetic algorithms and structured genetic algorithms, *International Journal of Systems Science*, Vol. 39, No. 4, 335–347.
6. Apkarian P., and Gahinet P. (1995), A convex characterization of gain-scheduled H_∞ controller, *IEEE Transactions on Automatic Control*, Vol. 40, No. 7, 853–864.
7. Beaven R.W., Wright M.T., and Seaward D.R. (1996), Weighting function selection in the H_∞ design process, *Control Engineering Practice*, Vol. 4, No. 7, 625–633.
8. Boubaker O. (2013), The inverted pendulum benchmark in nonlinear control theory: A survey, *International Journal of Advanced Robotic Systems*, Vol. 10, No. 5, 233–241.
9. Briat C. (2015), *Linear Parameter-Varying and Time-Delay Systems: Analysis, Observation, Filtering & Control*, Springer-Verlag, Heidelberg.
10. Choukchou-Braham A., Cherki B., Djemai M., and Busawon K. (2014a), Classification of Underactuated Mechanical Systems, In: Choukchou-Braham A., Cherki B., Djemai M., and Busawon K. (eds.), *Analysis and Control of Underactuated Mechanical Systems*, Springer, London, 35–54.
11. Choukchou-Braham A., Cherki B., Djemai M., and Busawon K. (2014b), Control Design Schemes for Underactuated Mechanical Systems, In: Choukchou-Braham A., Cherki B., Djemai M., and Busawon K. (eds.), *Analysis and Control of Underactuated Mechanical Systems*, Springer-Verlag, London, 55–91.
12. Do A.L., Sename O., Dugard L., and Soualmi B. (2011), Multi-objective optimization by genetic algorithms in H_∞ /LPV control of semi-active suspension, In: *Proc. of IFAC World Congress*, Milano, Italy, 7162–7167.
13. El-Bardini M., and El-Nagar A.M. (2014), Interval type-2 fuzzy PID controller for uncertain nonlinear inverted pendulum system, *ISA Transactions*, Vol. 53, 732–743.
14. Fiacchini M., Viguria A., Cano R., Prieto A., Rubio F.R., Aracil J., and Canudas-de-Wit C. (2006), Design and experimentation of a

- personal pendulum vehicle, In: *Proc. of Portuguese Conference on Automatic Control*, Lisbona, Portugal.
15. **Hansen N., Arnold D.V., and Auger A.** (2015), Evolution Strategies, In: Kacprzyk J., and Pedrycz W. (eds.), *Springer Handbook of Computational Intelligence*, Springer, Heidelberg, 871–898.
 16. **Hasseni S., and Abdou L.** (2017), Robust LPV control applied to a personal pendulum vehicle, In: *Proc. of International Conference on Sciences and Techniques of Automatic Control and Computer Engineering*, Monastir, Tunisia, 6–11.
 17. **Hasseni S., and Abdou L.** (2018), Integral backstepping/LFT-LPV H_∞ control for the trajectory tracking of a quadcopter, In: *Proc. of International Conference on Systems and Control*, Valencia, Spain, 348–353.
 18. **Hasseni S., and Abdou L.** (2020), Robust LPV control for attitude stabilization of a quadrotor helicopter under input saturations, *Advances in Technology Innovation*, Vol. 5, No. 2, 98–111.
 19. **Hjartarson A., Seiler P., and Packard A.** (2015), LPV Tools: a toolbox for modeling, analysis and synthesis of parameter varying control systems, *IFAC PapersOnLine*, Vol. 48, No. 26, 136–145.
 20. **Holland J.H.** (1992), *Adaptation in Natural and Artificial Systems*, MIT Press, MA, USA.
 21. **Hu J., Bohn C., and Wu H.R.** (2000), Systematic H_∞ weighting function selection and its application to the real-time control of a vertical take-off aircraft, *Control Engineering Practice*, Vol. 8, No. 3, 241–252.
 22. **Iwasaki T., and Shibata G.** (2001), LPV system analysis via quadratic separator for uncertain implicit system. *IEEE Transactions on Automatic Control*, Vol. 46, No. 10, 1195–1208.
 23. **Li S., Jiang S., and Pan F.** (2019), Event-triggered fault detection for networked LPV systems, *Circuits, Systems, and Signal Processing*, Vol. 38, No. 7, 2992–3019.
 24. **Liu T.J., Du X., Sun X.M., Richter H., and Zhu F.** (2019), Robust tracking control of aero-engine rotor speed based on switched LPV model, *Aerospace Science and Technology*, Vol. 91, 382–390.
 25. **Liu Z., Theilliol D., Gu F., He Y., Yang L., and Han J.** (2017), State feedback controller design for affine parameter-dependent LPV systems, *IFAC PapersOnLine*, Vol. 50, No. 1, 9760–9765.
 26. **López-Estrada F.R., Ponsart J.C., Theilliol D., Zhang Y., and Astorga-Zaragoza C.M.** (2016), LPV model-based tracking control and robust sensor fault diagnosis for a quadrotor UAV, *Journal of Intelligent & Robotic Systems*, Vol. 84, 163–177.
 27. **Nguyen A.T., Chevrel P., and Claveau F.** (2020), LPV static output feedback for constrained direct tilt control of narrow tilting vehicles, *IEEE Transactions on Control Systems Technology*, Vol. 28, No. 2, 661–670.
 28. **Ohhira T., and Shimada A.** (2017), Model predictive control for an Inverted pendulum robot with time-varying, *IFAC PapersOnLine*, Vol. 50, No. 1, 776–781.
 29. **Packard A.** (1994), Gain scheduling via linear fractional transformations, *Systems and Control Letters*, Vol. 22, No. 2, 79–92.
 30. **Park M.S., and Chwa D.** (2009), Swing-up and stabilization control of inverted-pendulum systems via coupled sliding-mode control method, *IEEE Transactions on Industrial Electronics*, Vol. 56, No. 9, 3541–3555.
 31. **Prasad L.B., Tyagi B., and Gupta H.O.** (2014), Optimal control of nonlinear inverted pendulum system using PID controller and LQR: Performance analysis without and with disturbance input, *International Journal of Automation and Computing*, Vol. 11, No. 6, 661–670.
 32. **Raffo G.V., Ortega M.G., and Rubio F.R.** (2007), Nonlinear H_∞ Control Applied to the Personal Pendulum Car, In: *Proc. of European Control Conference*, Kos, Greece, 2065–2070.
 33. **Rechenberg I.** (1973), *Evolutionstrategie: Optimierung Technischer Systeme nach Prinzipien der Biologischen Evolution*, Frommann-Holzboog-Verlag, Stuttgart, Germany.
 34. **Robert D., Sename O., and Simon D.** (2010), An H_∞ LPV design for sampling varying controllers: experimentation with a T-inverted pendulum, *IEEE Transactions on Control Systems Technology*, Vol. 18, No. 3, 741–749.
 35. **Rotondo D., Cristofaro A., Johansen T.A., Nejari F., and Puig V.** (2018), Diagnosis of icing and actuator faults in UAVs using LPV unknown input observers, *Journal of Intelligent & Robotic Systems*, Vol. 91, No. 3–4, 651–665.
 36. **Rudra S., Barai R.K., and Maitra M.** (2017), Block Backstepping Control of the Underactuated Mechanical Systems, In: Rudra S., Barai R.K., and Maitra M. (eds.), *Block Backstepping Design of Non-linear State Feedback Control Law for Underactuated Mechanical Systems*, Springer-Verlag, Singapore, 31–52.
 37. **Salhi S., Aouani N., and Salhi S.** (2015), LPV affine modeling, analysis and simulation of DFIG based wind energy conversion system, In: *Proc. of International Conference on Modelling, Identification and Control*, Sousse, Tunisia.
 38. **Scherer C.W.** (2001), LPV control and full block multipliers, *Automatica*, Vol. 37, No. 3, 361–375.
 39. **Seto D., and Baillieul J.** (1994), Control problem in super-articulated mechanical systems, *IEEE Transactions on Automatic Control*, Vol. 39, No. 14, 2442–2453.
 40. **Shamma J., and Athans M.** (1991), Gain scheduling: potential hazards and possible remedies, In: *Proc. of American Control Conference*, Boston, USA, 516–521.
 41. **Siradjuddin I., Amalia Z., Setiawan B., Ronilaya F., Rohadi E., Setiawan A., Rahmad C., and Adhisuwignjo S.** (2018), Stabilising a cart inverted pendulum with an augmented PID control scheme, *MATEC Web of Conference*, Vol. 197, 11013.
 42. **Skogestad S., and Postlethwaite I.** (2003), *Multivariable Feedback Control, Analysis and Design*, John Wiley & Sons, Chichester.
 43. **Tasoujian S., Salavati S., Franchek M.A., and Grigoriadis K.M.** (2020), Robust delay-dependent LPV synthesis for blood pressure control with real-time Bayesian parameter estimation, *IET Control Theory & Applications*, Vol. 14, No. 10, 1334–1345.
 44. **Vu V.T., Sename O., Dugard L., and Gaspar P.** (2017), Multi objective H_∞ active-roll bar control for heavy vehicles, *IFAC PapersOnLine*, Vol. 50, No. 1, 13802–13807.
 45. **Wright A.** (1991), *Genetic Algorithms for Real Parameter Optimization*, Morgan Kaufmann, San Mateo, California.
 46. **Wu F.** (2001), A generalized LPV system analysis and control synthesis framework, *International Journal of Control*, Vol. 74, No. 9, 745–759.
 47. **Wu F., Yang X., Packard A., and Becker G.** (1996), Induced L_2 norm control for LPV systems with bounded parameter variation rates, *International Journal of Robust and Nonlinear Control*, Vol. 6, No. 9–10, 983–998.
 48. **Xu F., Tan J., Wang Y., Wang X., Liang B., and Yuan B.** (2019), Robust fault detection and set-theoretic UIO for discrete-time LPV systems with state and output equations scheduled by inexact scheduling variables, *IEEE Transactions on Automatic Control*, Vol. 64, No. 12, 4982–4997.
 49. **Yang D., Wang Y., and Chen Z.** (2020), Robust fault diagnosis and fault tolerant control for PEMFC system based on an augmented LPV observer, *International Journal of Hydrogen Energy*, Vol. 45, No. 24, 13508–13522.
 50. **Yeo B.K., and Lu Y.** (1999), Array failure correction with a genetic algorithm, *IEEE Transactions on Antennas and Propagation*, Vol. 47, No. 7, 823–828.
 51. **Younis W., and Abdelati M.** (2009), Design and implementation of an experimental Segway model, *AIP Conference Proceedings*, Vol. 1107, 350–354.
 52. **Zhou K., and Doyle J.C.** (1998), *Essentials of Robust Control*, Prentice Hall, Upper Saddle River, NJ.

IDEAL RECTIFIER BRIDGE CONVERTING THE HARVESTED ENERGY OF VIBRATIONS INTO ELECTRIC ENERGY TO POWER AN MR DAMPER

Bogdan SAPIŃSKI^{*}, Łukasz JASTRZĘBSKI^{}, Arkadiusz KOZIEL^{***}**

^{*}Faculty of Mechanical Engineering and Robotics, Department of Process Control, AGH University of Science and Technology, al. Mickiewicza 30, 30-059 Kraków, Poland

deep@agh.edu.pl, lukasz.jastrzebski83@gmail.com, arkadiuszkoziel93@gmail.com

received 3 November 2020, revised 19 January 2021, accepted 22 January 2021

Abstract: The newly developed ideal rectifier bridge equipped with four N-type MOSFETs and two rail-to-rail operational amplifiers is a part of a typical energy harvesting conditioning circuit responsible for the rectification stage in the system of converting the energy harvested from vibrations into electrical energy to power the MR damper. The only energy loss in the bridge is caused by the voltage loss in transistors' channels. The first sections of the work summarises the structural design of the bridge, the simulation procedure under the RL load and by sine voltage inputs with predetermined frequency and amplitude range, and benchmarks the results against those obtained for the conventional bridge based on Schottky diodes. In the second section, the PCB prototype of the bridge is analysed, and measurement data are compiled. The third section reports on the laboratory testing of the developed bridge converting the harvested energy in an MR damper-based vibration reduction system.

Key words: Energy Harvesting, Rectifier Bridge, Voltage, Current, MR Damper

1. INTRODUCTION

Energy harvesting vibration reduction systems with MR dampers have attracted a great deal of attention recently. Their main advantage is that they are able to effectively reduce the vibration amplitude of the sprung mass at near-resonance frequency using the energy harvested from vibrations. Such systems provided in e.g. automobiles and railway vehicles (Sung and Choi 2008, Wang and Liao 2009a, Wang and Liao 2009b) utilize ambient vibrations to excite the harvester harmonically, thereby producing an alternating voltage or AC power. The AC power has to be conditioned before it can be effectively used with any electronics or storage elements requiring DC power (Safei et al. 2019). A typical energy harvesting conditioning circuit has two major components: the rectification (AC/DC conversion) and regulation stage (DC/DC conversion). The simplest energy harvesting circuit is the full-wave rectifier (converting AC signals into all positive voltage) integrated with a smoothing capacitor (converting the signals to DC).

As demonstrated in Sapiński (2011), the energy harvesting vibration reduction system with an MR damper has three separate components: an electromagnetic harvester, an MR damper and an energy conditioning circuitry. Similar three components can be distinguished in the energy harvesting MR damper reported in Sapiński (2014). It appears that in both cases, the system is able to adjust itself to structural vibrations, however, in the limited range of the harvester output voltages. The constraint imposed by the limited range of the harvester output voltage is the consequence of the predetermined range of MR damper piston velocity (amplitude and frequency of vibrations). Assuming that the har-

vester and MR damper parameters are known beforehand, of particular interest is the AC/DC conversion of the harvester output voltage such that the power loss should be as low as possible.

In their former studies, the authors used the rectifier bridge incorporating of the Graetz bridge based on Schottky diodes. Those diodes are widely used in automotive power systems as protection from the effects of reverse battery conditions and of other automotive electrical transients.

When analysing literature on the subject, the authors' attention has been drawn to original solutions concerning rectifier bridges, which are described in many research reports. For example, Balato et al. (2017) demonstrated an H-bridge Graetz rectifier with a smoothing capacitor to convert AC current generated in resonant electromagnetic vibration harvester into DC current supplying resistance load. Snamina and Orkisz (2014) proposed an H-bridge Graetz rectifier, enabling the accumulation of energy recovered from vibrations in 2DOF mechanical system in large-capacity capacitors. Grzybek and Micek (2017) described an H-bridge Graetz that was applied in the mechanical system with a self-powered vibration sensor, including piezoelectric material. It should be noted that the rectifier bridges presented in those works concern silicon diodes. The forward voltage drop of the Schottky diodes, however, results in significant power loss at high currents and enhances the need for thermal management using heatsinks and a larger PCB space. For this reason, the authors undertook to develop a new rectifier bridge to eliminate the aforementioned drawbacks so that it should be applicable in MR damper-based vibration reduction systems and recommended the use of N-type MOSFETs in place of Schottky diodes (Selevaraj 2019).

It is worthwhile to mention the solution by Maiorca et al. (2013) proposed to use of a diode-less mechanical H-bridge rectifier, in which there are no voltage drops in the forward direction. However, this solution is problematic due to the mechanical strength of the rectifier elements and the breakdown that may occur at the time of switching. The solution most similar to the one discussed in this work was proposed by Chytil (2014) where the ideal rectifier bridge was based on a commercial chip that controls four transistors. Also, this solution is not possible to use in the application described in Sapiński (2011) due to the too high voltage (9 V) required for the proper operation of the H-bridge rectifier.

The present paper is organized as follows. Section 2 summarises the design structure and operating principle of the ideal rectifier bridge. Section 3 benchmarks the simulation results of the bridge under the RL load and by sine voltage inputs with predetermined frequency and amplitude range against those obtained for the Graetz bridge based on Schottky diodes. Section 4 describes PCB of the bridge. Section 5 collates the measurement data obtained for the two bridge types and discusses the experimental results in relation to simulation data. Section 6 is focused

on the laboratory testing of the developed ideal bridge employed for converting the energy harvested from vibrations into electric energy used to power the MR damper. Finally, the main conclusions are presented in Section 7.

2. DESIGN STRUCTURE AND OPERATING PRINCIPLE

The objectives underlying the bridge design are closely associated with parameters of the prototype electromagnetic harvester device (Sapiński 2010) and of the Lord RD-8040-1 MR damper (Lord Corporation 2020) and their application in vibration reduction systems with energy harvesting capability. As shown in Fig. 1, the bridge is positioned between the harvester coil and the control coil of the MR damper. The input to the bridge is a voltage signal induced in the harvester coil (proportional to vibration velocity), the output signal being the rectified voltage, supplying the control coil of the MR damper.

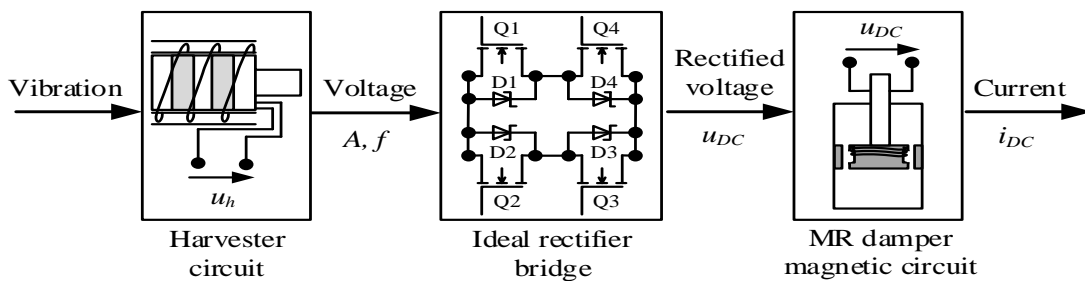


Fig. 1. Schematic diagram of the harvester – ideal rectifier bridge – MR damper system

The underlying assumptions are as follows :

- the maximal amplitude and frequency of voltage induced in the harvester coil should be $A=10\text{ V}$ and $f=10\text{ Hz}$,
- resistance and inductance of RD-8040-1 damper coil should be $R_d=5\Omega$ and $L_d=100\text{ mH}$,
- the bridge performs with the efficiency approaching 95% as long as the amplitude of voltage generated by the harvester is of the order of more than 10 mV,
- the electric energy required to power the bridge components comes either from the harvester (parasite mode) or from an external local storage device (a Li-ion cell or a battery of capacitors),
- in the conditions of no power supply to the bridge components, the bridge begins to operate as a conventional bridge based on Schottky diodes (with a decidedly lower efficiency).

It is worthwhile to mention that the bridge can be adapted to operate at higher frequency and amplitude of voltage induced in the harvester coil than the levels assumed in the present study.

The diagram of a newly developed bridge (Fig. 2) features three major blocks: the supply block (SB), the control block (CB) and the rectifier block (RB). The BOOST (U1) DC/DC converter in the SB block enhances the input voltage u_{IN} according to the actual position of the jumper JP1 (available positions: 1, 2, 3). In its position 1, converter U1 is supplied with rectified voltage u_{DC} , whilst the bridge operates in the parasite mode $u_{IN} = u_{DC}$.

In position 2, converter U1 is supplied with voltage from an external source u_{EXT} – i.e. the bridge operates in the external supply mode. Converter U1 elevates the voltage u_{IN} to $u_{OUT}=20\text{ V}$ with respect to the GND reference, when $u_{IN} \geq 3\text{ V}$. In position 3, converter U1 is discon-

nected from the power supply – the bridge operates in the passive mode acting as a conventional Graetz-type rectifying bridge based on Schottky diodes D1-D4.

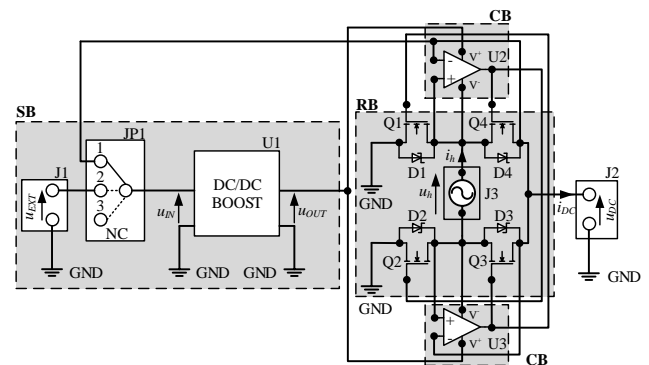


Fig. 2. Schematic diagram of the ideal rectifier bridge

Converter U1 is requisite to ensure the adequate control of transistors Q1-Q4 whose operation in the linear range is undesirable. Sources of transistors Q3 and Q4 are connected to points of various potential, the potential difference yielding voltage u_h (Fig. 2). Consequently, voltage u_{OUT} must be larger than the sum of u_h and the minimal gate-source threshold voltage U_{GSmin} of transistors Q3 and Q4. The block SB is provided with fault and overload protection, as well as u_{EXT} reverse polarity protection and electrostatic discharge protection (ESD).

Block CB incorporates two operational rail-to-rail amplifiers U2 and U3 operated in the differential configuration with the amplification 10,000 [V/V]. Amplifiers U2 and U3 use the complete span between the negative and positive supply rail for signal conditioning at the input and output. Their function is to amplify the drain-source voltage in transistors Q3 and Q4. The duty cycle of the bridge involves two phases: 1 and 2. At the onset of phase 1, transistors Q1-Q4 remain closed (in off-position), whilst voltage u_h produces the current flow through diodes D2 and D4. The potential difference between the drain in transistor Q4 and its source is amplified by op-amp U2. The gate-source voltage U_{GS} of transistors Q2 and Q4 is larger than the voltage required for their full opening ($U_{GS} > U_{GSmin}$), resulting in immediate current flow i_h through transistors Q2 and Q4. Current i_{DC} flows through the two-terminal network R_dL_d and returns to the harvester coil. The only power loss in the ideal bridge circuit is due to a voltage drop on open channel/drain-source on-state resistances in transistors Q2 and Q4. Throughout phase 1, transistors Q1 and Q3 remain closed, whilst their gate potential is equal to that of their sources. Phase 2, in which transistors Q1 and Q3 are operated and controlled via amplifier U3, proceeds in a similar manner as phase 1.

Block RB is comprised of four N-type MOSFETs (the nominal open channel resistance being 5 m Ω) connected in the H-bridge configuration. Schottky diodes D1-D4 connected in parallel with transistors Q1-Q4 enable the passive mode operation (with no power supply).

3. SIMULATION PROCEDURE

Two variants of bridge systems were investigated in the simulation procedure: a conventional rectifier (B1) based on Schottky diodes and an ideal rectifier (B2) incorporating N-type MOSFETs and two rail-to-rail operational amplifiers. The simulation procedure use the LTSpice environment (Analog Devices, 2020). The purpose of the procedure was to determine the extent of power loss in the form of heat released on diodes D1-D4 in bridge B1 and on transistors Q1-Q4 in bridge B2. Key features that have implications for the simulation procedures are as follows:

- the diodes D1-D4 are the type RBR2MM60C (Rohm, 2020), transistors Q1-Q4 are IRFH5007 type (Infineon, 2020);
- the output in each bridge is connected with the control coil of the MR damper modelled as a two-terminal network R_dL_d (resistance-inductance load), without taking into account the processes in the magnetic circuit;
- the harvester coil is an ideal source of sinusoidally varied voltage with amplitude A and frequency f (its resistance and internal inductance being neglected);
- the capacitor smoothing ripples of voltage u_{DC} in the bridge outlet is neglected;
- in the case of bridge B2, the power supply comes from the battery $u_{EXT}=3.7$ V in the SB block.

Simulation results are illustrated in Figs. 3-6. Apparently, the voltage drop ($|u_h| - u_{DC}$) across bridge B1 is about 0.7 V, which is equal to 2x forward voltage drop U_F in diodes D1-D4 for the instantaneous current level i_{DC} (Fig. 3a, b). When $A=2$ V, the maximal voltage u_{DC} becomes 1.3 V (Fig. 3a). Negative voltage values u_{DC} (Fig. 3b) registered when voltage u_{IN} falls in the range $(-U_F, U_F)$ are attributable to resistance-inductance loading of bridge output (the two-terminal system R_dL_d). Voltage drop across bridge B2 is close to zero, whilst $u_{DC} \approx |u_h|$. Power loss in bridge circuit B2 is associated with voltage drop across the drain-source resistances in transistors Q1-Q3 or Q2-

Q4. Voltage drop across the transistors is proportional to their drain-source on state resistance and to current i_{DC} . The values of voltage u_{DC} are always positive – block CB with transistors Q1-Q4 is able to effectively dissipate energy stored in the magnetic field of the MR damper control coil.

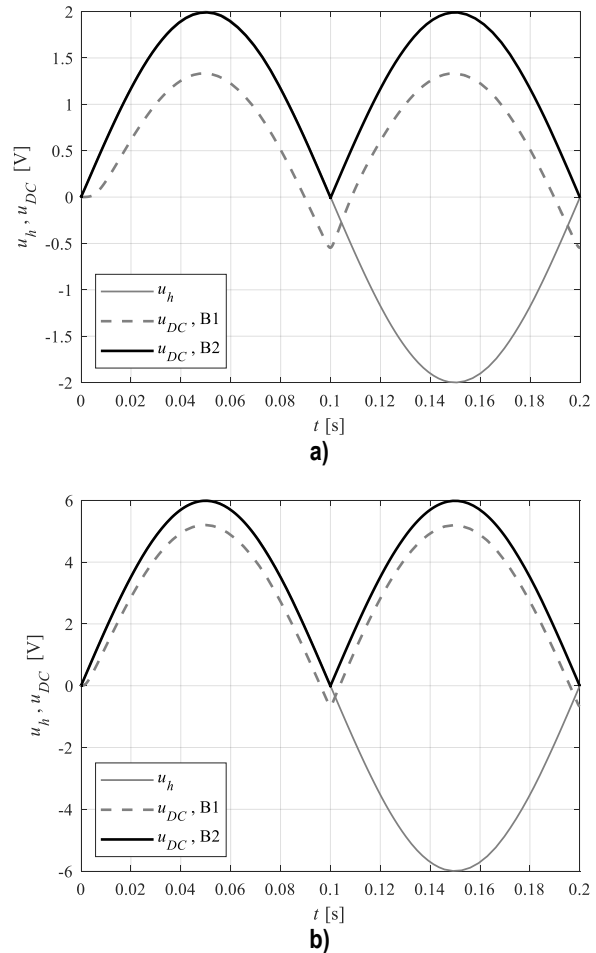


Fig. 3. Time histories of voltage u_h and u_{DC} : $f=5$ Hz; a) $A=2$ V, b) $A=6$ V

It appears that within the time period from 0 to 10 ms, when no magnetic field energy is yet accumulated in the damper control coil, the currents i_h (Fig. 4a) and i_{DC} (Fig. 5a) in bridge B1 begin to flow when $|u_h| > 0.7$ V. At the instant the voltage u_h reaches zero, the direction of current i_h flow is reversed (Figs. 4, 5) while maintaining its absolute value. Furthermore, immediately after the current flow i_h is reversed (when $0.1s < t < 0.11s$), its absolute value tends to decrease, despite an increase in absolute value of voltage u_h , which can be attributable to reduced current levels sustained in the circuit by the induction coil. The effect whereby the current flow is sustained by the damper control coil can be also observed for current i_{DC} whose minimal value at each time instant ($t > 0s$) exceeds zero. Lower current levels, i_h and i_{DC} , in bridge B1 are associated with the voltage drop across diodes D1-D4. The smaller the voltage u_{DC} , the smaller the current i_{DC} . The average current level i_{DC} for bridge B1 approaches 100 mA (when $A=2$ V, Fig. 5a). For the amplitude $A=6$ V (Fig. 5b), it is approximately equal to 0.5 A. The average current level i_{DC} for bridge B2 is larger than the average current level registered for bridge B1, its respective values for the amplitudes $A=2$ V and $A=6$ V being 200 mA and about 700 mA.

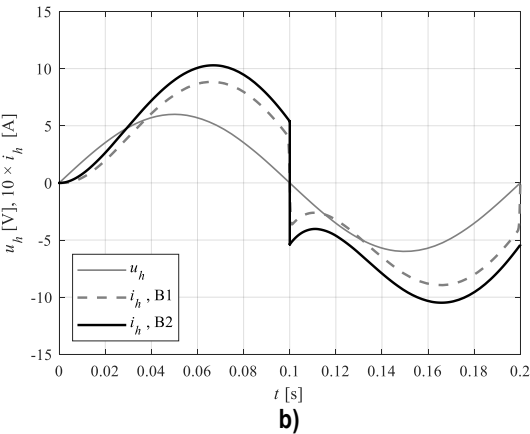
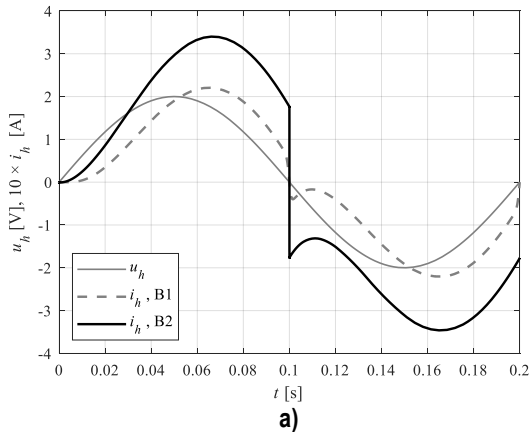


Fig. 4. Time histories of voltage u_h and current i_h ; $f=5$ Hz; a) $A=2$ V, b) $A=6$ V

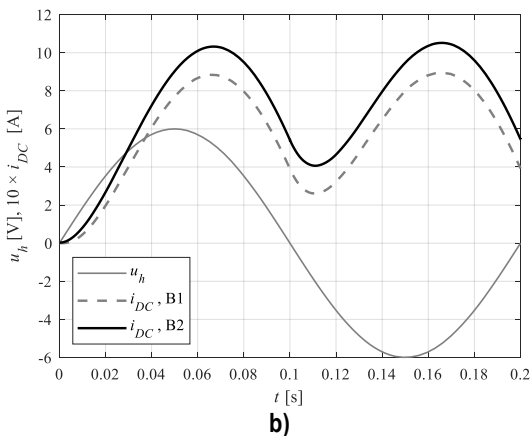
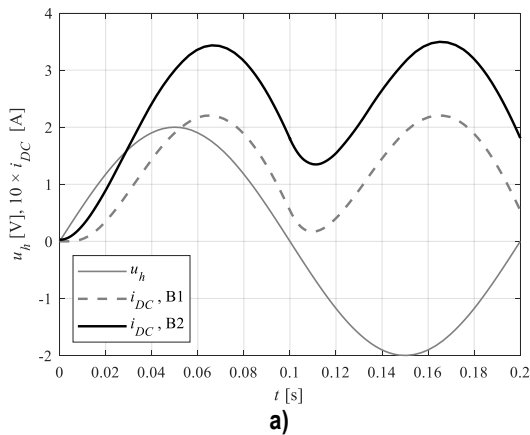


Fig. 5. Time histories of voltage u_h and current i_{DC} ; $f=5$ Hz; a) $A=2$ V, b) $A=6$ V

Bridge efficiency is derived from the formula:

$$\eta = 100 \frac{\frac{1}{T} \int_0^t u_{DC}(t) i_{DC}(t) dt}{\frac{1}{T} \int_0^t u_h(t) i_h(t) dt} [\%] \quad (1)$$

Plots in Fig. 6 show the bridge efficiency for B1 and B2 in the frequency range (0.5, 10) Hz, for amplitudes $A=2$ V and $A=6$ V. Apparently, bridge efficiency is improved when the amplitude is 6 V. Actually, bridge efficiency η is improved at higher amplitude of voltage u_h because the voltage u_{DC} supplying the MR damper control coil is equal to voltage u_h less the constant voltage value $2xU_F$, being the sum of voltage drops across the bridge components. One has to bear in mind, however, that the actual values of voltage drops $2xU_F$ may differ depending on the type of applied system components (diodes or transistors) and depending on the current level i_{DC} in those elements, whilst they are independent of the input voltage level u_h . As regards bridge B1, its efficiency decreases with increasing frequency, whilst that of bridge B2 remains nearly constant, exceeding 95%.

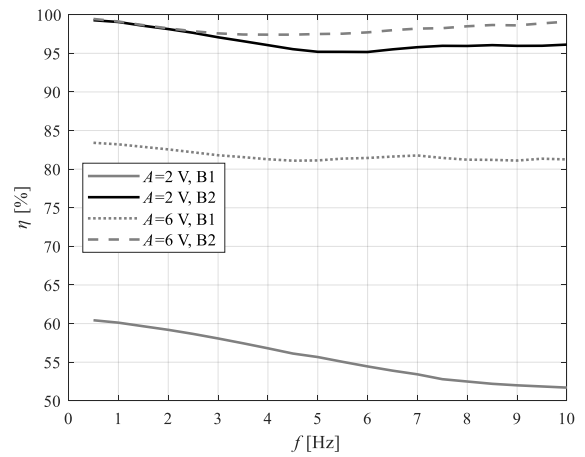


Fig. 6. Efficiency vs frequency

4. PCB FABRICATION

The development of PCB design of an ideal bridge (B2) was supported by the KiCad software (KiCad EDA, 2020). All components comprising the SB, CB and RB blocks are implemented on a double-sided laminate. Most components have the surface-mounting device housings. In the double-sided placement configuration, the components are placed in the top and bottom layers, which allows the PCB dimensions to be minimised (57 mm x 53 mm) and placed on a two-layer copper board. The laminate thickness was 1.6 mm, and the base copper thickness equal to 35 μ m. The copper plating was finished by the HASL (Hot Air Solder Levelling) method; thus, the conductive layer thickness was increased by several μ m. The path width for signal routing and for supplying the SB and CB clock circuits is 0.2 mm. The paths to handle the block RB and other high current connectors were implemented using the copper planes of paths with the minimal width 0.5 mm. The vias implementing the electric connections between copper layers and effecting the heat release were 0.3 mm in diameter. The number of vias was increased to handle high-current connections. The view of top and bottom of the bridge PCB is shown in Figs. 7a, b.

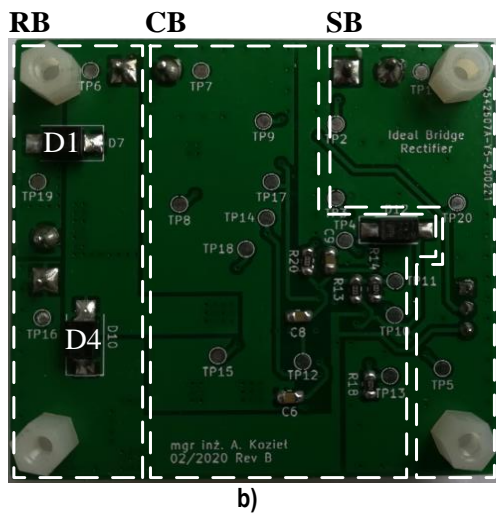
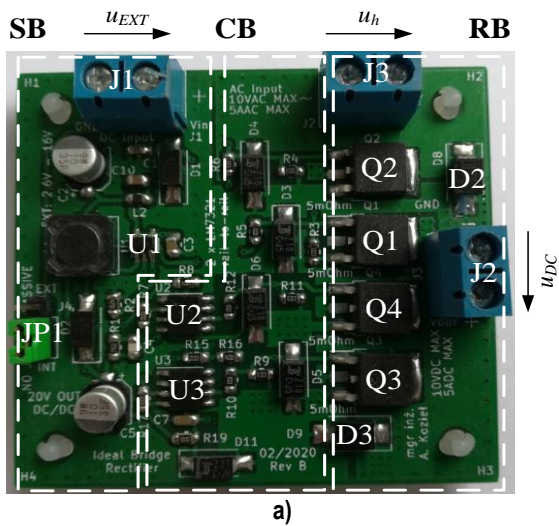


Fig. 7. Ideal rectifier bridge PCB: a) top view, b) bottom view

The PCB surface was subdivided into three respective areas to handle the SB, CB, RB blocks. The connections between regulator U1 and operational amplifiers U2 and U3 were designed to be as short as possible. The decoupling capacitors are placed close to the power supply terminal. Components that release heat (D1-D4 and Q1-Q4) in the RB block are separated from the SB and CB block circuits. The RB block connections were implemented on the power planes, which enabled the effective heat release to the PCB and to the ambience.

5. MEASUREMENT PROCEDURE

Bridge measurements were taken using the circuit shown schematically in Fig. 8, comprising a power amplifier (Sapiński et al. 2012) supplied from the power supply, voltage and current converters, an AD/DA board and a PC supporting the MATLAB/Simulink 2011b. The power amplifier generates alternating voltage fed to the bridge input (corresponding to u_h) in accordance with the command signal u_{con} generated at the AD/DA board output. The amplifier is fitted with integrated converters, enabling the measurements of voltage u_h and current i_h in the harvester coil. Voltage u_{DC} and current i_{DC} in the MR damper control coil are measured with voltage-voltage (u/u) and current-voltage (i/u) converters based on op-amps AD629 and AD8622.

Registered quantities were duly converted into voltage signals in the range (+10, -10) V, sampled by the AD/DA board at the frequency 1 kHz.

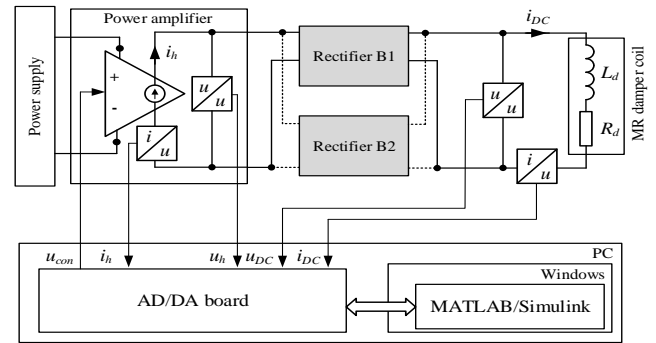


Fig. 8. Diagram of the measurement system

Finally, B2 measurement data are benchmarked against the results obtained for bridge B1 (based on Schottky diodes). One has to bear in mind that the measurements of bridge B2 were taken using an external power supply (a Li-Ion 3.7 V battery) – JP1 in position 2. Plots in Figs. 9-11 show time histories of measured and simulated steady-state voltages u_h , u_{DC} and currents i_h , i_{DC} , Fig. 12 plots efficiency η in the function of frequency 1, derived from formula (1).

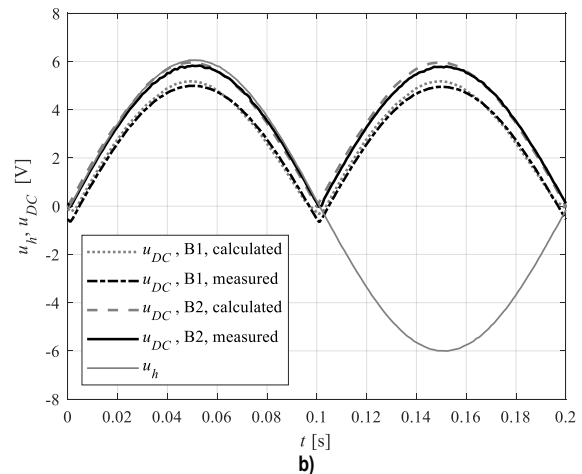
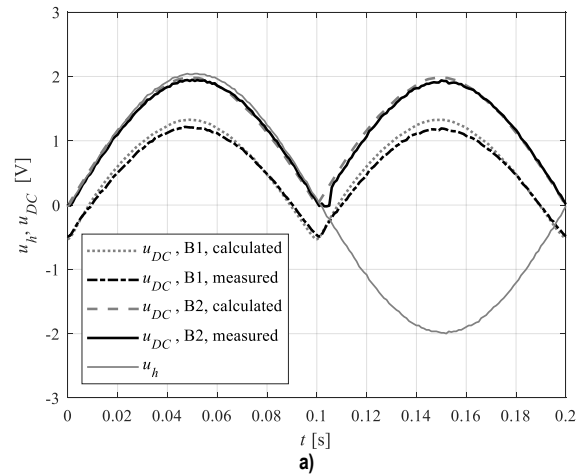


Fig. 9. Time histories of voltage u_h and u_{DC} : $f=5$ Hz; a) $A=2$ V, b) $A=6$ V

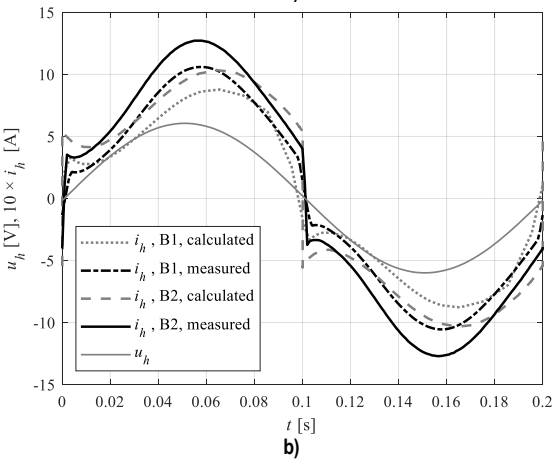
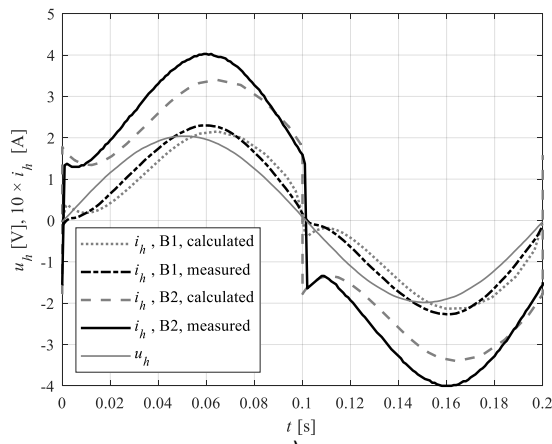


Fig. 10. Time histories of voltage u_h and current i_h : $f=5$ Hz; a) $A=2$ V, b) $A=6$ V

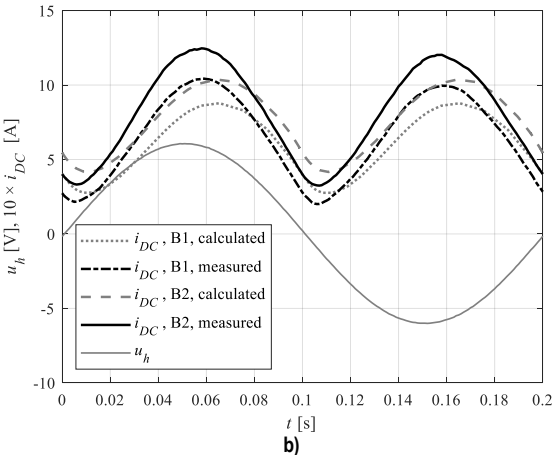
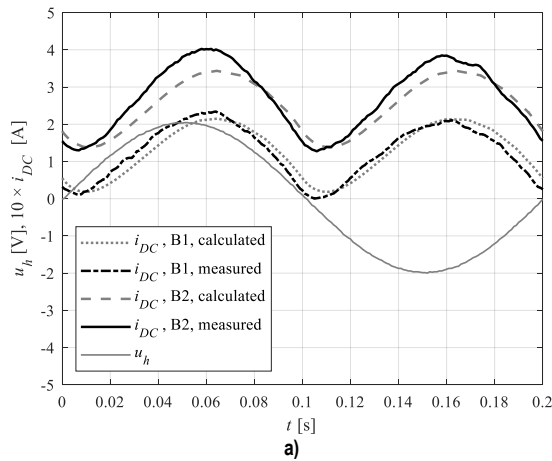


Fig. 11. Time histories of voltage u_h and current i_{DC} : $f=5$ Hz; a) $A=2$ V, b) $A=6$ V

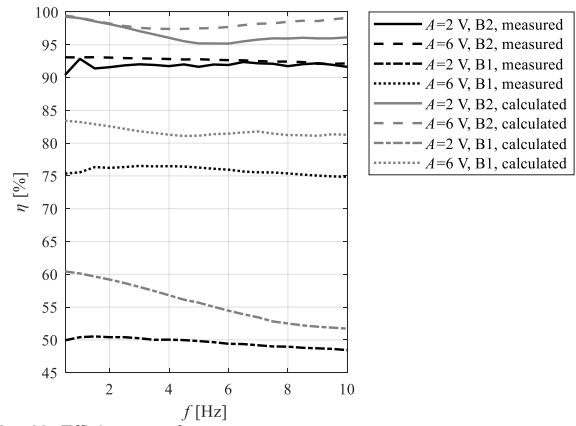


Fig. 12. Efficiency vs frequency

Measured voltages u_{DC} (Fig. 9) are in good agreement with the calculation results. Minor discrepancies are attributable to parasite resistances present in the bridge, not accounted for in the simulation model. The plots of i_h and i_{DC} (Figs 10-11) reveal certain discrepancies. The maximal difference between their instantaneous values for $A=6$ V is found to be 0.2 A and is registered for the two bridges under consideration. Actually, these discrepancies are the result of eddy currents induced in ferromagnetic material from which the MR damper rod is made. The simulation procedure used a solenoid coil where such phenomenon should not occur. The efficiency of bridge B2 obtained experimentally is 92%; for bridge B1, the respective values are: 50% (for $A=2$ V) and 75% (for $A=6$ V). These are found to be less than the simulated results, mostly due to the occurrence of eddy currents and parasite resistances (Fig. 12).

6. APPLICATION AND TESTING

To verify the adequacy of the newly developed bridge B2 design, experimental tests were conducted in the test rig (Sapiński et al. 2010) incorporating the harvester prototype, the RD-8040-1 damper, a passive spring rated at $k=90,000$ N/m attached to the sprung mass $m=155$ kg, a shaker and a measurement system (Fig. 13). The natural frequency of the SDOF system (sprung mass-damper-spring) is $f_0=3.8$ Hz. The measurement system comprised a PC, an AD/DA board supporting the MATLAB/Simulink, displacement sensors (S1, S2), force sensors (S3, S4), voltage-voltage (u/u) and current-voltage (i/u) converters. Measurements were taken of the shaker core displacement (input excitation) z , sprung mass displacement x , force F_{in} generated by the shaker, damper force F_d , voltage and current levels in the harvester coil u_h and i_h , voltage and current in the bridge u_{DC} and i_h (voltage and current in the MR damper control coil).

The excitations applied in the testing procedure were in the form of displacement inputs z with the amplitude 3.5 mm and frequency varied from 2 Hz to 10 Hz, with the step 0.1 Hz. Each test took 30 s and involved three phases: increasing the amplitude of applied inputs (0, 10) s, maintaining the amplitude of applied excitation on the fixed level (10, 20) s, decreasing the amplitude of excitation (20, 30) s. Figs. 14-16 plot the results of tests done in the time interval (10, 20) s, while the amplitude z of the applied excitation remained constant. Figs. 14-15 show the respective time histories of input voltage and current (u_h, i_h), output voltage and current (u_{DC}, i_{DC}) in bridges B1 and B2. Fig. 16 plots the displacement transmissibility coefficient T_{xz} in the function of frequency for the SDOF system governed by formula (2); expressing the efficiency of reduction of the sprung mass vibration amplitude.

$$T_{xz} = \frac{\sqrt{\int_0^T x(t)^2 dt}}{\sqrt{\int_0^T z(t)^2 dt}} \quad (2)$$

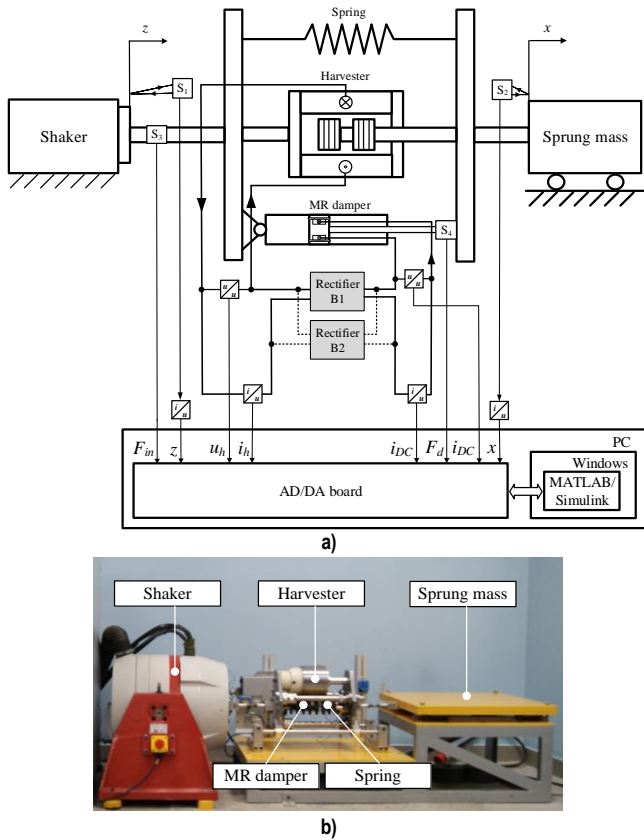


Fig. 13. The test rig: a) schematic diagram, b) general view

It is readily apparent (see Fig. 14) that instantaneous values of voltage in the harvester u_h supplying bridge B1 are larger than the voltage supplying bridge B2 – it appears to be the consequence of a larger relative velocity of magnets motion with respect to the harvester coil, which is associated with a larger amplitude of sprung mass vibrations x (see Fig. 16). The maximal instantaneous values are about 2V (B1) and 1.4 V (B2). Despite lower values of voltage u_h at the input to B2, currents i_h in the two bridges are similar in value, not exceeding 200 mA. Moreover, instantaneous values of voltage u_{DC} at the bridge outputs are similar, too (Fig. 15), whilst the only registered discrepancy is the occurrence of negative values of instantaneous voltage, not exceeding -350 mV in the case of bridge B1. As regards bridge B2, no negative values of instantaneous voltage u_{DC} are registered, and so, the instantaneous current intensity i_{DC} in the damper control coil reaches a slightly higher value than in B1, which is indicative of lower loss of energy supplied to the control coil via bridge B2. In consideration of the voltage difference $|u_h - u_{DC}|$, it appears that the voltage drop across bridge B1 is 0.7 V, whilst for bridge B2, it becomes 20 mV. This observation is in good agreement with the results of simulations and measurements, outlined in Sections 4 and 5.

Transmissibility plots T_{xz} in Fig. 16 were derived under the following conditions of power supply to the MR damper control coil (the two-terminal network): no power supply (Case 1), direct supply from the harvester (Case 2), power supply from bridge B1 (Case 3), power supply from bridge B2 (Case 4). Apparently, the amplitude of sprung mass vibration in Case 4 is vastly reduced in the frequency

range (2, 6.5) Hz in relation to Case 2, whilst the maximal value of this coefficient registered at 3.9 Hz approaches $T_{xz}=1.4$. Its respective values registered in the remaining cases are: $T_{xz}=3.4$ at frequency 3.8 Hz (Case 1); $T_{xz}=1.6$ at frequency 4.1 Hz (Case 2); $T_{xz}=1.7$ at frequency 3.5 Hz (Case 3).

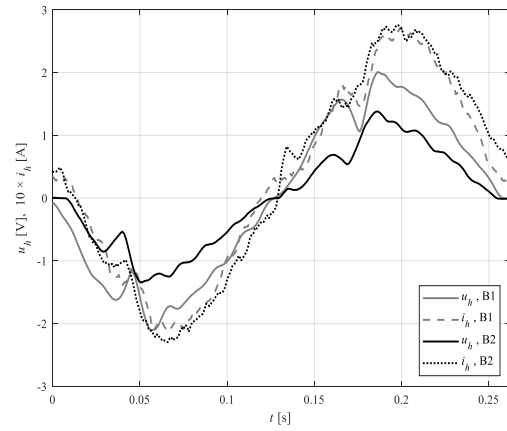


Fig. 14. Time histories of voltage u_h and current i_h ; $f = 3.8$ Hz

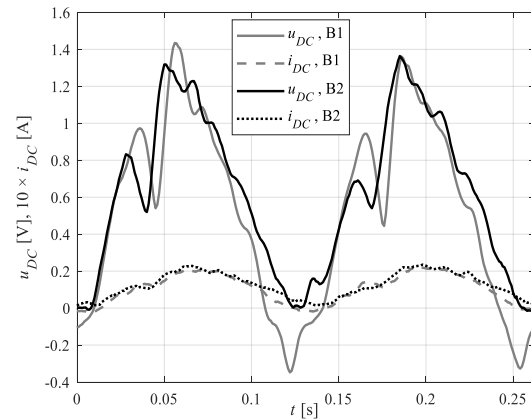


Fig. 15. Time histories of voltage u_{DC} and current i_{DC} ; $f = 3.8$ Hz

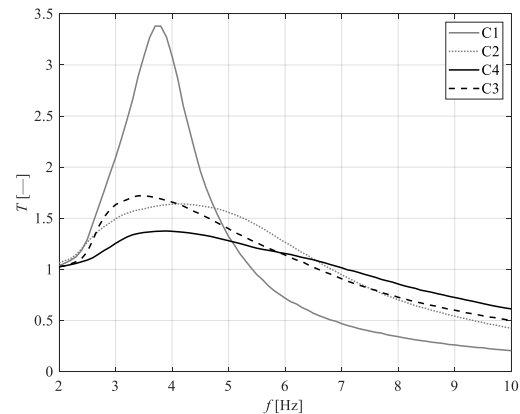


Fig. 16. Transmissibility coefficient T_{xz} vs frequency f

Obviously (see the plots in Fig. 1), the application of bridge B2 should be most favourable, as the amplitude of spring mass vibration is thus significantly reduced in the neighbourhood of resonance frequency, whilst the system's behaviour is less favourable at frequencies in excess of 5 Hz in Cases 2, 3, 4 when compared to Case 1.

This effect can be attributed to the presence of an MR damper dissipating energy placed in between the source of vibration (kin-

ematic input) and the sprung mass. In such system, when the excitation frequency should exceed $\sqrt{2}f_0$, the increase of damping in the system results in increased amplitudes of the sprung mass vibration. Its performance and condition will further deteriorate due to growing amounts of electric energy generated by a harvester at frequencies in excess of 5 Hz. In order to overcome this drawback, it is suggested that additional passive circuits converting the alternating current should be provided in between the harvester coil and the MR damper coil (Jastrzębski and Sapiński, 2017).

7. SUMMARY

The main aim of the study was to develop an ideal rectifier bridge to convert the AC signal to positive voltages in an MR damper-based regenerative vibration reduction system. Its structural design and fabrication techniques are outlined, and the results of simulations and laboratory testing are collated. The advantages of the newly developed bridge are demonstrated by benchmarking the measurement results against those obtained for a rectifier bridge based on Schottky diodes, leading us to the following conclusions.

- In the case of bridge B1, the power loss in the harvester coil – MR damper control coil circuit is largely due to power loss in Schottky diodes (in the form of heat release). The actual level of power loss is associated with forward voltage and current flowing in diodes. In the case of bridge B2, the power loss is associated with the drain-source on-state resistance of transistors and current flowing through them. Compared to bridge B1, power loss is significantly reduced, and thus, the efficiency of the bridge (B2) can be improved.
- Efficiency of bridge B1 increases with increasing amplitude of voltage u_h and tends to decrease with increasing frequency. Efficiency of bridge B2 is constant; it is unrelated to the amplitude of voltage u_h and frequency f . For bridge B1, the efficiency becomes 75 %, for B2 – 92 %.
- Bridge B2 requires an external source of electric power to supply the electronic circuit for transistor control. This energy may be obtained by harvesting the energy of sprung mass vibration. In the case of no external supply, efficiency of bridge B1 is similar to that of bridge B2.
- In the vibration reduction system incorporating bridge B1, the value of transmissibility coefficient T_{xz} will not change by more than $\pm 6\%$ in relation to the case where the MR damper control coil is supplied directly from the harvester. Apparently, the amplitude of sprung mass vibration is decreased only in the frequency range (4, 7) Hz.
- Application of bridge B2 in the vibration reduction system results in a nearly 15% reduction of the sprung mass vibration amplitude in relation to the case where the bridge is absent. This effect is registered in the frequency range (2, 6.5) Hz.
- In each investigated case where the MR damper control coil is supplied from the harvester (with or without the bridge), at frequencies exceeding 5 Hz, the amplitude of sprung mass vibration tends to increase in relation to the case where the coil is not supplied. This is best revealed in systems incorporating bridge B2, and this drawback can be overcome through the application of passive electric circuits utilising the voltage resonance effect.

Further studies will investigate the electronic systems for conditioning of voltage generated by the harvester, and a dedicated high-efficiency DC/DC converter is planned to be developed.

REFERENCES

1. **Balato M., Costanzo L., Vitelli M.** (2017), Resonant electromagnetic vibration harvesters: Determination of the electric circuit parameters and simplified closed-form analysis for the identification of the optimal diode bridge rectifier DC load. *International Journal of Electrical Power and Energy Systems* 84, 111-123.
2. **Chytil J.** (2014), Practical realization of ideal diode full-wave rectifiers, *Informatics Control Measurement in Economy and Environment Protection*, vol.4, no.4, 81-84.
3. **Grzybek D., Micek P.** (2017), Piezoelectric beam generator based on MFC as a self-powered vibration sensor, *Sensors and Actuators A: Physical*, 267, 417-423.
4. **Jastrzębski Ł., Sapiński B.** (2017), Electrical interface for an MR damper-based vibration reduction system with energy harvesting capability. *Proceedings of 18th International Carpathian Control Conference ICCO 2017*.
5. **Maiorca F., Giusa F., Trigona C., Ando B., Bulsara A. R., Baglio S.** (2013), Diode-less mechanical H-bridge rectifier for "zero threshold" vibration energy harvesters, *Sensors and Actuators A: Physical*, 201, 246-253.
6. **Safaei M., Sodano H. A., Steven R Anton S. R.** (2019), A review of energy harvesting using piezoelectric materials: state-of-the-art a decade later (2008–2018), *Smart Materials and Structures*, 28, 113001.
7. **Sapiński B.** (2010), Vibration power generator for a linear MR damper, *Smart Materials and Structures*, 19, 105012.
8. **Sapiński B.** (2011), Experimental study of a self-powered and sensing MR-damper-based vibration control system, *Smart Materials and Structures*, 20, 105007.
9. **Sapiński B.** (2014), Energy-harvesting linear MR damper: prototyping and testing, *Smart Materials and Structures*, 23, 035021.
10. **Sapiński B., Jastrzębski Ł., Rosół M.** (2012), Power amplifier supporting MR fluid-based actuators, *Proceedings of 13th International Carpathian Control Conference ICCO 2012*, 612–616.
11. **Sapiński B., Snamina J., Jastrzębski Ł., Staśkiewicz A.** (2010), Laboratory stand for testing of self-powered vibration reduction systems, *Journal of Theoretical and Applied Mechanics*, Vol. 49, No. 4.
12. **Selevaraj K.** (2019), Basics of Ideal Diodes, Texas Instruments, <http://www.ti.com/lit/an/slvae57/slvae57.pdf>
13. **Snamina J., Orkisz P.** (2014), Energy Harvesting from Vibrations of a Two-Degree-of-Freedom Mechanical System, *Acta Physica Polonica A*, vol. 125, no. 4A, 174-178.
14. **Sung K. G., Choi S. B.** (2008), Effect of an electromagnetically optimized magnetorheological damper on vehicle suspension control performance. *Proc. of the Institution Mechanical Engineers Part D Journal of Automobile Engineering*.
15. **Wang D. H., Liao W. H.** (2009a), Semi-active suspension systems for railway vehicles using magnetorheological dampers. Part I: System integration and modelling, *Vehicle System Dynamics*.
16. **Wang D. H., Liao W. H.** (2009b), Semi-active suspension systems for railway vehicles using magnetorheological dampers. Part II: Simulation and analysis, *Vehicle System Dynamics*.
17. **Lord Corporation** (2020), MR damper, RD-8048-1, Technical documentation, www.lord.com
18. **KiCad EDA** (2020), User manual, <https://www.kicad-pcb.org/>
19. **Analog Devices** (2020), LTSpice, User manual, <https://www.analog.com/>
20. **Infineon** (2020), IRFH5007, Technical documentation, <https://www.infineon.com>
21. **RHOM** (2020), RBR2MM60C, Technical documentation, <https://www.rohm.com/>

This work is supported by AGH University of Science and Technology under research program No. 16.16.130.942.

EXPERIMENTAL ESTIMATION OF WEAR RESISTANCE OF POLYAMIDE COMPOSITES, REINFORCED BY CARBON AND GLASS FIBRES USED IN METAL-POLYMER GEARINGS

Myron CHERNETS,* Myroslav KINDRACHUK,* Anatolii KORNIENKO*, Alina YURCHUK**

*Aerospace Faculty, Department of engineering, standardization and certification,
National Aviation University, 1, Liubomyra Huzara ave., Kyiv, Ukraine, 03058

**Aerospace Faculty, Department of computerized electrotechnical systems and technologies,
National Aviation University, 1, Liubomyra Huzara ave., Kyiv, Ukraine, 03058

myron.czerniec@gmail.com, nau12@ukr.net, anatoliy_k@ukr.net, pruner@ukr.net

received 18 May 2020, revised 3 March 2021, accepted 5 March 2021

Abstract: The method of model triboexperimental studies to determine the basic mathematical model parameters of materials wear resistance at sliding friction is considered. The quantitative relative experimental characteristics of wear resistance of glass fibre and carbon fibre reinforced polyamide used in metal-polymer gear couple have been determined. Wear resistance functions of these functional polymeric composites have been established as the basic ones in the tribokinetic mathematical model of material wear for sliding friction conditions. Also, according to the conducted researches, wear resistance diagrams were constructed. They may be used as graphical indicators of wear resistance in the required range of specific friction forces. The dependences that connect the characteristic functions of wear resistance of these materials (obtained by the developed mathematical tribokinetic wear model) with linear wear and gearing service life are presented.

Keywords: Method for determining the characteristics and functions of wear resistance, reinforced polyamide, dispersed glass and carbon fibres, metal-polymer gears

1. INTRODUCTION

New developments in industrial technologies require constant improvements of materials used (Kindrachuk et al, 2018). New hardfacing and advanced materials are always introduced, and many of them will find their application much later (Pashechko et al., 2018, Gorokh et al., 2018). A very important task here is the prediction of wear loss, or service life of mechanisms and machines, but most scientists predict durability of materials only. Various methods and power schemes of triboexperimental studies to evaluate the wear resistance of materials are used. Here, it is possible to determine the absolute and relative characteristics of the studied tribocouple's materials under the given conditions. They can be used to make a comparative assessment of materials' wear resistance under identical test conditions. The most common of these include linear, mass and volume wear loss (absolute characteristics) and the intensity and rate of wear (relative characteristics). It is more convenient to use relative wear characteristics. These quantitative characteristics of materials' wear resistance are traditionally determined under specified normal loading in tribocouple. However, the calculation methods for estimating wear using them are not adequate as far as they are, as a rule, calculated for one value of specific load. Therefore, it is necessary to perform numerical triboexperimental studies of tribocouples in a sufficiently wide range of specific loads, the results of which should establish the characteristics of wear resistance. These characteristics will become the basic ones in mathematical models of wear kinetics of sliding (or rolling with

slippage) tribocouples. Polymeric materials have some peculiarities if they operate in couple with steels, and we should take this into account (Kindrachuk et al., 2019 a, b,).

This paper presents the results of the studies on the method of model triboexperiments (Chernets and Lenik, 1997, Chernets, 2019) with sliding friction to establish the wear resistance characteristics of reinforced polyamide composites paired with steel used in metal-polymer gear couple.

2. STATE OF THE ART

As it is known, during the operation of gears under the influence of friction forces acting on the gear in the torque transmission, tooth wear occurs inevitably. The wear rate is the practical criterion that determines the gears' lifespan (Zarkoa et al., 2019, Greco et al., 2011). However, despite the obvious necessity at the design stage of carrying out the predicted calculation of gears' durability according to the criterion of acceptable linear wear of the teeth, effective and reliable methods of calculation have not yet been developed. There are several methods of calculation of this kind in the literature. In the 1970s and 1980s, Drozdov Yu.N. has been working on this problem in USSR. (Drozdov, 1969, 1975, Drozdov and Nazhestkin, 1990, Pronikov, 1978, Grib, 1982). There is no continuation of these studies by other investigators in the countries of the former USSR. Since the late 1990s, several scientists have been developing such methods to calculate certain types of gears. Among them, there are: Bajpai et al., (2004), Brauer and Andersson, (2003), Flodin, (2000), Flodin and

Andersson (1997, 1999, 2000, 2001), Kahraman et al., (2005), Kolivand and Kahraman (2010), Mao (2007), Pasta and Mariotti (2007), Wu and Cheng (1993). Archard's law of abrasive wear is used in all simplified calculation methods to evaluate wear of teeth. According to him, the wear rate is linearly dependent on the friction path and contact pressure. In closed gearings operated with lubrication, abrasive wear does not occur and the use of these methods is therefore unreasonable. Besides, other factors are not covered by these methods, which will be discussed below. This fact makes it impossible to use them in engineering practice. Even in open gear drives, abrasive wear is also uncommon, because in the presence of an abrasive medium, gears quickly lose their performance.

The estimation of service life of gearings is a very important task. Reasons of gearings failure may vary a lot. Basically, teeth may fail due to fatigue or sudden rupture (Geçura et al., 2019), surface fatigue (Brandao et al., 2014), fretting-fatigue (Wei et al., 2020), contact-fatigue (Liu et al., 2020) or may be worn out (Brethee et al.). In problem of lifespan estimation, scientists focus their attention to particular reasons of failure. Brandao et al. (2014) did a study of pitting and fatigue influence on gears wear. They developed a numerical model that involves simulation of micropitting and fatigue wear. But, these two processes were modelled separately and combined later. DIN 20MnCr5 steel was used as gear material. Bravo et al. (2015) were solving the task of gear couple deterioration until the final failure. They point out the complexity of this task. Both gears were manufactured of plastic materials. Authors succeeded a lot in developing effective means to extend the time for plastic gear applicability.

Hegadekatte et al. (2010) studied the wear in miniature gear mechanisms made of ceramics or cemented carbides. The Archard's wear model was selected as the most appropriate. Simulation was done using FEM method. This time, the lifespan prediction by this method for macrogears is questionable. To determine wear coefficient, they used experimental pin-on-disk and twin-disc wear data. Wang et al. (2019) made a numerical model and simulations of wear process of heavy loaded helical gears based on the modified Archard's wear model for elastohydrodynamic lubrication. They also found relations between load factors, gear geometric parameters and wear rate of tooth contact surface. These data, unfortunately, were not checked experimentally.

The surface condition and gear modification also influence simulation; besides, the roughness effect during simulations is also an important factor. Bodach et al. (2012) studied the numerical simulation of positively modified gears' roughness influence on lubrication and wear process. Results showed that tooth geometry change influences much more than change in roughness during operation. Guilbault and Lalonde (2019) made a significant effort to predict tooth roughness change with high accuracy (1.27 μm predicted compared to 1.3 μm measured). They proved that micropitting failure starts on the surface, while pitting crack initiates at some depth under the surface. But, both these studies cannot spot the method to predict lifespan of the gear.

Raadnui (2019) studied the wear and other deterioration processes of gears, including contamination and corrosion influence on gears conditions. He deduced the relationships between operating conditions, wear debris size, morphology and failure mode. This work's results can't be used directly to predict the lifespan of gear trains, but may be used for quantitative prediction of wear loss. For wear tests, he used a test set with two industrially produced gears engaged.

The dynamic wear prediction model established by Liu et al., (2016) has a task to connect surface wear process and gear dynamics. At low rpm, the effect of initial tooth wear is negligible, but as rpm rises, the wear effect becomes more significant. But, the question about experimental studies still requires a solution. Feng et al. (2019) updated the dynamic model by taking into account vibrations occurring during operation, and vibration-wear bias. Tooth wear was monitored continuously and corrected tooth shape (as a result of wear) continuously being added to the model. All the results were checked by laboratory gear test rig. This model may predict the wear of gears with acceptable accuracy.

3. WEAR TEST PROCEDURE

When conducting model triboexperimental studies, they usually use plane friction contact. In this case, the conditions of wear are unchanged throughout the experiment. A pin-on-disc tribometer is a very good solution for that.

To study the polymer composite-steel couple's wear, a friction PoD layout was used (composite pin – AISI 1045 steel disk).

In the current work, tribological tests were conducted using a pin-on-disk test layout (composite pin – steel disk), which ensures that the conditions of friction and wear are constant during the experiment. The following research program was used: contact pressure $P = 1, 2, 5, 10, 20$ MPa, sliding speed $v = 0.4$ m/sec, wear path = 2000 m, diameter of pin $d = 2$ mm. Friction factor measured for materials was 0.3.

For wear test, we used Anton Paar tribometer TRB³ (Fig. 1).



Fig. 1. High temperature Anton Paar tribometer TRB³

This tribometer allows to have 60N deadweight load, and combined with standard specimen, 20 MPa contact pressure may never be achieved. But, to meet the requirements of the test, a modified pin specimen was manufactured (Fig. 2). The contact area of the modified specimen with cone section is 3 mm², which gives 20 MPa at 60N load. Reduced pin diameter section length is about 2 mm, and no plain contact distortion was observed. Mass

wear loss was measured by electronic balances with accuracy 0.001 g Axis model ANG 200 C.

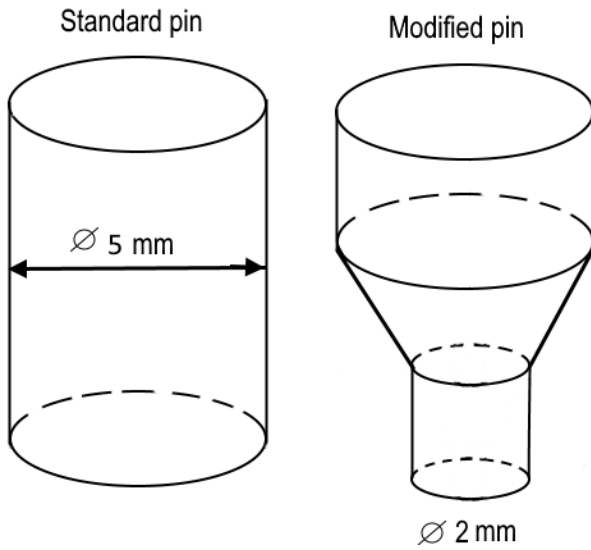


Fig. 2. Standard and modified pin for TRB³ tribometer

4. RESULTS AND DISCUSSION

After the wear test, mass wear loss ΔM of specimens was determined, and their average linear wear h was calculated by the formula:

$$h = \frac{\Delta M}{\rho S}, \quad (1)$$

where ρ is the density of polyamide composite with 30 wt. % of fibre reinforcement; S is the nominal contact area.

The next stage of data processing of triboexperimental studies was the establishment of experimental wear resistance model characteristics, in particular wear resistance functions Φ_i at certain levels of specific friction forces τ_i in friction contact

$$\Phi_i = L_i/h_i, \quad (2)$$

where $L_i = vt$ is friction path, v – friction velocity, t is the duration of the experiment, h_i – linear wear of samples, τ_i is the discrete value of specific friction force at contact pressure i . We should note that the friction forces can be significantly different with the same contact pressure in the tribomechanical system. They depend on the sliding friction coefficient, which can be in a wide range (from 0.005 to 0.01 for mixed friction, from 0.05 to 0.1 for boundary friction, from 0.1 to 1.0 for dry friction) (Kurdi et al., 2018, Bongaerts et al., 2018, Wand and Wang, 2013). The specific friction force, the value of which determines the wear rate of tribosystem elements, in tribotechnology is calculated by Amonton – Coulomb formula:

$$\tau = fP, \quad (3)$$

where f is friction coefficient; P is nominal contact pressure.

The final stage of processing experimental data is to determine the basic characteristics of wear resistance for a mathematical model of the study of materials wear kinetics at sliding friction (Chernets and Lenik, 1997, Chernets et al., 2011). Using the established by (2) discrete experimental characteristics of wear resistance – wear resistance functions. Their approximation is

performed according to the following relation (Chernets, 2019a, Chernets et al., 2011):

$$\Phi_k(\tau) = C_k \left(\frac{\tau_{sk}}{\tau} \right)^{m_k}, \quad (4)$$

where C_k, m_k – are nonlinear and exponential wear resistance characteristics of tribocouple materials, which are determined by formula (4) through approximation by the method of least squares through several iterations based on the experimental values of wear resistance functions Φ_i determined earlier by formula (2), τ_s – shear strength of materials, $k = 1; 2$ – designation of tribocouple elements. The characteristic function of wear resistance is the basic integral parameter of the developed mathematical wear model (Chernets and Lenik, 1997, Chernets et al., 2011, Chernets, 2019b).

The above procedure was used to determine the wear resistance characteristics C_k, m_k of polyamide composites with a filler volume fraction of 30% coupled with steel (calculated by formula (4)):

carbon fibre reinforced polyamide PA6 + 30CF (UPA – 6130 UV): $= C_{CF} = 3.1 \cdot 10^5, m_{CF} = 2.3, \tau_{SCF} = 48$ MPa; glassfibre reinforced polyamide PA6 + 30GF (PA6-L-CB30-1): $= C_{GF} = 1.26 \cdot 10^5, m_{GF} = 1.9, \tau_{SGF} = 52$ MPa.

On Fig. 3, points show the experimental discrete values of the calculated wear resistance functions $\Phi_i = \Phi_i(\tau_i)$ of both the composites, and the lines show their wear resistance diagrams $\Phi(\tau) \sim \tau$ as indicators of their wear resistance in the studied range of friction forces.

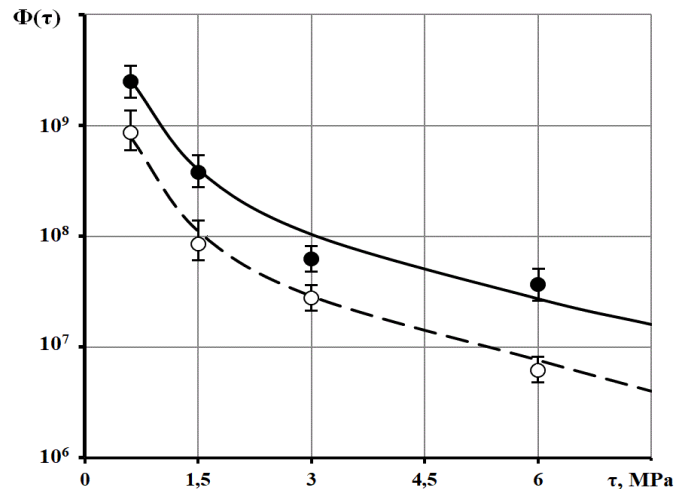


Fig. 3. Diagram of wear resistance of polyamide composites: solid line – carbon fibre reinforced composite, dashed line – fiberglass reinforced composite; dark circles – experimental values of wear resistance function for carbon fibre composite, light circles – for fiberglass reinforced composite. Each point is an average value of 3 wear tests

The above mentioned material's wear resistance diagram (WRD) allows to visually evaluate the material's wear resistance over the entire range of specific friction force change. In addition, when studying the wear of several materials, it is easy to compare their wear resistance under different loading conditions.

Based on the results of triboexperimental studies and WRD of these polymeric composites, the comparative wear resistance was evaluated, and we found that carbon fibre-reinforced composite

would be $C_{CF}/C_{GF} = 2.46$ times more wear resistant than fibre-glass reinforced composite.

Wear resistance is inverse to wear intensity. Therefore, respectively, experimental inverse function of linear wear resistance will be the experimental function of the intensity of linear wear $I_{hi}(\tau_i)$ for corresponding values of specific friction force τ_i :

$$\frac{1}{\Phi_i(\tau_i)} = \frac{h_i}{L_i} = I_{hi}(\tau_i), \quad (5)$$

Also, wear resistance function $\Phi_i(\tau_i)$ is related to the linear wear rate $\gamma_{hi}(\tau_i)$ by the following formula:

$$\Phi_i(\tau_i) = v/\gamma_{hi}(\tau_i), \quad (6)$$

and inverse:

$$\gamma_{hi}(\tau_i) = v/\Phi_i(\tau_i) = vI_{hi}(\tau_i), \quad (7)$$

So, these experimental evaluation results of materials' wear resistance may be compared with the results of other authors obtained under similar wear conditions, first of all, at the same range of specific friction force and sliding speeds.

Basic wear characteristics may be used to calculate the total linear wear of tribomechanical sliding system if wear characteristics of one of its elements are known. This is especially important in case of dissimilar wear resistance of coupled materials and dissimilar tribocontact conditions. Total linear wear of tribosystem h_{Σ} can be calculated as follows:

$$h_{\Sigma} = h_1 + h_2 = h_1(1 + h'_1) = h_2(1 + h'_2), \quad (8)$$

where h'_1, h'_2 – relative linear wear of coupled elements (pinion 1 and gear 2).

They are calculated as $\Phi_k(\tau)$ taking into account (4) according to the following dependencies:

$$\begin{aligned} h'_1 &= \frac{h_2}{h_1} = \frac{\Phi_1(\tau)}{\Phi_2(\tau)} = \frac{C_1 \tau_{S1}^{m_1} \tau^{m_2}}{C_2 \tau_{S2}^{m_2} \tau^{m_1}} K_t^{(2)}, \\ h'_2 &= \frac{h_1}{h_2} = \frac{\Phi_2(\tau)}{\Phi_1(\tau)} = \frac{C_2 \tau_{S2}^{m_2} \tau^{m_1}}{C_1 \tau_{S1}^{m_1} \tau^{m_2}} K_t^{(1)}, \end{aligned} \quad (9)$$

where $K_t^{(1)}, K_t^{(2)}$ – coefficients of elements mutual overlapping at tribological contact.

Correspondingly, in a gearing:

$$h_{\Sigma} = h_k (K_t^{(k)} + h'_k);$$

$$h_{\Sigma} = h_1 (-K_t^{(1)} + h'_1);$$

$$h_{\Sigma} = h_2 (K_t^{(2)} - h'_2);$$

$$K_t^{(1)} = 1,$$

$$K_t^{(2)} = z_1/z_2, \quad (10)$$

where z_1, z_2 are respectively the number of teeth of pinion and gear.

Linear wear h_k of gears teeth are interrelated, so:

$$h_1 = \frac{h_2 h'_2}{K_t^{(2)}}; \quad h_2 = \frac{h_1 h'_1}{K_t^{(1)}}, \quad (11)$$

Taking into account (2):

$$vT_1 = \Phi_1 h_1; \quad vT_2 = \Phi_2 h_2, \quad (12)$$

where T_1 and T_2 – are the durabilities of the studied tribocouples. Accordingly, relative durabilities T'_1 and T'_2 of tribomechanical system elements will be determined as:

$$T'_1 = \frac{T_2}{T_1} = \frac{\Phi_2(\tau) h_2 K_t^{(2)}}{\Phi_1(\tau) h_1 K_t^{(1)}} = \frac{\Phi_2^2(\tau)}{K_t^{(1)} \Phi_1^2(\tau)}$$

$$T'_2 = \frac{T_1}{T_2} = \frac{\Phi_1(\tau) h_1 K_t^{(1)}}{\Phi_2(\tau) h_2 K_t^{(2)}} = \frac{\Phi_1^2(\tau)}{K_t^{(2)} \Phi_2^2(\tau)} \quad (13)$$

Then,

$$T_1 = \frac{T_2 \Phi_1^2(\tau)}{\Phi_2^2(\tau) K_t^{(2)}} = T_2 T'_2;$$

$$T_2 = \frac{T_1 \Phi_2^2(\tau)}{\Phi_1^2(\tau) K_t^{(1)}} = T_1 T'_1. \quad (14)$$

5. CONCLUSIONS

The method of triboexperimental studies of materials at sliding friction according to pin-on-disk friction layout provides the correct determination of relative wear resistance characteristics Φ_i of materials due to the invariance of tribocontact conditions throughout the experiment. The developed method's efficiency is confirmed by an example of the tests given here of the two types of polyamide-based composite materials PA+30%CF and PA6+30%GF under the studied range of specific friction forces.

Obtained experimental values of Φ_i were used to construct wear resistance diagrams of the studied materials. They graphically display their wear resistance (Fig. 3).

These wear resistance diagrams of materials, as graphical indicators of their wear resistance, allow to determine the comparative wear resistance of the studied composites for any required value of specific friction force.

Determined as a result of approximation of experimental wear resistance indicator values (functions Φ_i) and material's wear resistance characteristics C_k, m_k are required for the assessment of wear and durability of metal-polymer gears by the developed method of gears calculation (Chernets et al, 2011, Chernets, 2019, Chernets and Chernets, 2017) or by the corresponding numerical methods used in problems of contact mechanics (Kindrachuk and Galanov, 2014).

Using the characteristics of material's wear resistance C_k, m_k in tribocouple, it is possible to determine the relative linear wear of tribosystem elements h'_1, h'_2 , their total wear resistance h_{Σ} and durabilities T_1 and T_2 of tribosystem elements.

This methodology allows transforming wear rates, friction force values, and friction factors, available from scientific literature, into wear resistance functions. Thus, any of the results obtained with dissimilar test methods may be used as a database for further research.

REFERENCES

1. Bajpaj P., Kahraman A., Anderson N.E. (2004), A surface wear prediction methodology for parallel-axis gear pairs, *Journal of Tribology*, 126, 597–605.
2. Bobach L., Beilicke R., Bartel D., Deters L. (2012), Thermal elastohydrodynamic simulation of involute spur gears incorporating mixed friction, *Tribology International*, 48, 191–206.
3. Bongaerts J. H. H., Day J. P. R., Marriott C., Pudney P. D. A., Williamson A.-M. (2018), In situ confocal Raman spectroscopy of lubricants in a soft elastohydrodynamic tribological contact, *Journal of applied physics*, 104, 014913.
4. Brandão J.A., Seabra J.H.O., Castro J.D., Martins R. (2014), On the simulation of simultaneous fatigue and mild wear during a micro-

- pitting gear test, International Gear Conference: 26th–28th August 2014, Lyon, P. 523–531.
5. Brauer J., Andersson S. (2003), Simulation of wear in gears with flank interference – a mixed FE and analytical approach, *Wear*, 254, 1216–1232.
 6. Bravo A., Koffi D., Toubal L., Erchiqui F. (2015), Life and damage mode modeling applied to plastic gears, *Engineering Failure Analysis*, 58, 1, 113–133.
 7. Brethee K, Zhenc D., Gua F., Ball A (2017), Helical gear wear monitoring: Modelling and experimental validation, *Mechanism and Machine Theory*, 117, 210–229.
 8. Cherepova T., Dmitrieva G., Tisov O., Dukhota O., Kindrachuk M. (2018), Research on the properties of Co-TiC and Ni-TiC hip-sintered alloys, *Acta mechanica et automatica*, 13, 1, 57–67.
 9. Chernets M. (2019a), A method for predicting contact strength and life of archimedes and involute worm gears, considering the effect of wear and teeth correction, *Tribology in Industry*, 41, 1, 134–141.
 10. Chernets M. (2019b), Method of calculation of tribotechnical characteristics of the metal-polymer gear, reinforced with glass fiber, taking into account the correction of tooth, *Eksplatacja i Niezawodnosc – Maintenance and Reliability*, 21, 4, 546–552.
 11. Chernets M., Chernets Ju. (2017) The simulation of influence of engagement conditions and technological teeth correction on contact strength, wear and durability of cylindrical spur gear of electric locomotive, *Proc. JMachE. Part J: Journal of Engineering Tribology*, 231, 1, 57 – 62.
 12. Chernets M.V., Kelbinski J., Jarema R.Ja. (2011), Generalized method for the evaluation of cylindrical involute gears, *Materials Science*, 1, 45–51.
 13. Chernets' M.V., Lenik K. (1997), On estimation of materials durability, *Materials science*, 33, 834–840.
 14. Drozdov Ju. N. (1969), The calculation of gear trains wear resistance [In Russian], *Mashinovedenie*, 2, 84–88.
 15. Drozdov Ju. N. (1975), Development of wear calculation method and friction simulation [In Russian], *Wear resistance*, Science, Moscow, 120–135.
 16. Drozdov Ju.N., Nazhestkin B.P. (1990), The development of methods to calculate wear of toothed wheels [In Russian], *Engineering Gerald*, 11, 15–17.
 17. Feng K., Borghesani P., Smith W. A., Randall R.B., Peng Z. (2019), Vibration-based updating of wear prediction for spur gears, *Wear*, 426–427, part B, 1410–1415.
 18. Flodin A. (2000) Wear of spur and helical gears. *Dissertations and Theses*, UMJ Dissertations Publishing.
 19. Flodin A., Andersson S. (1997), Simulation of mild wear in spur gears, *Wear*, 207, 1–2, 16–23.
 20. Flodin A., Andersson S. (1999), Wear simulation of spur gears, *Lubrication science*, 5(3), 225–250.
 21. Flodin A., Andersson S. (2000), Simulation of mild wear in helical gears, *Wear*, 241(2), 123–128.
 22. Flodin A., Andersson S. A (2000), Simplified model for wear prediction in helical gears, *Wear*, 249 (3–4), 285–292.
 23. Gębura A., Klysz S., Tokarski T. (2019), Monitoring wear of gear wheel of helicopter transmission using the FAM-C and FDM-A methods, *Procedia Structural Integrity*, 16, 184–191.
 24. Gorokh G., M.I.Pashechko M., Borc J., Lozovenko A., Kashko I., Latos A. (2018), Matrix coatings based on anodic alumina with carbon nanostructures in the pores, *Applied surface science*, 433, 1, 829–835.
 25. Greco A.C., Erck R., Ajayi O., Fenske G. (2011), Effect of reinforcement morphology on high-speed sliding friction and wear of PEEK polymers, *Wear*, 271, 9–10, 2222–2229.
 26. Grib V.V. (1982), Solving of tribotechnical problems by numerical methods [In Russian], Science, Noscov.
 27. Guilbault R., Lalonde S. (2019), A stochastic prediction of roughness evolution in dynamic contact modelling applied to gear mild wear and contact fatigue, *Tribology International*, 140, 105854
 28. Hegadekatte V., Hilgert J., Kraft O., Huber N. (2010), Multi time scale simulations for wear prediction in micro-gears, *Wear*, 268, 316–324
 29. Kahraman A., Bajpaj P., Anderson N.E. (2005), Influence of tooth profile deviations on helical gear wear, *Journal of mechanical design*, 127, 4, 656–663.
 30. Kindrachuk M., Volchenko A., Volchenko D, Volchenko N., Poliakov P., Tisov O., Kornienko A. (2019b) Polymeres with enhanced energy capacity modified by semiconductor materials, *Functional materials*, 26, 3, 629–634.
 31. Kindrachuk M.V., Volchenko O.I., Volchenko D.O., Volchenko N.O., Polyakov P.A., Kornienko A.O., Yurchuk A.O. (2019a), Polymeric Materials Modified by Semiconductor Substances in Friction Units of Braking Devices, *Journal on nano- and electronic physics*, 11, 3, 03014.
 32. Kindrachuk V., Galanov B. (2014), An efficient approach for numerical treatment of some inequalities in solid mechanics on examples of Kuhn–Tucker and Signorini–Fichera conditions, *Journal of the Mechanics and Physics of Solids*, 63, 432–450.
 33. Kolivand M., Kahraman A. (2010), An ease-off based method for loaded tooth contact analysis of hypoid gears having local and global surface deviations, *Journal of mechanical design*, 132, 7, 071004.
 34. Kurdi A, Hongjian Wang H, Chang L. (2018), Effect of nano-sized TiO₂ addition on tribological behaviour of poly ether ether ketone composite, *Tribology International*, 117, 225–235.
 35. Liu H., Liu H., Zhu C., Tang J. (2020), Study on gear contact fatigue failure competition mechanism considering tooth wear evolution, *Tribology International*, 147, 106277 (Journal pre-proof).
 36. Liu, X., Yang, Y., Zhang, J. (2016), Investigation on coupling effects between surface wear and dynamics in a spur gear system, *Tribology International*, 101, 383–394.
 37. Mao K. (2007), Gear tooth contact analysis and its application in the reduction of fatigue wear, *Wear*, 262, 11/12, 1281–1288.
 38. Pashechko M., Krzysztof Dzedzic K., Mendyk E., Jerzy Jozwik J. (2018), Chemical and phase composition of the friction surfaces Fe–Mn–C–B–Si–Ni–Cr hardfacing coatings, *Journal of tribology*, 140(2), 021302.
 39. Pasta A. , Mariotti Virzi G. (2007), Finite element method analysis of a spur gear with a corrected profile, *Journal of strain analysis*, 42, 281–292.
 40. Pronikov A. S. (1978), Reliability of machines [In Russian], Machine engineering, Moscow.
 41. Raadni S. (2019) Spur gear wear analysis as applied for tribological based predictive maintenance diagnostics, *Wear*, 268, 316–324.
 42. Wang H., Zhou C., Leia Y., Liu Z. (2019), An adhesive wear model for helical gears in line-contact mixed elastohydrodynamic lubrication, *Wear*, 426–427, part A, 896–909.
 43. Wang, Y., Wang, Q. J. (2013), Stribeck Curves. *Encyclopedia of Tribology*, 3365–33150.
 44. Wei J., Niu R., Dong Q., Zhang S. (2020), Fretting-slipping fatigue failure mode in planetary gear system, *International Journal of Fatigue*, 136, 105632.
 45. Wu S., Cheng H.S. (1993), Sliding wear calculation in spur gears, *Journal of Tribology*, 115, 493–500.
 46. Zorkoa D, Kulovec S, Duhovnika J, Tavcar J. (2019), Durability and design parameters of a Steel/PEEK gear pair, *Mechanisms and machine theory*, 140, 825–846.